# CHEMICAL REVIEWS

Review

# Emerging Chalcohalide Materials for Energy Applications

Uma V. Ghorpade, Mahesh P. Suryawanshi,* Martin A. Green, Tom Wu, Xiaojing Hao, and Kevin M. Ryan
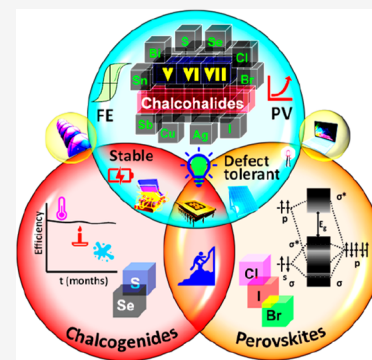
Read Online

ACCESS | Metrics & More | Article Recommendations

**ABSTRACT:** Semiconductors with multiple anions currently provide a new materials platform from which improved functionality emerges, posing new challenges and opportunities in material science. This review has endeavored to emphasize the versatility of the emerging family of semiconductors consisting of mixed chalcogen and halogen anions, known as "chalcohalides". As they are multifunctional, these materials are of general interest to the wider research community, ranging from theoretical/computational scientists to experimental materials scientists. This review provides a comprehensive overview of the development of emerging Bi- and Sb-based as well as a new Cu, Sn, Pb, Ag, and hybrid organic−inorganic perovskite-based chalcohalides. We first highlight the high-throughput computational techniques to design and develop these chalcohalide materials. We then proceed to discuss their optoelectronic properties, band structures, stability, and structural chemistry employing theoretical and experimental underpinning toward high-performance devices. Next, we present an overview of recent advancements in the synthesis and their wide range of applications in energy conversion and storage devices. Finally, we conclude the review by outlining the impediments and important aspects in this field as well as offering perspectives on future research directions to further promote the development of chalcohalide materials in practical applications in the future.

## CONTENTS

# 1. INTRODUCTION

Designing and developing synthesis techniques for new energy materials and that allow the scalable fabrication of high-performing devices is a rapidly advancing topic of research. Over the last 60 years, mainstream silicon semiconductor material technology has advanced significantly to improve device efficiency and lower fabrication cost, ensuring the future large-scale use of photovoltaics (PV).[1−3] Opportunities still exist for promising thin film energy materials such as CdTe,[4−6] Cu(In, Ga)Se$_2$ (CIGS),[5,7] Cu$_2$ZnSn(S, Se)$_4$ (CZTSSe),[4,5] and organic semiconductors[4,5] that promise even lower fabrication cost and shorter energy pay-back time over the well-established silicon technology. These materials efficiently harvest major parts of the solar spectrum, allowing tandem or multijunction devices to be built with efficiencies that exceed the Shockley-Queisser limit of a single-junction device.[8,9] However, already commercialized CdTe and CIGS suffer from a scarcity of Te and In elements for terawatt PV deployment, which has led researchers to investigate their counterpart CZTSSe containing earth-abundant and non/less-toxic constituent.[10−15] However, high-temperature synthesis (>500 °C), some lattice instabilities, and secondary phase formation during synthesis limit advancements in optoelectronic characteristics and device efficiencies at the commercial level.[16−18]

In recent times, halide perovskites, ABX$_3$ (where, A = MA$^+$ (CH$_3$NH$_3^+$), FA$^+$ (CH(NH$_2$)$_2^+$), Cs$^+$, or mixed A-cations; B = Pb$^{2+}$ or Sn$^{2+}$ or mixed B-cations; X = I$^-$, Br$^-$, or Cl$^-$ or mixed X-anions), a relatively old family of materials, have emerged as a member of the third-generation technologies for PV devices.[19−27] Recently, solar cells based on halide perovskites brought a promise of breaking a prevailing paradigm by reaching a record efficiency of 25.8% at a low fabrication cost in merely decade,[28] further challenging the 60-year reigned silicon technology (at least on the laboratory scale). Despite several key attributes of these halide perovskites, the fact that lead (Pb) is a major constituent of high performance devices entails toxicity issues from the fabrication steps to the final disposal/recycling.[29−32] Moreover, they undergo a rapid degradation on exposure to external stimuli (such as moisture, heat, and illumination or their combinations).[33,34] Furthermore, water soluble Pb ions escaping from perovskite devices can pose a severe toxicity issue owing to the moderate solubility of PbI$_2$ ($K_{sp}$ = 4.4 × 10$^{-9}$).[35] Apart from the general toxicity, the neurotoxicity of Pb (the maximum blood Pb level at 5 $\mu$g/dL for children set forth by World Health Organization (WHO))[36] is another concern. Given this, a number of significant advances are being developed that combat degradation and perform toward its stability, which again pique scientific interest.[37−42] However, the challenges associated with instability of Pb-halide perovskites, combined with their toxicity, motivate the search for alternate, intrinsically stable perovskite-type materials contain-

ing non-/less-toxic elements. A simple approach toward the synthesis of environmentally benign halide perovskite-based materials is to replace toxic Pb with Sn or Ge since both elements fulfill the ionic size, coordination, and charge balance requirements to form the perovskite structure.[22,43−50] However, Sn$^{2+}$ and Ge$^{2+}$ cations in perovskites can be easily oxidized to Sn$^{4+}$ and Ge$^{4+}$, respectively, resulting in relatively fast degradation, low performance, and challenges in reproducibility,[50−54] further limiting their practicability over Pb-based halide perovskites.[29,32,44] The phenomenal performance of the above-mentioned halide perovskites can be linked to the outermost ns$^2$ electrons in the metal cation, which rationally leads to the possibility of utilizing Bi and Sb (from their ability to form 3$^+$ ions) with a similar electronic configuration as Pb$^{2+}$. In this regard, vacancy-ordered Bi- and Sb-based double perovskites having the structure A$_3$B$_2$X$_9$ or nonperovskite structures have been developed.[53−62] However, these materials offer poor dichotomy, (i) stable in air while not offering 3D structure or direct bandgaps, and (ii) relatively small effective masses but also strongly bound excitons, inhibiting free carrier generation.[30,63] Moreover, they also exhibit low mobilities, poor charge transport, and high resistivities from 10$^{10}$−10$^{12}$ $\Omega$ cm, ultimately leading to poor device performances.[63] Therefore, the pursuit for alternative highly stable and less-toxic light-harvesting materials with the feature of ns$^2$ lone pair cations is a challenging research area.

Chalcohalides are an emerging family of inorganic semiconductors that are commonly denoted as MChX, where M stands for one or more metal cations and Ch and X stand for one or more chalcogen and halogen anions, respectively (e.g., SbSI, BiSI, SbSeI, BiSeI, and their derivatives) (Scheme 1). They were extensively studied in the 1960s due to their promising glass-forming abilities and exotic physical, chemical, optical, and ferroelectric properties.[64−71] Maintaining charge neutrality in hybrid organic—inorganic metal chalcohalides (AB(Ch, X)$_3$) requires the use of trivalent or tetravalent B cations and thus the advancement of chalcohalide perovskite as an area of research.[72] The motive behind chalcohalide perovskite stems from the stability issue of the halide perovskite owing to the presence of the ionic B-X bond. High electronegativities of halogen atoms add the ionic character to the B—X bond making these materials unstable. To improve the properties, a nonhalide Ch (chalcogenide (S, Se) anions) is substituted, which gives the B-X bond covalent character, improving the stability but with increased enthalpy of formation. Such partial substitution of halides with chalcogenide anions is called a "split-anion approach".[73,74]

Moreover, chalcohalide materials may offer good charge transport properties because of the high-Z ns$^2$ levels of d$^{10}$s$^2$p$^0$ electron configuration. A highly dispersive character of both valence band (VB) and conduction band (CB), due to the peculiar electronic structures, offers a high charge carrier mobility and defect tolerance in these chalcohalides.[75] Interestingly, the presence of both divalent chalcogen (S$^{2-}$/Se$^{2-}$) and monovalent halide (I$^-$/Br$^-$/Cl$^-$) anions in these chalcohalide materials allows facile tuning of crystal and electronic structures and optical properties.[75−77] These tunable properties broaden their use in various applications including room temperature (RT) radiation detection, transparent electronic devices, photodetectors, photocatalysis, photoelectrochemical (PEC) water splitting, light-emitting diodes (LEDs), batteries, supercapacitors, and single junction and tandem solar cell devices. Table 1 summarizes the fundamental

**Scheme 1. Overview of the Current Status of Representative Chalcohalide Materials**
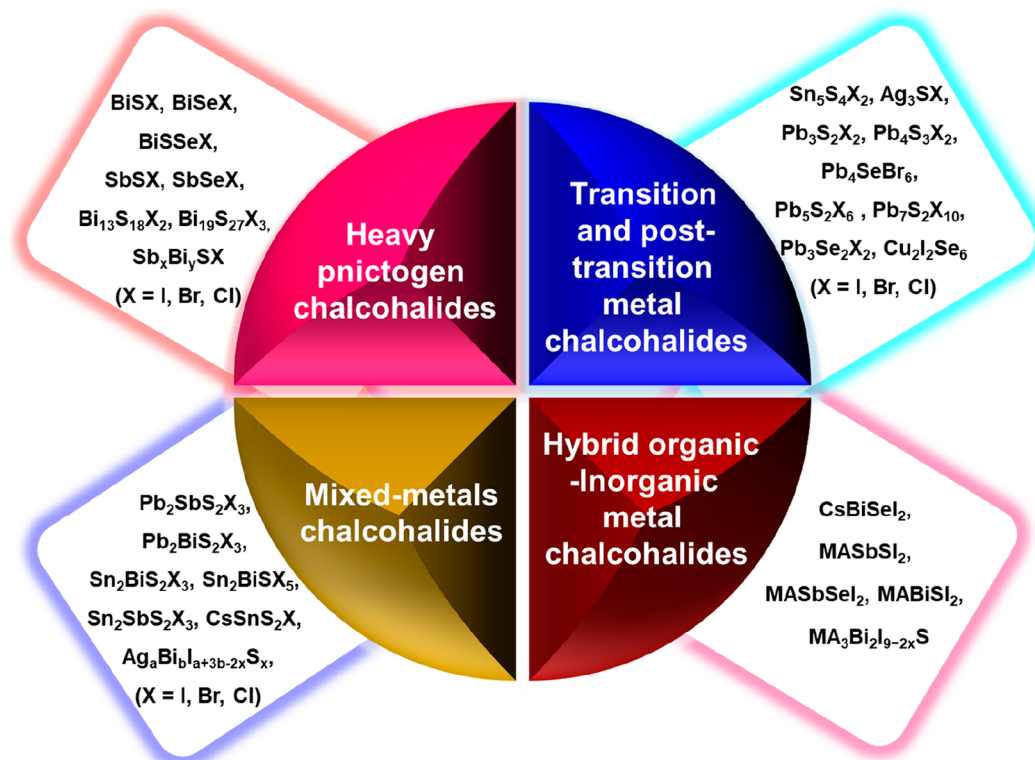


structures, optoelectronic properties, and their application in various energy conversion and storage devices. The extensive developments in chalcohalide materials bring a necessity to review chalcohalides focusing on the materials design, their properties, film fabrication, and device fabrication while providing a perspective on future directions and potential applications in energy devices (Scheme 2). The synthesis and applications of Bi- and Sb-based chalcohalide materials have been previously discussed as a part of dedicated book chapters[78−80] and reviews[81−83] as well as a brief overview of their potential in solar cell devices.[84−86]

In this review, we comprehensively discuss various chalcohalide materials according to the type of metal cation(s) and assess their potential in various energy conversion and storage. It includes an up-to-date overview of the heavy pnictogen chalcohalides (M = Bi and Sb), transition and post-transition metal chalcohalides (M = Cu, Sn, Pb, and Ag), mixed-metal chalcohalides (M = Bi/Sb with other metals), and hybrid organic−inorganic metal chalcohalides (i.e., chalcohalide perovskite) not only from the synthesis point of view but also from device perspective. Following the introduction (section 1), we briefly discuss high-throughput computational techniques to design, develop, characterize, and further optimize these materials and highlight the enabling attributes including optoelectronic properties and structural chemistry of interest (sections 2 and 3). Next, we discuss recent theoretical advances in the developments of Bi- and Sb-based chalcohalide materials followed by the progress of some new Cu-, Sn-, Pb-, and Ag-based chalcohalides to motivate further research in this field (section 4). We also highlight major achievements in the synthesis of these materials and their application in various devices such as solar cells, photodetectors, photocatalysis, thermoelectrics, batteries, supercapacitors, and piezo/pyro-electric nanogenerators (section 5). Beyond summarizing the

developments and applications of these chalcohalides, road-blocks and key points to fabricate high-performing devices are further discussed. Lastly, we provide a brief outlook on this field and a perspective on the future directions for chalcohalide materials.

## 2. MATERIALS PROPERTIES AND RESEARCH METHODS ENABLING ATTRIBUTES TOWARD OPTOELECTRONICS

The requirements of emerging chalcohalide semiconductor materials have four basic criteria: (1) processability and chemical stability, (2) suitable bandgap and high absorption coefficient to ensure maximal absorption of light in the visible region, (3) high mobility and dopability to enable sufficient charge carriers, and (4) defect tolerance. In this section, we discuss both the theoretical and experimental aspects of these materials properties/chemistries that enable attributes for high-performance energy conversion devices. We mainly emphasize properties relevant to solar cells, photocatalysis, photodetectors, and nanogenerators.

Lately, much progress has been made in theoretical computation and screening using the Materials Genome Initiative (MGI) that led to the development of different computational programs such as Materials Project,[87] AGLOWLID,[88] NREL-MatDB,[89,90] and the Open Quantum Materials Database.[91] These programs compile data from density functional theory (DFT) calculations and offer a progressive pathway for screening and exploring materials candidates for desired applications. This has revolutionized the way materials are selected for synthesis in the community of experimental materials scientists. A standard pathway has been established for computational materials screening to guide accelerated discovery and designs of materials across a broad range of applications, termed as the "funnel" approach.[92]

**Table 1. Fundamental Properties and Applications of Chalcohalide Materials**

| chalcohalides/properties | bandgap (experimental) eV | bandgap (theory) eV | band alignment | conductivity type | crystal structure | effective mass (e, h) | application[a] |
|---|---|---|---|---|---|---|---|
| BiSX | 0.7–2.05 | 1.0–1.78 | direct, indirect | n-type | orthorhombic | 0.53, 0.95 | PV, DSSC, PEC, PC, PD, battery, TE |
| BiSeX, $Bi_3Se_4Br$ | 1.27–1.71 | 1.0–2.2 | direct, indirect | n- and p-type | orthorhombic | ~0.53–0.57, ~2.19–2.98 | |
| BiSSeX | 1.48–1.63 | | | | | | PEC |
| $Bi_{19}S_{27}X_3$ | 0.77–1.6 | | direct | p-type | hexagonal | | PC, PD |
| $Bi_{13}S_{18}I_2$ | 0.75–1.57 | 0.6–0.91 | indirect, direct | n-type | hexagonal, trigonal | | battery, TE |
| SbSX | 1.77–2.15 | 1.4–2.21 | indirect, direct | | orthorhombic | 0.07–0.54, 0.098–0.65 | PEC, DSSC, PC, PD, battery, PNG, |
| SbSeX | 1.67 | 1.29–1.67 | indirect | | | 0.52 | PENG |
| $Sb_xBi_ySI$ | 1.51–1.83 | | | | | | PV |
| $Pb_3S_2X_2$, $Pb_4S_3X_2$, $Pb_4SeBr_6$, $Pb_5S_2I_{6\ (direct)}$, $Pb_7S_2Br_{10}$ | 1.6–2.5 | 1.5–2.0 | indirect | | orthorhombic, pseudocubic | | PV, PD |
| $Pb_3Se_2X_2$ | 1.48 | | indirect | | orthorhombic, cubic | | |
| $Sn_5S_4Cl_2$ | | | | | | 0.5, 0.4 | |
| $Cu_2I_2Se_6$ | | 1.95 | indirect | | rhombohedral | 0.32 | |
| $Pb_2SbS_2I_3$, $Pb_2BiS_2I_3$, $Sn_2BiS_2I_3$, $Sn_2BiSI_5$, $Sn_2SbS_2I_3$, $CsSnS_2Cl$ | 1.2–2.19 | 1.08 ($Sn_2SbS_2I_3$), 0.98 ($CsSnS_2Cl$) | direct indirect ($CsSnS_2Cl$) | n-type | orthorhombic, monoclinic | | PV |
| $Ag_3SI$, $Ag_3SBr$, $Ag_aBi_bI_{a+3b-2x}S_x$, | 0.9–1.87 | | | | | | PV |
| $MASbSI_2$, $MASbSeI_2$, $MABiSI_2$, $MA_3Bi_2I_{9-2x}S$ | 1.67–2.03 | 0.83–1.4 | direct | | cubic, hexagonal | 0.32, 0.4 | PV |

[a]PV, Photovoltaic; DSSC, dye-sensitized solar cells; PEC, photoelectrochemical cell; PC, photocatalysis; PD, photodetector; TE, thermoelectric; PNG, pizeoelectric nanogenerator; PENG, pyroelectric nanogenerator.

Usually, it begins with more computationally "inexpensive" steps such as queries of possible structures from the available Inorganic Crystal Structure Database (ICSD).[93] This step is followed by more in-depth steps that require more computer resources to explore the new materials not available in the database using chemical substitution or structure similarities, or via random searches or using machine learning (ML).[94] The key requirements for computational materials screenings as shown in Figure 1, left panel include (1) an initial data subset enumerating different stoichiometries or structures, (2) iterations for energetic stability, (3) essential descriptors or chemical constraints to realize the properties of fundamental interests (e. g., bandgap, effective masses, mobility of charge carriers etc.), and (4) advanced electronic structure screening to derive accurate band structure and defect tolerance in materials. These effective computational screening steps allow the down-selection on the order of tens of materials for further experimental investigations. Like the computational "funnel" approach (Figure 1, right panel), materials discovery through experiments follows an "experimental funnel" approach. This follows a standard approach of experimental synthesis of materials and their series of characterizations to determine the structure, composition, and optoelectronic properties, which could be further correlated to the computational results.[93–96] In some cases, iterative computational screening-experimental validation steps would require discovering materials with an end goal of achieving high-performance energy devices.

Utilizing the above-mentioned combined approaches of ab initio calculations and machine learning (ML), two-dimensional (2D) chalcohalide ($A_2B_2X_2$, B = S/Se/Te, X = F/Cl/Br/I) materials have been discovered.[93] Initially, an input data set was generated by performing DFT calculations on the structural and electronic properties of 300 out of 5300 2D chalcohalides, each

of which was described by 62 initial descriptors. Following that, different ML models were tested to find suitable ML models with a minimum complexity of 26 descriptors. This ML model predicted the electronic properties of the remaining 5000 chalcohalides and screened out 411 chalcohalides with band gaps ranging from 0.9 to 1.6 eV. Materials with high cost and toxicity were then further excluded, resulting in 71 chalcohalide materials with desired properties as the outcome of initial screening, as demonstrated by the funnel approach in Figure 1, left panel. These 73 chalcohalides were systematically scrutinized by DFT for their stability, charge carrier effective masses, and mobility (Figure 1, right panel), and three chalcohalides ($Bi_2Se_2Br_2$, $Bi_2Se_2(BrI)_2$, and $Bi_2Se_2I_2$) were predicted to have suitable band gaps, high absorption coefficients, and carrier mobilities, making them promising candidates for optoelectronic performances. With this context and the latest updates in mind, the following sections discuss the properties of chalcohalides as a result of the computational and experimental funnel approaches described above, as well as some advanced computational outcomes in section 4.

## 2.1. Band Gap, Carrier Effective Masses, and Dielectric Properties

The incorporation of transition metals and chalcogen in lead-free perovskites has been proposed as a viable solution for improving the materials properties through bandgap engineering.[84,97–101] Likewise, heterovalent ions combine the excellent optical properties of both perovskites and chalcogenides since both positively and negatively charged ions addition are feasible bandgap tuning methods and thus the lifetime of charge carriers.[84–86] The semiconductor chalcohalides (V–VI–VII) consisting of thio-, seleno-, and halogens are discussed in the present review, e.g., V = Bi, Sb, Pb, Sn, Cu, Ag; VI = S, Se; VIII = Cl, Br, I. Among them, pnictogen chalcohalides are Bi- and Sb-

**Scheme 2. Chalcohalides Presenting Tunable Optoelectronic Properties, Indicating the Wide Range of Applications That Can Be Pursued**
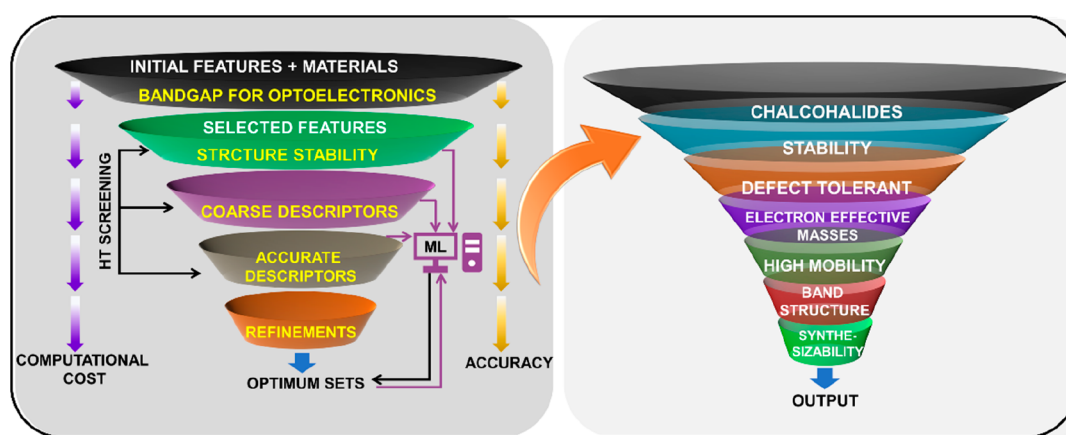




**Figure 1.** Funnel type prediction models comprising different parts such as input data set, ML model, ML predictions, and preliminary screening (left panel) and generic high throughput computational screening of chalcohalide compounds (right panel). Based on optimum sets from the prediction model, the selected candidates will be then further screened for their stability, defect tolerance, electron effective masses, mobility, and band structure using density functional theory (DFT). Reproduced (reprinted in part) with permission from refs 92 and 93. Copyright 2021 Wiley and 2019 American Chemical Society.

based post-transition metal chalcohalides that comprise a trivalent heavy pnictogen (Bi/Sb) cation, a divalent (S/Se) chalcogenide, and monovalent (I/Br/Cl) halide anions. These materials show both types of band alignment (direct and indirect), with n- and p-type depending on their synthesis methods and bonding of ions into crystal structures. As an example, BiSeI grown by chemical transport reaction shows n-type conductivity,[102] whereas when grown by the Stock-Barger method (growth from the melt) shows both n- and p-type conductivity.[103] The structural arrangement of metal cations bonded to multiple anionic ligands can improve the local degree of freedom and lower local asymmetry while achieving band gap
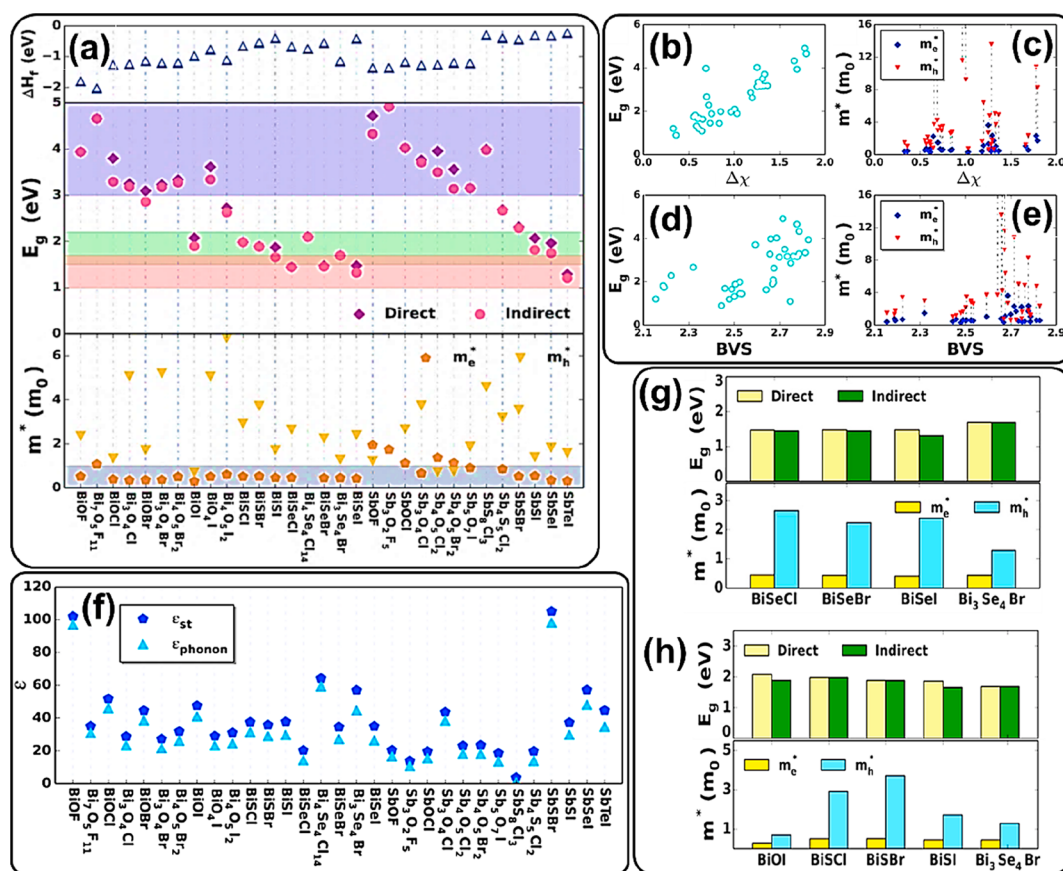
**Figure 2.** (a) Formation energies per atom (upper panel), band gaps (middle panel), and effective masses of electron and hole (lower panel) for the 31 Bi- and Sb-based compounds. Red, green, and blue shaded areas in the middle panel indicate bandgap ranges of 1.0−1.7, 1.5−2.2, and >3 eV, respectively. Gray shaded area in the lower panel indicates effective masses lower than the rest mass of the electron ($m_0$). (b) Band gaps and (c) effective masses of holes and electrons as a function of average electronegativity discrepancy between anions and cations for the 31 Bi- and Sb-based compounds. (d) Band gaps and (e) effective masses of holes and electrons as a function of bond valence sum (BVS) of the cations. (f) Calculated dielectric constants ($\varepsilon$) of the considered Bi/Sb oxyhalides and chalcohalides. Total static dielectric constant ($\varepsilon_{st}$) and the component from phonon contribution ($\varepsilon_{phonon}$) has been shown. (g) Histogram of HSE + SOC band gaps, effective masses of holes and electrons for BiSeCl, BiSeBr, BiSeI, and $Bi_3Se_4Br$. (h) Histogram of HSE + SOC band gaps, effective masses of holes and electrons for BiOI, BiSCl, BiSBr, BiSI, and $Bi_3Se_4Br$. (a−h) Reproduced with permission from ref 75. Copyright 2018 Nature Publishing Ltd.

control. On the other hand, the difference in their bonding caused by the electronegativity difference in anions causes an increase in the distortion degree of coordination polyhedron. Chalcohalide materials reviewed in the current review showed experimental and theoretical band gaps between ∼0.75 and 3.0 eV and were also tunable with varying chalcogen and halogen composition,[75,104−112] suggesting their potential application in the wide optoelectronic and solar energy conversion devices. Most of the chalcohalides, which have shown PV performance up to now, exhibit high absorption coefficient ($>1 \times 10^5$ cm$^{-1}$) and indirect band gaps. However, the difference between direct and indirect band gaps is very small (between 0.02 to 0.1 eV), which makes them potential candidates for solar energy conversion devices. Despite the fact that this family of materials has been synthesized decades ago, their potential application in solar energy conversion has only recently been predicted (theoretically). However, the synthesis of these chalcohalide materials with the chosen optoelectronic properties is still challenging for large-scale applications.

The theoretical and experimental data revealed that chalcohalide materials, like chalcogenides[113−116] and halide perovskites,[117−121] possess highly nonlinear dielectric properties and exhibit a strong piezoelectric effect. These types of materials

are characterized by their layered structure, strong anisotropy, and relativistic effect. Most of these materials also possess the ferroelectric-PV (FE-PV) effect, which refers to the generation of a steady PV response (photocurrent/photovoltage) along the polarization direction in these ferroelectric materials without central symmetry. It is different from the standard PV effect where the photogenerated charge carriers at the semiconductor p−n junction are separated by an internal built-in electric field. Notably, the direction of photocurrent in the FE-PV device can also be reversed by changing the spontaneous polarization direction with an external electrical field.[122,123] Many well-known ferroelectric materials possess the perovskite structure including halide perovskites[124−127] and recently emerging chalcogenide perovskites.[128−131] Since the dielectric constant is a measure of the of electric potential energy in the form of induced polarization, this feature increases the promise of such materials considerably.[118] It is assumed that large dielectric constants and low effective masses would promote efficient ionization of defect states and suppress deep trap states within the bandgap.[132] The antibonding character of s orbitals causes the lower hole effective masses than the electron effective masses.[133]
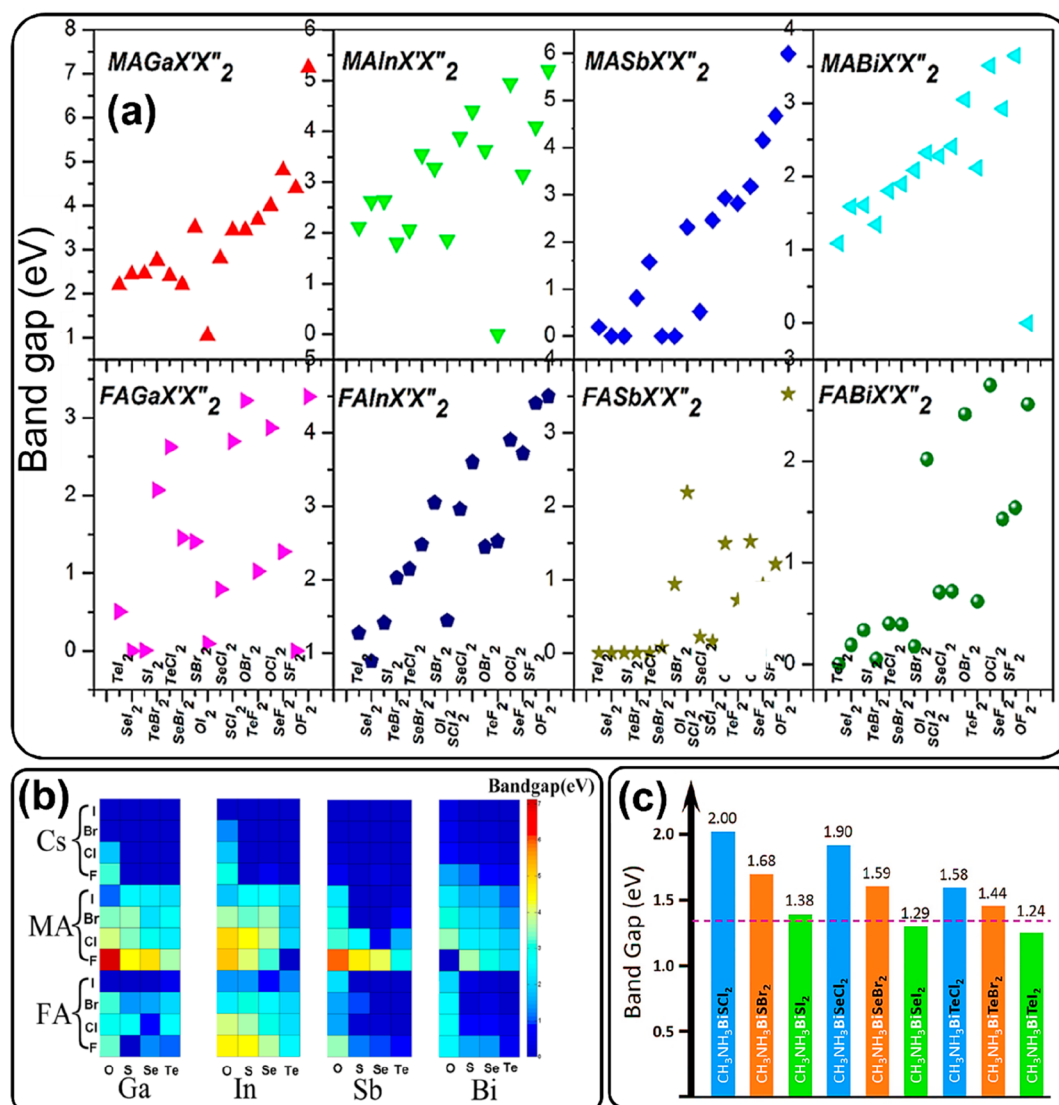
**Figure 3.** (a) Band gap as a function of average electronegativity and (b) calculated band gaps of 192 mixed-anion perovskites. Each square represents a material, and the color represents the corresponding band gap. The larger letters are A ions, and the smaller letters are X″ ions on the left. The larger and smaller letters below are B and X′ ions, respectively. (a, b) Reproduced with permission from ref 137. Copyright 2019 American Chemical Society. (c) Calculated band gaps of $CH_3NH_3BiXY_2$ compounds (with X = S, Se, or Te and Y = Cl, Br, or I) using the HSE functional with SOC. The dashed line marks the optimal band gap for a single-junction solar cell according to the Shockley−Queisser theory. Reproduced with permission from ref 73. Copyright 2016 The Royal Society of Chemistry.

Ran et al.[75] calculated formation energies, band gaps, and effective masses of electrons/holes and dielectric constants for the 36 Bi- and Sb-based materials, shown in Figure 2. As shown in Figure 2a, the negative formation energy indicates the successful synthesis of these materials. The respective materials have both direct and indirect band gaps and smaller effective masses. The effective masses of holes and electrons are shown not only as a function of the average electronegativity discrepancy between anions and cations but also as a function of the bond valence sum of the cations (Figure 2b−e). Additionally, the high dielectric constant values due to large phonon contributions show the capability of the material for energy-related applications (Figure 2f). Pb-halide perovskites have high dielectric constant, low effective masses, and VB antibonding nature that lead to defect-tolerant transport characteristics due to their $ns^2$ electronic configuration.[134,135] Similarly, these chalcohalide materials with $ns^2$ electronic configuration have shown higher dielectric constants and

accordingly smaller charge capturing cross-section defects that cause low scattering and recombination.[132] Section 4 discusses the theoretically calculated band alignment and effective masses for various chalcohalides in detail. For easy understanding, the histograms of Heyd-Scuseria-Ernzerhof (HSE) hybrid functional + spin orbit coupling (SOC) band gaps, effective masses of electron and hole for different Bi-based chalcohalides are also presented in Figure 2g and h. It reveals that iso-structural compounds, BiSeCl, BiSeBr, and BiSeI, show similar optical band gaps of ∼1.47−1.48 eV, where BiSCl, BiSBr, BiSI, and $Bi_3Se_4Br$ have bandgaps in the range of 1.5−2.2 eV. The BiSeCl, BiSeBr, and BiSeI materials have shown similar transport effective masses of 0.53−0.57 $m_0$ and ∼2.19−2.98 $m_0$ for electrons and holes, respectively. It illustrates the prominent role of the chalcogen in the electronic structures of the upper VB and also indicates the potential as a solar absorber material, which is consistent with the present findings. In BiSCl, BiSBr, BiSI, and $Bi_3Se_4Br$ materials, the electron or hole effective masses are

lower than $m_0$, indicating that these materials are potentially useful as RT radiation detection materials. SbSI indicates an optical bandgap of ~2 eV, and in fact, it can be varied by changing the chalcogen and halide.[109,118] Theoretically calculated electron effective masses using generalized gradient approximation (GGA) for SbSI, SbSBr, and SbSeI were 0.21, 0.26, and 0.52 $m_0$, respectively, with bandgaps of 1.51, 1.57, and 1.29 eV, suggesting possible high mobility in good quality crystals with low defect concentrations.[74] Berry phase analysis of the polarization revealed that, despite having a smaller change in polarization ($\Delta P$) than many perovskite structures, all three materials have significant spontaneous electric dipole moments. Besides, $Sn_5S_4Cl_2$ was theoretically predicted to be stable compositions with bandgaps across the visible range, but it also evidenced low electron and hole effective masses of 0.5 $m_e$ and 0.4 $m_h$, respectively, suggesting that it could be used as a low-bandgap absorber in multijunction solar cells.[85,136]

To improve the properties and sustainability of halide perovskite, researchers focused on the addition of chalcogen ion to $ABX_3$ perovskite making it $AB(ChX)_3$-type chalcohalide perovskite. Although the photoconversion efficiencies of solar cells based on Bi- and Sb-based halide perovskites are significantly lower than those of organic–inorganic Pb-halide perovskites,[138–141] the inclusion of negatively charged chalcogen ions shifts their bandgaps for favorable optoelectronic properties and forms metal chalcogenide bonds. As a result, the overall covalence significance of the compound is found to be more significant, leading to improved durability. Mao et al.[137] calculated the band gaps of selected 192 mixed-anion chalcohalide perovskites ranging from 0 to approximately 7 eV as well as the influence of total anion electronegativity on band gaps for the methylammonium (MA) and formamidinium (FA) systems (Figure 3a). Similar to halide perovskites, the bandgap values of these chalcohalide perovskites increase when X″ ($F^-$, $Cl^-$, $Br^-$, or $I^-$) changes from I to Br, Cl, and F (from top to bottom in the panel) and decrease when the X′ ($O^{2-}$, $S^{2-}$, $Se^{2-}$, or $Te^{2-}$) changes from O to S, Se, and Te (from left to right in the panel) as presented in Figure 3b. This study thus introduces a viable pathway for exploring stable, lead-free chalcohalide perovskites for PV applications by screening suitable candidates from the 192 compounds by taking into account the tolerance, octahedral factor, and stability. Figure 3c shows the band gaps for the nine materials with combinations of S, Se, or Te and Cl, Br, calculated using the HSE hybrid functional with SOC. According to the Shockley–Queisser theory, the bandgap of these materials can be tuned to provide an optimum bandgap for a single-junction solar cell.[73] Red-to-black piezochromic response for a larger bandgap $(CH_3NH_3)_2[PbI_2(SCN)_2]$ (MAPSI) material captured researchers' attention.[142] Although the performance of MAPSI may be affected by MAPI contamination, the typical optical properties and its large pressure response may originate from (i) the short interlayer contact, (ii) the covalency of the Pb–S linkages, and (iii) the electronic effects of SCN− substitution in the Pb–I lattice. However, significant response of the material to comparatively low pressures opens up new avenues for more optical and electronic diversity from 2D structures.

## 2.2. Defect Tolerance

The $ns^2$ electronic configuration of cations plays a vital role in the optoelectronic properties of the materials.[143] Therefore, materials containing post-transition metals, such as $Bi^{3+}$, $Sb^{3+}$, $Cu^+$, $Pb^{2+}$, and $Sn^{2+}$ (with $ns^2$ electronic configurations), are

considered as defect tolerant,[97,144] which leads to slow electron–hole recombination kinetics from their intrinsic point defects and could make them last longer.[97,145–147] Chalcohalide materials containing these post-transition metals with a $6s^2$ or $5s^2$ electronic configuration can share the high dielectric constant, low effective masses, and antibonding character of VB, which all contribute to the defect tolerant transport properties.[97] These partially oxidized ($Bi^{3+}$, $Sb^{3+}$, $Sn^{2+}$, $Pb^{2+}$) and polarizable cations offer high-born effective charges and therefore large dielectric constants, CB with greater bandwidth due to SOC, dispersive VB, and low effective masses due to filled 5s/6s orbitals. Wlázlak et al.[81] also emphasized multiple features of these chalcohalides such as low carrier effective masses, the ferroelectric-PV effect, and the $ns^2$ configuration of trivalent heavy pnictogens, which are thought to be the source of defect tolerance similar to in Pb-halide perovskites.

A $ns^2$ electron configuration is mainly encountered in defect tolerant semiconductors, indicating that the presence of lone pair electrons in metals is an important point in their appealing optoelectronic properties. Consequently, this characteristic gives a more rational basis for attributes like band gaps, carrier effective masses, and defect levels same as in perovskites.[148] The antibonding feature of the valence band maxima (VBM) (with mixed halide 3/4/5p and s character) and spin–orbit effects in the CB are what give the vacancy-related states their shallow defect character.[20] As a result, the presence of lone-pair states and antibonding coupling at VBM are critical band edge characteristics for favorable optoelectronic properties.[148] In addition to producing a higher energy VBM that lowers ionization energies and results in decreasing band gaps, the antibonding component also produces more dispersive bands from s-p hybridization, raising hole mobility and lowering recombination rates.[149] Since the occupied cation "s" states both produce lighter hole masses and increase the valence band energy by introducing cation s-anion p interaction. Furthermore, the lone electron pair involved with compounds formed from metals with a $ns^2$ electronic configuration has been shown to be strongly dependent on the electronic states of the anion.[150] The geometric variation of these compounds, including the structural distortions linked to the lone pair of electrons, may be simply explained by the relative energy differences between the electronic states participating in the orbital interactions.[151] Dangling bond defects might be drawn quantum mechanically into the continuum bands by the existence of an antibonding higher VB and a bonding lower CB, leaving the bandgap clear and enabling the creation of shallow defects.[152]

Thus, the defect tolerance property arises from the fundamental electronic band structures, the density of states (DOS), orbital characters of the CB and VB extrema, effective masses of electrons and holes, dielectric constant of the material, etc. The presence of intrinsic point defects, particularly structural defects in the defect-tolerant materials, causes relatively slow electron–hole recombination kinetics within the bandgap.[153,154] Depth of the defect level can also be quantified.[146] Although the idea of defect tolerance is claimed to extend to this class of materials, it has not yet undergone a thorough investigation. Zhang et al.[155] developed a computational method to evaluate the term "defect tolerance" by quantitatively examining the nonradiative recombination rates caused by deep-level defects, which gives rise to another phase of further research.
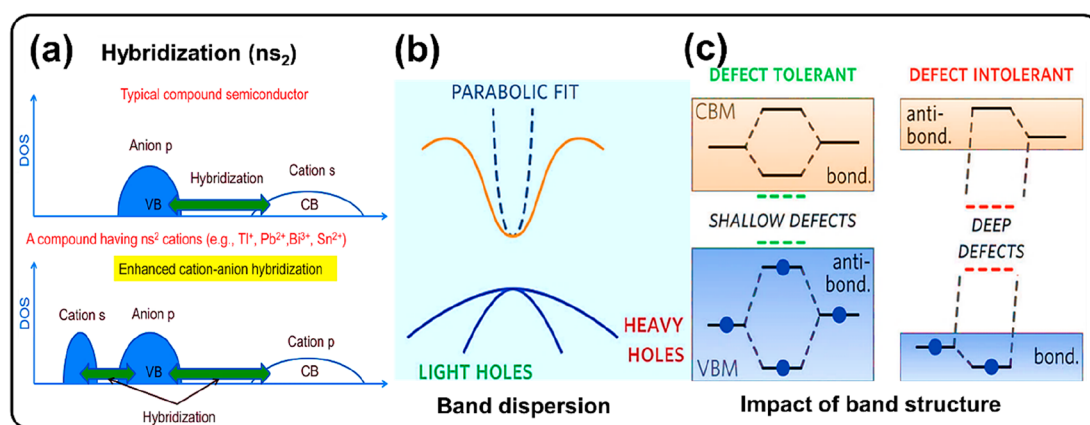
**Figure 4.** (a) Schematic of DOS for a typical compound semiconductor (not including transition-metal and rare-earth compounds with significant d or f character in the CB) (top) and a compound that contains $ns^2$ cations (bottom). Reproduced with permission from ref 143. Copyright 2016 American Physical Society. (b) Schematic band structure indicating how greater band dispersion (curvature) gives rise to smaller hole and electron effective masses and (c) impact of bonding structure on defect tolerance, with antibonding states at the top of the VBM giving rise to shallower defects. (b, c) Reproduced with permission from ref 144. Copyright 2016 The Royal Society of Chemistry.

## 2.3. Band Structure

Chalcohalide materials show a high level of band dispersion and antibonding states in the VBM. This gives the materials both ionic and covalent characteristics and hence strong lattice polarization and large static dielectric constant.[75] Hybridization of cation s and anion p orbitals makes the dispersive VB (Figure 4a, upper panel). Additionally, the cross-band gap hybridization takes place between extended cations p orbital from CB with anion p orbital from VB as shown in Figure 4a (lower panel). Such cross-gap hybridization indicates covalency in the otherwise ionic materials, as stated above.[143] Also, the presence of 5s or 6s orbital in VB causes the charge transfer from s and p state, contributing to the strong optical absorption. The presence of chalcogen along with halogen reduces the intrinsic ionic conductivity in the chalcohalide materials, which in turn helps to increase the charge collection efficiency and reduce the space charge effects.[111] SbSI material is predicted to have the same band structure as that of Pb-based halide perovskite and hence exhibits low effective masses of charge carriers, high absorption coefficient, and suitable bandgap, making them suitable for PV and ferroelectrics.[75,97,156] This $ns^2$ configuration causes the cation-s state to move down in energy, forming the lone pair state and separating from the cation-p states due to the Mass-Darwin effect. This causes the significant charge transfer only from the cation-p to the anion-p states rather than from the cation-s to the anion-p states.[75] In such materials, therefore, VBs are mainly formed by antibonding combinations of cation-s and anion-p states and CBs are dominated by spatially extended cation-p states and also hybridize in the antibonding pattern with anion-p states. All these characteristics cause dispersive VBs and CBs making the material favorable for small effective mass, high carrier mobility and Born effective charges, and high defect tolerance (Figure 4b,c).[144] Consequently, the presence and preferences of the elements from group III to VII make the material a great candidate for optoelectronics. This is because (i) the typical combination of cation and anion, as well as the partially oxidized cation, leads to shallow inner point defects in the material (Figure 4c),[144] (ii) not only is the dispersion of the VBM dependent on the hybridization between anion p-orbitals and cation s-orbitals but 70−90% of the VBM partial DOS (pDOS) in these materials originates from anion p orbitals, and (iii) when the cations dangling bond that surround the anion

vacancy have minimal interaction, they form the shallow anion vacancies. This is possible when dispersive CBM is formed from heavy cation p-orbitals. In most of the selenoiodides, in which anions have low coordination number and cation−cation distances are long, shallow anion vacancies are often formed, allowing efficient electron transport and thereby making them good electronic and optoelectronic materials.[146] The presence of a relativistic effect that increases the width of the CB by lowering the CBM stabilizes chalcohalide materials against oxidation.[82,157] The relative energy of the p and s orbitals determines the contribution of the s orbital to the VBM. Because the VB forms by combining the anion p with cation s orbitals with the antibonding VBM, it again is directed toward the stabilization since s orbitals more greatly contribute to making a stronger lone pair and hence shallow states at the band edges, rather than deep gap states that act as traps and recombination centers (Figure 4c).[133,158] All of these properties are therefore supposed to provide a high degree of defect tolerance. Bi-based materials share many similarities in the chemical properties with Pb-based halide perovskites, e.g., stable electronic configuration ($d^{10}s^2p^0$), similar polarizability, rich structural diversity ($BiX_6$ clusters, one-dimensional (1D) structure, layered structure), and large relativistic effects.[82,133,157]

## 2.4. Stability

Long-term stability is one of the key factors along with the efficiency, cost-effectiveness, and nontoxicity of materials, determining the perspective of commercialization. Although hybrid Pb-halide perovskite semiconductors have become one of the most researched semiconductor materials in the last ten years, they are prone to instability in the presence of moisture, oxygen, and temperature. In comparison, the current study has been intended to look a benign alternative that is also stable under atmospheric conditions. Materials can be assessed concerning their structural and device stabilities. When we talk about structural stability, we mainly refer to the ability of materials to retain their desired phase under ambient conditions. While device stability is referred to maintaining the performance without any significant changes in defects concentration or at interfaces between different stacked layers such as chemical changes including composition, diffusion of elements or decomposition of materials. Chalcohalides have been predicted to be stable compared to the inorganic and organic−inorganic
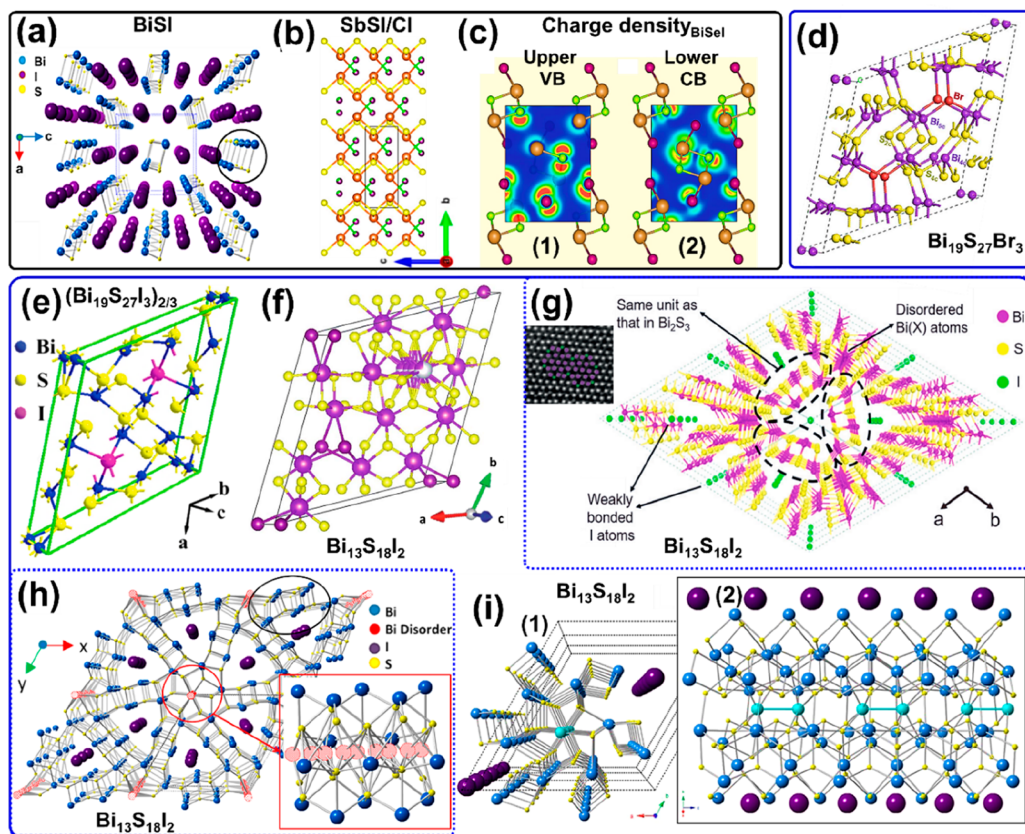
**Figure 5.** (a) BiSI structures, viewed down the *b*- axis at the ac plane of their orthorhombic unit cells. The black circle highlights the Bi–S 1-D chain. Reproduced with permission from ref 107. Copyright 2017 American Chemical Society. (b) Crystal structure of SbSI/Cl (SbSI$_{0.73}$Cl$_{0.27}$) viewed along *a*-axis where the double-chains arrange along the *c*-axis within the Sb–S and Sb–(I, Cl) chemical bonds. Reproduced with permission from ref 170. Copyright 2019 American Institute of Physics. (c) Charge density isosurfaces of the (1) upper VB and (2) lower CB of BiSeI. Regions of low and high electron density are shown in blue and red, respectively. Bi, Se, and I atoms are denoted by orange, green, and purplish–red spheres, respectively. Reproduced with permission from ref 133. Copyright 2016 The Royal Society of Chemistry. (d) Structural model for Bi$_{19}$S$_{27}$Br$_3$. Reproduced with permission from ref 174. Copyright 2015 The Royal Society of Chemistry. (e) Crystal structure model of hexagonal (Bi$_{19}$S$_{27}$I$_3$)$_{2/3}$. Reproduced with permission from ref 175. Copyright 2018 The Royal Society of Chemistry. (f) Crystallographic packing diagram of Bi$_{13}$S$_{18}$I$_2$ unit cell. Bismuth, magenta; iodine, purple; sulfur, yellow. The disordered bismuth is shown in gray/magenta with an occupancy factor of 0.25. Reproduced with permission from ref 176. Copyright 2019 The Royal Society of Chemistry. (g) Crystal structure of Bi$_{13}$S$_{18}$I$_2$. Inset shows the HAADF-STEM image of an as-sintered nano Bi$_{13}$S$_{18}$I$_2$, showing the hexagonal periodicity of I atoms as darker dots (green spheres) and Bi atoms as brighter dots (purple spheres). Reproduced with permission from ref 177. Copyright 2018 John Wiley and Sons. (h) Averaged cell representation (ACR) of the hexagonal P6$_3$ structure of Bi$_{13}$S$_{18}$I$_2$ viewed down the *c*-axis. Inset: normal to the *c*-axis to highlight bismuth (disordered/averaged dimer) sites, in hatched red. (i) Superstructure of Bi$_{13}$S$_{18}$I$_2$ in P$_3$ (where c′ = 2c). (1) Representation viewed down the *c*-axis, subvalent bismuth shown in teal. (2) Representation of 4–3′ Bi$_2$$^{4+}$ dimers (shown in teal) and their coordination spheres viewed perpendicular to the *c*-axis. (h, i) Reproduced with permission from ref 178. Copyright 2017 American Chemical Society.

hybrid halide perovskites owing to the increased strength of metal-chalcogen bonding.[75] To be specific, the metal-chalcogen interactions in chalcogenides are more covalent, leading to overall covalent bonding in the materials and hence higher stability, whereas the metal-halogen interactions in halide perovskites are less polar covalent.[84] On the other hand, a partial substitution of halide ions with chalcogen in chalcohalides offers a greater enthalpy of formation making them structurally more robust.

The Goldschmidt tolerance factor is used for the estimation of suitable components that form a stable perovskite structure at an empirical level. For chalcohalide perovskites, the tolerance factor is estimated to be 0.99 (e.g., MASbSI$_2$). However, detailed theoretical calculations revealed negative decomposition energies, suggesting that these chalcohalide perovskites may be difficult to synthesize experimentally under thermal equilibrium conditions.[72] The perfect crystal lattice of perovskite structure does not involve any lattice distortion arising from lattice strain

as well as any defect vacancies beyond the thermodynamic equilibrium conditions.[159−162] However, lattice strain and vacancies can originate during the materials synthesis and growth process, which are unavoidable and are highly detrimental to stability.[163−167] Since studies on these chalcohalide perovskites are at earlier stage, a thorough understanding of the origins and formation of lattice strain and vacancies is necessary. Though preliminary studies reveal the notable stability of chalcohalide materials, the question of whether these chalcohalides offer a synergy of good semiconducting properties of halides and good stability of chalcogenides is not entirely answered yet. The following sections may offer more insights into addressing this question.

## 3. STRUCTURAL CHEMISTRY

Unlike chalcogenide and perovskite, the difference in electronegativity in these mixed-anionic compounds invariably results in distinct bonding properties. High electronegative elements

prefer to bind with high electropositive elements, forming strong ionic bonds, whereas low electronegative elements prefer to coordinate with low electropositive elements, forming stable covalent bonds, resulting in unique crystal structures and physicochemical properties.[168] Since the chalcohalide cations (Sb(III), Bi(III), etc.) exhibit a second-order Jahn−Teller instability like Pb(II) and Sn(II) cations linked with changes in coordination environment from symmetric to asymmetric, the phenomenon of phase behavior can be linked to the $ns^2$ lone pair electrons.[150] Besides, the strength of both dangling-bond hybridization and orbital repulsion at band edges is also influenced by the crystal structure and so is a driving element in the electronic structure.[99] Moreover, defect tolerance is controlled by bonding behaviors that are an equilibrium of various competing factors such as ion coordination, bond length, hybridization, bonding character, crystal symmetry, oxidation state, Jahn−Teller distortion, etc. since it affects the energetic position of the defect charge transition level in the end.[97,146,152,169]

## 3.1. Heavy Pnictogen Chalcohalides

**3.1.1. Bi- and Sb-Based Chalcohalides.** Most of the reports on the MChX (M = Bi, Sb, Ch = S, Se, and X = Cl, Br, I) were founded on the orthorhombic crystal system with *Pnma and Pnam* space groups. Rod or needle-like morphology of these V−VI−VII ternary or pseudoquaternary materials is due to their structural characteristics. Figure 5a and b present the structures of BiSI and SbSI(Cl).[107,170] In BiSI or SbSI, when one chalcogen (Ch = S, Se) is replaced by two halogens, the $M_4S_6$ chain (from $Sb_2S_3$ or $Bi_2S_3$) splits into two $(M_2S_2X_2)$ chains. As an example, the crystal structure possesses the double chains of $[(MChX)_\infty]_2$ in the form of a binary screw axis linked together by a strong M-Ch (Sb/Bi-S/Se) covalent bond and the halogen anion has an ionic bond with a covalent binding bridge.[102] Double chains of $[(MChX)_\infty]_2$ grow parallel to the *c* axis with weak interchain van der Waals forces between the chains evolving in an anisotropic nature. As a result, the growth rate occurs more than 50 times parallel to the *c*-direction than that perpendicular to it, proved by Molnar et al.[171] Fong et al.[172] described in detail about the ionic−covalent bonding between cations and anions of these materials. Because M (Bi, Sb) atoms cannot provide enough charge for the chalcogen anions to form an ionic bond, Bi and Ch (Se) compromise by forming a covalent bond after electrons are transferred into the halogen anions. Therefore, the bonding between M and Ch is considered more covalent than the bonding between M and X.[172] The quasi 1D chains are composed of distorted pseudo-octahedra edge-sharing, which consists of 3 Bi−Ch and 2 Bi−I bonds with the vacant site occupying the Bi lone pair.[173] The vertical orientation of these chains on the substrate material could promote carrier transport and also reduce the charge recombination due to the parallel occurrence of enforced vertically aligned grain boundaries along the covalently bonded 1D axis.[133] As we transition from BiSI to BiSeI, the strength of the lone pair decreases, distorting the pseudo-octahedral lattice, and therefore a deviation in the bond angles. Therefore, charge density isosurfaces show the different electron densities (lower at VBM) surrounding the Bi ions in BiSeI making a kind of difference (Figure 5c). SbSI has also two phases that are linked by a ferroelectric distortion, where a small displacement along with the *z*-axis switches from ***Pnam*** (centrosymmetric, $D_{2h}$) to ***Pna2_1*** (noncentrosymmetric, $C_{2v}$) structures and vice versa.[74] Since the ferroelectric transition produces a single phase with spontaneous

polarization, SbSI is an excellent material for exhibiting both bulk and poly crystalline photoferroic effects.

**3.1.2. Derivatives of Bi-Based Chalcohalides.** Another Bi-based chalcohalide studied material is $Bi_{19}S_{27}X_3$ ($Bi_{19}S_{27}Cl_3$, $Bi_{19}S_{27}Br_3$, and $Bi_{19}S_{27}I_3$) (Figure 5d). It possesses few other isomorphic structures, like $Bi_{13}S_{18}I_2$, belonging to hexagonal crystal structure with $P6_3$ or $P6_3/m$ space group shown in Figure 5e−i.[175−178]

The very first report from this family is of $Bi_{19}S_{27}I_3$, reported by Miehe and Kupčik in 1971, which possesses a hexagonal crystal system with the space group $P6_3$.[179] Similarly, Bi-S-X based derivative $(Bi_{19}S_{27}X_3)$ shows the hexagonal crystal structure where three $(Bi_4S_6)$ chains are connected by two I atoms and an incomplete (2/3) occupation of one Bi atom, i.e., $Bi_{2/3}(Bi_4S_6)_3I_2$ and it becomes the $Bi_{19}S_{27}I_3$ as per the Daltonian formula (Figure 5d,e).[174,175] Though $Bi_{19}S_{27}I_3$ has been previously reported,[179,180] several conflicting reports exist on its true space group symmetry. Therefore, Groom et al.[178] reconsidered its crystal structure and newly proposed the $Bi_{13}S_{18}I_2$ in trigonal lattice with the *P3* space group. In this context, $Bi_{13}S_{18}I_2$ is proposed as a typical complex structure corresponding to the trigonal lattice shown in Figure 5f, g, and h. The structural complexity was resolved by using single-crystal X-ray diffraction (XRD) and synchrotron powder diffraction. In $Bi_{13}S_{18}I_2$, the ribbon-like subunits of $(Bi_4S_6)_\infty$ form six spokes around a central hexagonal channel at the corners of the unit cell and the iodine in the structure is located between the spokes in triangular channels.[177,178,181] According to the work by Xu et al.,[177] $Bi_{13}S_{18}I_2$ exhibits four sites for disordered Bi(X), each with a 1/4 occupancy and the disordered Bi(X) atoms at the (1/3, 2/3, z) sites coordinate with six S atoms to form a wheel-like cluster (Figure 5g). The Bi-S coordination forms in these structures are the same as those in $Bi_2S_3$, and these Bi and S atoms construct a 3D structure and create two 1D tunnels propagating in each unit cell along the [001] axis, in which I atoms reside. The inset of Figure 5g shows the HAADF-STEM image of $Bi_{13}S_{18}I_2$, showing the hexagonal periodicity of Bi and I atoms. The averaged cell representation (ACR) of the hexagonal $P6_3$ structure of $Bi_{13}S_{18}I_2$ viewed down the *c*-axis is represented in Figure 5h, and Bi (disordered/averaged dimer) sites are highlighted in the inset. After a thorough study on the $Bi_{13}S_{18}I_2$ structure, Groom et al.[178] reported the charge-balance when solved in the *P3* space group with $Bi_2^{4+}$ dimers as $(Bi^{3+})_{12}(Bi_2^{4+})_{0.5}(S^{2−})_{18}(I^−)_2$. The corresponding chain of dimers and their coordination spheres resulting from the superstructure and partial occupancy is shown in Figure 5i. The presence of $Bi_2^{4+}$ dimer units in this material was further confirmed from a presence of a weak peak at 106 cm$^{−1}$ in the Raman spectrum and redox chemistry from thermal decomposition.[178,181]

## 3.2. Transition/Post-transition and Mixed-Metals Chalcohalides

Manna and co-workers studied the crystal structures of Pb-based chalcohalides ($Pb_4S_3Br_2$, $Pb_3S_2Cl_2$, and $Pb_4S_3I_2$) from 3D electron diffraction and electron tomography of a single nanocrystal (NC), XRD, and DFT calculations.[112] They proposed that the Pb atoms possess three different coordination environments, where two Pb sites are surrounded by 4 S + 4 Br and one Pb atom surrounded by 6 (S + 2 Br), whereas S possesses two nonequivalent crystallographic sites and Br resides in a heptacoordinated pentagonal bipyramidal site. The structural varieties in these chalcohalides could originate from the different geometries of the basic structural units;
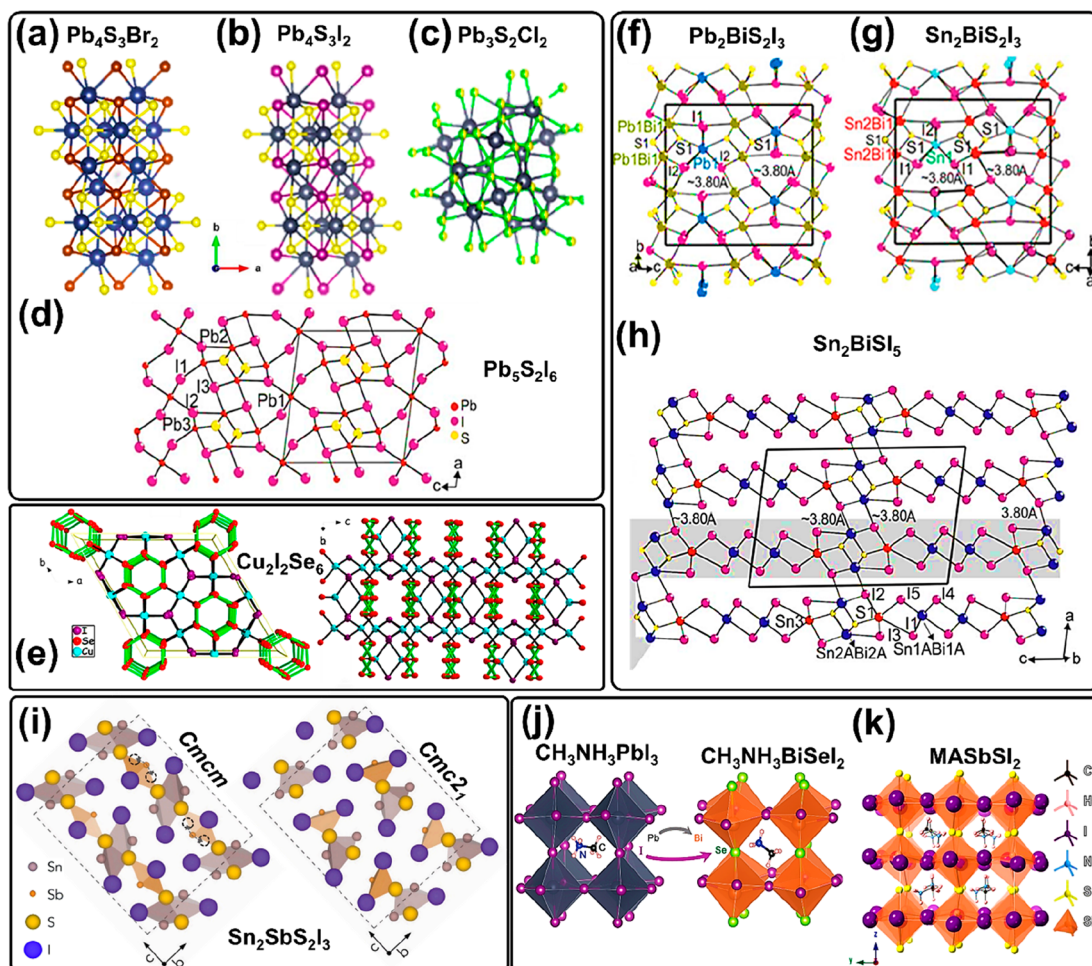
**Figure 6.** (a) $Pb_4S_3Br_2$, (b) $Pb_4S_3I_2$, (c) $Pb_3S_2Cl_2$. (a−c) Reproduced with permission from ref 112. Copyright 2020 American Chemical Society. (d) $Pb_5S_2I_6$. Reproduced with permission from refs 109 and 183. Copyright 2016 American Chemical Society and 1973 John Wiley and Sons. (e) $Cu_2I_2Se_6$ representing the view of the unit cell along the $c$-axis and ab-plane. Reproduced with permission from ref 111. Copyright 2018 American Chemical Society. Crystal structures of (f) $Pb_2BiS_2I_3$, (g) $Sn_2BiS_2I_3$, (h) $Sn_2BiSI_5$. (f−h) Reproduced with permission from ref 109. Copyright 2016 American Chemical Society. (i) Calculated crystal structures for $Cmcm$ and $Cmc2_1$ polymorphs of $Sn_2SbS_2I_3$, in the conventional orthorhombic unit cell. The empty circles show equivalent shifts in Sb position that correspond to the $Cmcm$ to $Cmc2_1$ transition. Reproduced with permission from ref 185. Copyright 2021 The Royal Society of Chemistry. (j) Atomic structures of $CH_3NH_3PbI_3$ and $CH_3NH_3BiSeI_2$ and a illustration of the split-anion approach to replace Pb in $CH_3NH_3PbI_3$. Reproduced with permission from ref 73. Copyright 2016 The Royal Society of Chemistry. (k) $MASbSI_2$ proposed from DFT relaxation. Reproduced with permission from ref 72. Copyright 2018 American Chemical Society.

otherwise, they show a similar coordination environment (Pb = octacoordinated, Cl, S = deformed octahedral) presented in Figure 6a−c. The crystal structure of $Pb_3S_2Cl_2$ NCs, as shown in Figure 6c, reported by Manna and co-workers closely resembles that of bulk $Pb_3Se_2Br_2$ reported by Ni et al.[182] In $Pb_3Se_2Br_2$, the Pb-centered dodecahedrons consist of eight corners and twelve faces that connect neighboring dodecahedrons through sharing 8 corners, 4 edges, and 8 faces by filling the space of the unit cell, i.e., anion-centered octahedra formed with 6 Pb atoms at its vertexes.[182] This results in a compact structure leaving no space between the polyhedra.[182] However, the $Pb_4SeBr_6$ material synthesized at ambient pressure exhibits different coordination environment.[183] Pb occupies three different Wyckoff positions (2a, 2b, and 4d) in $Pb_4SeBr_6$ resulting in different coordination polyhedron and ultimately three types of Pb-centered polyhedra. It builds up chains along an axis by sharing edges (Pb1) or faces (Pb2 and Pb3) linked with each other by shared corners, edges, and faces leaving space between polyhedra.[182,183] Unlike $Pb_3Se_2Br_2$, Pb atoms in $Pb_4S_3I_2$ exhibited three different types of chemical environments.[184] The one type (Pb1) of atom

that accounts for half of the Pb atoms in the crystal structure occupies 8d sites and is surrounded by 4 iodine and 3 sulfur atoms in a distorted 7-fold coordination. Among two different types of S atoms, one S (S1) atom occupies intralayer vertices and another (S2) atom occupies common vertices between different sheets. There is a sawtooth type of shape formation to the chains due to the interaction between short distanced Pb1 and Pb2 atoms. This type of polyhedra yields edge-sharing double-layer sheets along the $b$-axis. The remaining two Pb atoms (Pb2 and Pb3) occupy 4c sites coordinated by 6 sulfur atoms, or 3 sulfur plus 2 iodine atoms, respectively, with both atoms linked by forming zigzag type chains along the same $b$-axis generating another sheet. $Pb_5S_2I_6$ exhibits a crystal structure (Figure 6d) same as $Sn_2BiSI_5$ (explained afterward and presented in Figure 6h), where $Pb_5S_2I_6$ chains are separated by one $[PbI_6]$ octahedra instead of two as is the case for $Sn_2BiSI_5$.[183]

Kanatzidis and co-workers reported the crystalline and air-stable $Cu_2I_2Se_6$ as a wide indirect bandgap semiconductor material, possessing a 3D structured metal−inorganic frame-

work consisting of $[Cu_2I_2]$ nodes and $Se_6$ linkers.[111] $Cu_2I_2Se_6$ crystallizes in the rhombohedral $R\overline{3}m$ space group (Figure 6e) and is composed of coordinatively unsaturated $[Cu_2I_2]$ dimers linked together through molecular $Se_6$ rings. They reported that the $[Cu_2I_2]$ nodes are formed through symmetric bridging of the two Cu metals with two I ions. The remaining two more coordination sites per Cu ion are occupied by two Se atoms from two adjacent $Se_6$ rings to complete a tetrahedral coordination geometry around the $Cu^I$ ions. This material showed comparatively enhanced electron transport along the crystallographic ab-plane, which is superior to the similar structure of the rhombohedral Se.[111] The presence of $ns^2$ electronic configurations also makes this material resistant to oxidation due to the presence of an inert electron pair.[108]

The lone-pair properties of A(II) and B(III) cations control the majority of the structural behavior in the $A_2BCh_2X_3$ system. Kanatzidis and co-workers in their following works reported stable, n-type, quaternary sulfoiodides $Pb_2BiS_2I_3$, $Sn_2BiS_2I_3$, and $Sn_2BiSI_5$ as statistical disordered materials.[109] The $Pb_2BiS_2I_3$ and $Sn_2BiS_2I_3$ exhibit similar crystal structures; orthorhombic phase (space group, $Cmcm$) as shown in Figure 6f and g, whereas $Sn_2BiSI_5$ crystallizes in monoclinic form (space group $C2/m$) as shown in Figure 6h. Parallel infinite chains of $[(Pb_{0.5}Bi_{0.5})_2S_2]$ and $[(Sn_{1-x}Bi_x)_2S_2]$ ($x \approx 0.5$) extend along the crystallographic a-axis and are interconnected by trigonal prismatic $[PbI_6]$ and $[SnI_6]$ polyhedra. The 2D nature of the crystalline structure and weak interaction between metals (Pb, Bi, Sn) and I provide the materials with a 3D view (Figure 6f−h). Unlike $Pb_2BiS_2I_3$ and $Sn_2BiS_2I_3$, $Sn_2BiSI_5$ chains are interconnected by a trigonal prismatic $[SnI_6]$ and two $(Sn_{1-x}Bi_xI_6)$ octahedral units and extend along the crystallographic c direction.

Recently, Walsh and co-workers performed geometry optimizations for $Sn_2SbS_2I_3$ in both $Cmcm$ and $Cmc2_1$ space groups stating that the centrosymmetric $Cmcm$ crystal structure represents an average over multiple polar $Cmc2_1$ configurations.[185] Unlike the previously reported $Pb_2BiS_2I_3$ and $Sn_2BiS_2I_3$, the authors highlighted that the $Cmcm$ structure consists of infinite chains of $(Sn_2S_2I_2)_n$ along the a direction and is firmly packed along the b direction to create layers in the ab plane. The $(Sn_2S_2I_2)_n$ chains are made up of face-sharing $SnS_3I_2$ pyramids with a parallelepid $S_2I_2$ base and an apical sulfur atom. Sb and I atoms are located between layers, yielding the overall $(Sn_2SbS_2I_3)_n$ stoichiometry (Figure 6i, left). While the $Cmc2_1$ crystal structure consists of $(Sn_2SbS_2I_3)_n$ chains along the a direction, as the Sb atoms attach to the $(Sn_2S_2I_2)_n$ layers (Figure 6i, right). Both polymorphs have identical a and b cell lengths, with the major difference appearing in the c direction because the Sb lone-pair is oriented toward halide-bordered voids in both polymorphs; either along the interchain gap (b direction) for $Cmcm$ symmetry or toward the interchain gap (c direction) for $Cmc2_1$, with more marked localization observed in the $Cmc2_1$ instance. The authors stated that the dynamic stereochemical activity of the Sb lone-pair is one of the key driving reasons behind the production of the deformed, lower-symmetry $Cmc2_1$ polymorph via a second order Jahn−Teller instability, which is common in lone-pair chalcogenides.[150,185]

## 3.3. Hybrid Organic−Inorganic Metal Chalcohalides

Recently, attempts have also been made to explore the crystal structures of emerging 3D mixed anion Pb-free chalcohalide perovskite materials using computational screening based on first-principle calculations. Sun and co-workers reported a high-throughput screening of the mixed anion Pb-free chalcohalide perovskites for PV applications with the formula of ABChX (where A = $Cs^+$, $CH_3NH_3^+$, and $HC(NH_2)_2^+$; B = $Ga^{3+}$, $In^{3+}$, $Sb^{3+}$, and $Bi^{3+}$; Ch = $O^{2-}$, $S^{2-}$, $Se^{2-}$, and $Te^{2-}$, and X = $F^-$, $Cl^-$, $Br^-$, and $I^-$) and found that these materials exhibit crystal structures similar to Pb-based halide perovskite.[73] In another study, the crystal structures of $CH_3NH_3BiSeI_2$ and $MASbSI_2$ (Figure 6j,k) were also studied and revealed the cubic otherwise distorted structure after the addition of chalcogen.[72,73] The 3D $MASbSI_2$ perovskite is hypothesized to be in a cubic phase with MA molecules aligned in an antiferroelectric configuration.[186] It was discovered to be more energetically stable than other configurations, with sulfur atoms holding the apical sites of the octahedra (along the z-axis); however, thorough conclusions on the crystal structures have not yet been discussed. Indeed, the atomic structures of few hybrid metal chalcohalides appeared to be more complex than that of an ideal perovskite $ABX_3$.[187] This is because, while chalcogen atom benefits the hybrid metal chalcohalides, the two anion elements, Ch and X, may exhibit structural ordering and disordering, affecting stability. Such Ch-X anion ordering affects both bandgaps and formation enthalpies, and this ordering-induced bandgap variation may also result in large Urbach tails.

# 4. THEORETICAL BAND STRUCTURES AND ELECTRONIC PROPERTIES

## 4.1. Heavy Pnictogen Chalcohalides

The optical properties of materials are a key factor for energy-related applications. Owing to heterogeneous composition due to mixed anions, chalcohalides are considered sensitive during theoretical calculations. The true bandgap of chalcohalides is also under discussion since the band diagrams vary depending on the approximation level used during theoretical calculations. Different methodologies, calculations, and approximations (along with DFT) have been used to calculate the bandgap and band dispersion and to give insights into the optoelectronic properties of chalcohalides. Ab initio and first-principles calculations, GGA, HSE, and quasiparticle GW methods have been used to investigate the electronic structures and different optical features to their corresponding interband transition of chalcohalides. In this section, we review the advances made in chalcohalide materials using theoretical simulations and discuss ongoing studies that serve as a bridge between the structures and properties described in section 2.

**4.1.1. Bi-Based Chalcohalides.** It is a general phenomenon that the substitution of Se lowers the bandgap due to a variation in the lattice parameters. Similarly, the indirect bandgap was tuned between 1.63 and 1.48 eV by incorporating Se into BiSI.[106] However, a direct bandgap of about 1.27 eV would result from the 100% Se-doping (BiSeI). Unlike $CdS_{1-x}Se_x$ or $CdSe_xTe_{1-x}$, the VBM of BiSI is predicted to consist mainly of I 5p orbitals, rather than S 3p, which did not cause any noticeable shift and were largely similar regardless of the Se content. This is ascribed to the defect states introduced just above the VBM of BiSI after Se doping. As mentioned earlier, the SOC has a strong influence on the band extrema energies, but which have not been considered in prior research.

Brandt et al.[97] observed that Bi-based chalcohalides possess a larger contribution of SOC in the CB than Sn- and Sb-based chalcohalides. Therefore, Bi-based chalcohalides were proposed to be the most suitable for achieving similarly shallow anion vacancy levels as in $MAPbI_3$ perovskite. However, both SbSI and BiSI show similar antibonding s-orbital contributions at the
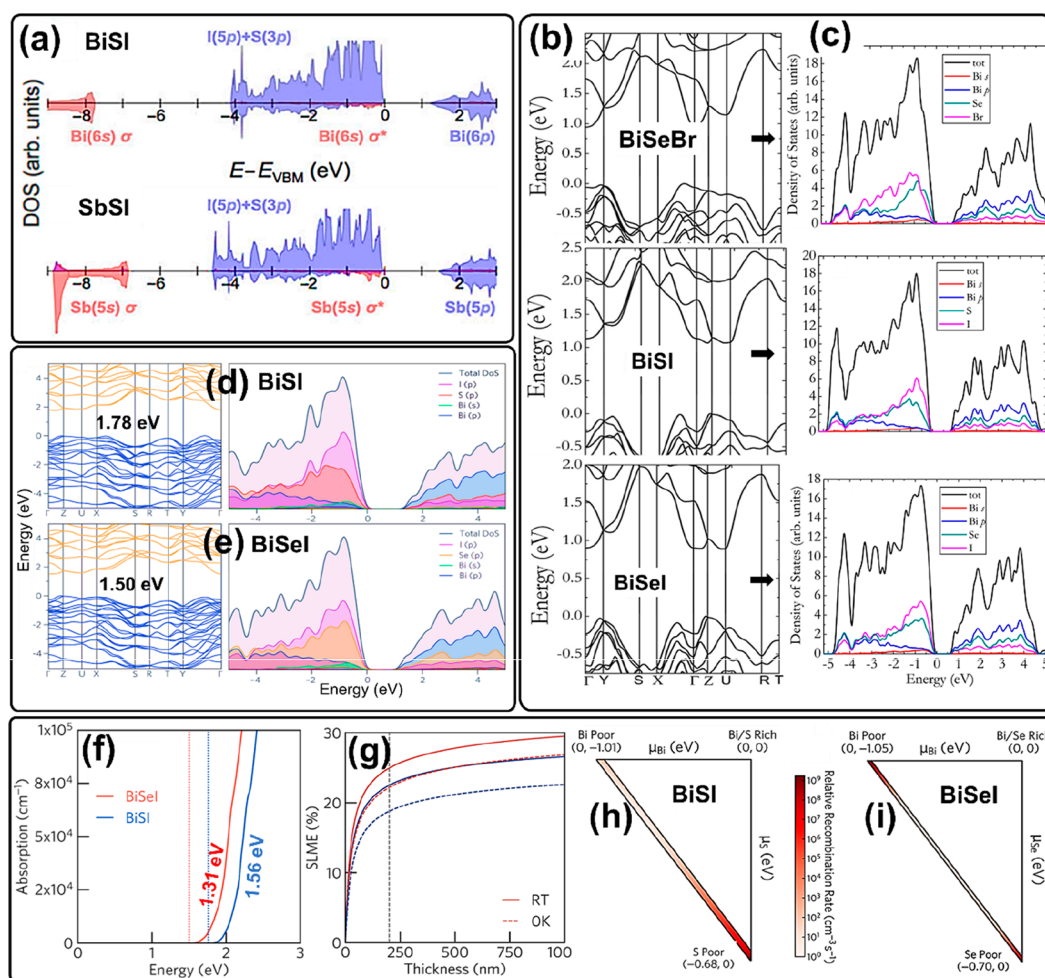
**Figure 7.** (a) DOS for BiSI and SbSI compounds. The pDOS are separated into atomic orbital contributions, with anions on the positive *y*-axis and cations on the negative. The cation s states are classified into bonding σ (lower energy) and antibonding σ* (higher energy) orbitals. Reproduced with permission from ref 97. Copyright 2015 Cambridge University Press. (b) Band structures for BiSeBr, BiSI, and BiSeI, and (c) their corresponding calculated DOSs using Perdew-Burke-Ernzerhof (PBE) functionals including the spin−orbit coupling. (b, c) Reproduced with permission from ref 143. Copyright 2016 American Physical Society. (d, e) Band structures and ion decomposed partial and total DOS of BiSI and BiSeI, respectively, along with the high symmetry directions. In all cases, the VBM is set to 0 eV. (d, e) Reproduced with permission from ref 133. Copyright 2016 The Royal Society of Chemistry. (f) Optical absorption of BiSI (blue) and BiSeI (red) calculated using hQSGW at 0 K. Fundamental band gaps ($E_g^{hQSGW}$) are shown by dotted lines. (g) SLME of BiSI and BiSeI calculated using the 0 K-band gaps and optical absorption (dashed lines) and results extrapolated to RT (solid lines). (h, i) Shockley-Read-Hall recombination (RSHR) rate across the range of accessible chemical potentials for BiSI and BiSeI, respectively. The darker regions of red represents the greater levels of recombination. (f−i) Reproduced with permission from ref 173. Copyright 2018 American Chemical Society.

VBM and the corresponding DOS of both are shown in Figure 7a. In mixed halide ions, e.g., $BiSBr_{1−x}I_x$, VB is formed with a higher contribution of the I 5*p* orbitals, as compared with that of Br 4*p*, because the absorption edges were continuously shifted toward longer wavelengths (1.71 to 1.51 eV) with increasing *x* values.[76] On the other hand, S 3*p* also plays an important role in the formation of VB. Substitution of $O^{2−}$ to $S^{2−}$ anion in $BiOBr_{1−x}I_x$ resulted in the significant shift with each corresponding spectrum of $BiOBr_{1−x}I_x$ of the absorption edges toward longer wavelength in the range of 150−260 nm, suggesting the contribution from high-energy S 3*p* orbitals to VB formation. Research on single Se-based Bi chalcohalides has gained attraction following this report. Shi et al.[143] thus thoroughly studied the electronic structures, dielectric properties, optical absorption, and defect properties of BiSeBr, BiSeI, and BiSI by DFT calculations. The calculated band structures (Figure 7b) and DOSs (Figure 7c) show that BiSeBr and BiSI are *n*- and *p*-type, respectively, whereas BiSeI induces substantial

VB dispersion in parallel and perpendicular directions to the atomic chains due to the strong interchain iodine binding. These inspiring results as outcomes from DFT calculations suggest their potential application in PV devices, transparent conducting materials, etc. They also reported the enhanced Born effective charges, resulting in strong lattice polarization and large static dielectric constants for all of these materials, and also proved that the subsequent strong screening of charge defects and impurities decreased the carrier scattering and trapping. The defects formed by Se and the Br vacancies in BiSeBr were both shallow donors and therefore did not effectively trap electrons, allowing efficient electron transport. These defects are attributed to the strong screening (suppresses coulomb potential) and low coordination numbers of anions that lead to a weak hybridization among Bi 6*p* orbitals at an anion vacancy. In-depth studies on the electronic structures using hybrid DFT with the addition of SOC were still necessary to underpin the properties of the band structure. With this motivation, Ganose et al.[133]
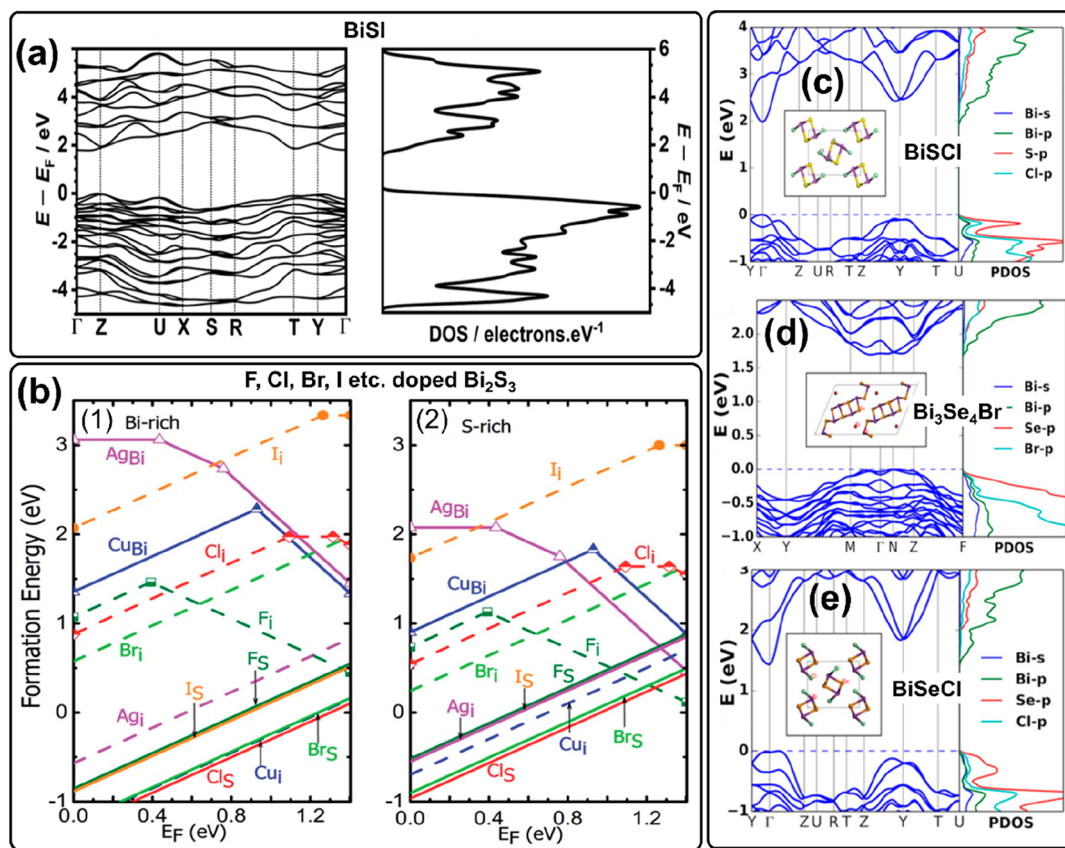
**Figure 8.** (a) Band structure and DOS of paraelectric BiSI calculated using GW@PBE0 formalism. The VBM and CBM are situated at points between Γ−Y and Γ−Z paths, respectively. Reproduced with permission from ref 190. Copyright 2019 American Chemical Society. (b) Calculated formation energies of F, Cl, Br, I, Cu, and Ag dopants at different sites, as a function of Fermi levels under (1) Birich and (2) S-rich conditions. Reproduced with permission from ref 191. Copyright 2017 The Royal Society of Chemistry. Crystal structure, band structure, and partial density of states (DOS) of (c) BiSCl, (d) $Bi_3Se_4Br$, and (e) BiSeCl. (c−e) Reproduced with permission from ref 75. Copyright 2018 Nature Publishing Ltd.

studied the BiSI and BiSeI materials by relativistic hybrid DFT, with the addition of SOC to show the promises of these materials in a PV device. As a result, BiSI and BiSeI showed the theoretical band gaps of 1.78 and 1.50 eV, respectively (Figure 7d and e, left panel). The difference with the experimental band gap is due to the absence of thermal effects, including lattice expansion and electron−phonon coupling during the DFT calculation. In the relativistic renormalization of the BiSI and BiSeI, CBs were found to exceed 0.6 eV, underlining the importance of including SOC effects in modeling these material systems. The band structures of these materials revealed several band extrema's, mostly located in the Brillouin zone, away from high-symmetry points. Also, the presence of large DOS (Figure 7d and e, right panel) at the band edges and larger absorption coefficients of greater than $1 \times 10^5$ cm$^{-1}$ seen roughly at 0.5 eV above the absorption edge makes these materials ideal solar absorbers. The VB energies (ionization potentials (IPs)) of BiSI and BiSeI were found to be 6.4 and 6.2 eV below vacuum level, respectively. The reduction in the bandgap is caused due to decrease in the IP (an increasing electron affinity) of BiSeI, which lowers the CBM relative to the vacuum level. Crystal Orbital Hamilton Population (COHP) was also used to study the stereoactivity of the antibonding states of the cations and thus the energy band formation mechanism.[133] The scalar-relativistic contraction of the Bi6s shell causes relatively diffused and therefore weakly stereoactive lone pairs, which produces the asymmetric electron density resulting in small pseudo-octahedral distortion of the lattice.[133,150] The charge density

isosurfaces also show the lower electron density surrounding the Bi ions at the top of the VB. The proof for the distortion in the pseudo-octahedral lattice and hence the deviation in the bond angles, which depends on the strength of the lone pair and decreases when moving from BiSI to BiSeI, is previously shown in Figure 5c. Also, the differences between the direct and indirect band gaps are small despite possessing indirect band gaps, indicating the indirect nature will have minimal effect on optical absorption and make these materials better alternatives in targeted application.

The same group later studied the optoelectronic properties using quasiparticle self-consistent GW (QSGW) theory.[173] Small effective electron masses in the direction of the BiChI (Ch= S, Se) chains coupled with extremely strong optical absorption just above the bandgap attributed to the high DOS on the band edges. As per the Boltzmann transport theory, temperature-dependent effective masses in the 1D direction are found to be relatively small and strongly anisotropic. Both BiSI and BiSeI exhibited smaller effective electrons masses than those of holes. The band gaps for BiSI (1.76 eV) and BiSeI (1.50 eV), calculated using hybrid QSGW, are in close agreement with previous hybrid DFT results and the temperature corrected band gaps of 1.56 eV (BiSI) and 1.31 eV (BiSeI) are in good agreement with the RT experimental optical band gaps (Figure 7f).[173,188,189] A strong optical absorption in combination with ideal bandgaps results in high spectroscopically limited maximum efficiencies (SLME) of 25.0 and 22.5% for BiSeI and BiSI, respectively, at small thin film thicknesses and is
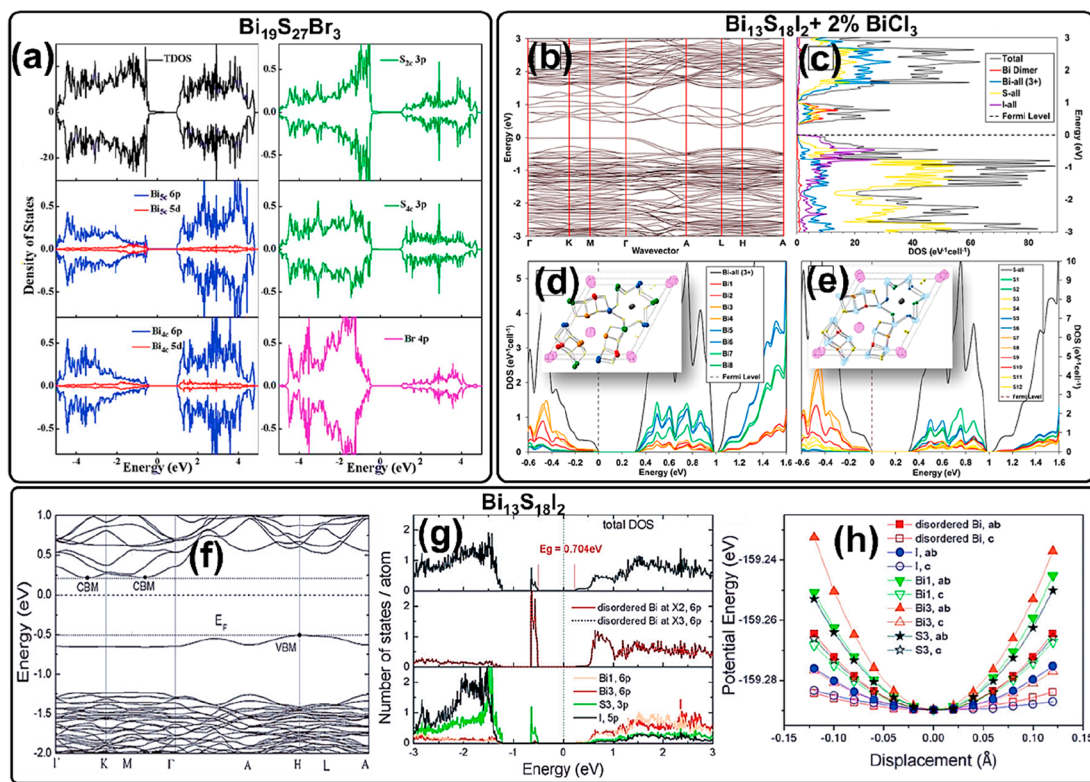
**Figure 9.** (a) DOS for $Bi_{19}S_{27}Br_3$. Electronic structure data calculated for the 2−1′ dimer supercell model of $Bi_{13}S_{18}I_2$. The Fermi level is set at 0 eV. Reproduced with permission from ref 174. Copyright 2015 The Royal Society of Chemistry. (b) Band structure, (c) corresponding DOS plot with 2−1′ dimer contribution in red, (d) trivalent bismuth ($Bi^{3+}$) pDOS (line colors correspond to atom colors in inset) and their contribution at $Bi_2^{4+}$ dimer energies, and (e) sulfur pDOS (line colors correspond to atom colors in inset) and their contribution at $Bi_2^{4+}$ dimer energies. (b−e) Reproduced with permission from ref 178. Copyright 2017 American Chemical Society. (f) Electronic band structure, (g) DOS, and (h) potential wells of $Bi_{13}S_{18}I_2$. (f−h) Reproduced with permission from ref 177. Copyright 2018 John Wiley and Sons.

comparable with the best-known PV absorbers (Figure 7g). They also identified the chemical potential space regions with reduced recombination rates by ~$10^7$ cm$^{-3}$ s$^{-1}$ under accessible experimental conditions that guide researchers to produce more efficient solar-energy conversion devices based on Bi-based chalcohalides. The calculated recombination rate across the range of accessible chemical potentials for BiSI and BiSeI is shown in Figure 7h and i. The p-type BiSI exhibited the lowest rate of recombination due to the relatively high energy formation of the dominant deep defects ($S_{Bi}$ and $V_S$), leading to low concentrations of these defects compared to the total number of charge carriers. On the other hand, the rate of recombination increases gradually (over $10^7$ s$^{-1}$ than p-type) in the case of n-type BiSI due to a lowering in the energy of the ultradeep $V_S$ and $Bi_S$ defects. As a result, it has been shown that Bipoor BiSI is essential to reduce the effect of unwanted recombination on the open-circuit voltage ($V_{oc}$) in PV devices. Moreover, both the p- and n-type BiSeI show high levels of recombination due to ultradeep transition defects of both types ($Se_{Bi}$ for p-type and $Bi_{Se}$ and $V_{Se}$ for n-type). Thus, it is concluded that the QSGWp offers additional accuracy and many details in the analysis as compared to the DFT methods.

In this regard, further advances in theoretical research were achieved by applying GW@PBE0 functions to the calculation of the band structure and DOS of BiSI (Figure 8a).[190] A fundamental indirect bandgap is observed at 1.77 eV (at 0 K), while a direct bandgap transition is observed at 20 meV higher energy compared to the experimental values of indirect and direct band gaps of 1.50 and 1.62 eV, respectively. The

electron−phonon coupling effects could be the possible reason behind this difference between the indirect and direct band gaps. The ionization potential (IP) of the BiSI is estimated to be 6.33 eV. Moreover, it also observed that the CB is more dispersed than the VB due to SOC effects induced by $Bi^{3+}$, resulting in a smaller effective mass of electrons ($m_e^* = 0.53\ m_0$) in comparison to holes ($m_h^* = 0.95\ m_0$). Doping in $Bi_2S_3$ by a series of extrinsic elements (F, Cl, Br, I, and some cations) was also investigated (Figure 8b).[191] It was discovered that these elements prefer to substitute the S anion as the energetically favorable doping site. This allows much lower formation energies of $F_S$, $Cl_S$, $Br_S$, and $I_S$ substitution than those of $F_i$, $Cl_i$, $Br_i$, and $I_i$ interstitials, i.e., 0.2−0.5 eV (under Birich, S-poor conditions) and 0.5−0.8 eV (under Bipoor, S-rich conditions) ($E_F$ = CBM). This implies that very high electron carrier concentrations can be produced in $Bi_2S_3$. Moreover, $Cl_S$ showed the lowest formation energy and the $F_S$ and $I_S$ have almost degenerate energy levels due to the smallest size difference between Cl and S. Birich condition increased the n-type conductivity after Cl and Br doping as well suppressed the deep-level recombination centers. Given the relatively low CB and high n-type conductivity, it is predicted that Cl and Br doped $Bi_2S_3$ under the Birich condition acts as an ideal candidate for the electron acceptor or counter electrode; however, the performance of $Bi_2S_3$ as a light-absorber or sensitizer material is intrinsically limited.

To date, major theoretical studies have been focused on Bi-based chalcoiodides, while findings on chalcochlorides have been lacking until BiChCl be a promising material for

optoelectronic applications. Ran et al.[75] calculated the band structures and pDOS of BiSeCl, BiSCl, and $Bi_3Se_4Br$ and found that all these materials exhibit indirect band gaps in the range of $\sim 1.0-1.7$ eV (Figure 8c–e). In particular, CBM is found to be located at G, whereas VBM along the G-Z direction in BiSeCl. The CBs are highly dispersive both parallel ($\Gamma$-Z direction) and perpendicular ($\Gamma$-X and $\Gamma$-Y direction) to the chain direction ($kz$) due to the extended Bi-$p$ states. On the other hand, VBs are dispersive in a direction parallel to the atomic chains ($\Gamma$-Z direction), but less perpendicular ($\Gamma$-X and $\Gamma$-Y direction) to the chain due to the weak Se–Se interchain coupling compared with that of intrachain coupling. The band structures of BiSCl (and hence BiSBr/I) are similar to BiSeCl (BiSeBr/I) except that the former have larger band gaps due to the deeper S-$p$ states as compared with Se-$p$ states. Although the VBs within this group of materials consist primarily of anion $p$ states (S-$p$ and halogen-$p$), the contributions from halogen-$p$ states near the VBM increase as the halogen ion changes from Cl to I. The relatively flat VBs further resulted in larger hole effective masses than $m_0$, while spatially extended Bi-$p$ states led to low electron effective masses than $m_0$. The calculated band structure of $Bi_3Se_4Br$ suggested that the CBM is located at $k$ point along the G-M direction and VBM along the N-Z direction and both turn out to be dispersive in nature. The pDOS plot shows that the VB is dominated by anion $p$ states and hybridize with Bi $6s$ orbital to form antibonding states, whereas CB is primarily derived from Bi $6p$ states. These findings suggest that further investigation of these materials to determine their dopability, defect and dielectric behavior, and the possibility of obtaining high resistance (for detector) is necessary to evaluate other properties relevant to optoelectronic applications.

Other derivatives of $Bi_{III}$-VI–VII compounds such as $Bi_{19}S_{27}X_3$, $Bi_{13}S_{18}I_2$, etc. have also been attracted a great interest ranging from catalysis to electronics due to their interesting characteristics. It has encouraged researchers to further investigate their properties using theoretical methods such as ab initio, first-principle calculations, and DFT. A notable study has been reported by Li and co-workers to deeply understand the electronic structure of $Bi_{19}S_{27}Br_3/I_3$ using DFT calculations performed with the Vienna ab initio simulation and a projector augmented wave method by using GGA with the spin-polarized Perdew-Burke-Ernzerhof (PBE) functional.[174] It has been revealed that the VBM of $Bi_{19}S_{27}Br_3$ and $Bi_{19}S_{27}I_3$ is composed of S $3p$ states, whereas the CBM mainly consists of Bi $6p$ states with slightly mixed with S $3p$ orbitals (Figure 9a). On the other hand, Br $4p$ or I $5p$ orbitals significantly contributed to lowering the VB region, i.e., to lower than $-0.4$ eV, which is why possibly replacing Br with I did not change the bandgap of the as-synthesized materials. The theoretically calculated bandgap of 0.6 eV was smaller than the experimental band gap of 0.82 eV, which was attributed to the shortcomings of the GGA method in underestimating the bandgap. They further studied the adsorption and desorption behavior of iodine species on the $Bi_{19}S_{27}Br_3$ via DFT and demonstrated a reversible adsorption behavior of iodine species, showing its potential application as counter electrode in dye sensitized solar cells (DSSCs).[192]

Since that report, research has recently been moved to study $Bi_{13}S_{18}I_2$. The band structure diagram and corresponding DOS plot with 2−1′ dimer contribution is shown in Figure 9b and c, respectively. A study on the anisotropy in the $Bi_{13}S_{18}I_2$ material was proven from the VBM, which is dominated by iodine and sulfur states and the flatness of the iodine states demonstrates strongly localized bands along with certain directions.[178]

Besides, the corresponding pDOS of trivalent bismuth ($Bi^{3+}$) with their contribution at $Bi_2^{4+}$ dimer energies and sulfur p-DOS with their contribution at $Bi_2^{4+}$ dimer energies are presented in Figure 9d and e, respectively. These results show that the CBM is dominated by unfilled $Bi^{3+}$ $6p$ states, 1 eV above the $E_F$ and the $Bi^{2+}$ states ($6p$) from $Bi_2^{4+}$ dimer (red) located between 0.3 and 1 eV above $E_F$. These disordered, partially occupied subvalent bismuth dimers along with their adjacent bonded sulfur and bismuth sites generated a group of "states in the gap" between the VB and CB, which made the dominant contribution to the bands in the gap with much smaller contributions from the $Bi_4S_6$ units and iodide states. The electronic band structure and total DOS of $Bi_{13}S_{18}I_2$ show the band gap of $\sim 0.70$ eV, which is nearly similar to the previously reported band gap of 0.82 eV (Figure 9f,g).[177] The double band extrema at the CBM located between the high symmetry points, G-M, and G−K, in the Brillouin zone exhibited the high degeneracy and moderate effective mass of the electron. Authors attributed this to increased symmetry in $Bi_{13}S_{18}I_2$ (trigonal) as compared to $Bi_2S_3$ (orthorhombic). In addition, the disordered Bi(X) and I atoms show the flattest potential wells (Figure 9h) as compared to S and other Bi atoms along the $c$-direction, indicating the weaker bonding of Bi(X) and I atoms to the nearby atoms than the other atoms. This study concludes that the lower bandgap value of $Bi_{13}S_{18}I_2$ along with its dimer property, suitable band structures, flat potential wells, is likely to have low thermal conductivity and potentially a high Seebeck coefficient and electrical conductivity making this material suitable for thermoelectric properties.

### 4.1.2. Sb-Based Chalcohalides.

Sb-based chalcohalides are the second family after Bi-based chalcohalides which are most studied ternary compounds, usually formed of a trivalent Sb cation with divalent (S or Se) and monovalent (I, Br) anions, for their optical, electrical, and ferroelectric properties. Early work on the band structure calculation of SbSI was reported by Nako and Balkanski in 1973 using the pseudopotential method in the para- and ferroelectric phases.[193] They found that the material exhibits an indirect band gap ($\sim 1.4$ eV) in both phases and the smallest direct band gap, which exists at the U point on the surface of the Brillouin zone and brings dichroism in the absorption edge. However, several characteristics of the band structures in the complex structure were not considered during the band structure calculations, which might have led to a lower band gap value in SbSI. Audzijionis et al.[194] further revealed that the upper part of the VB of SbSI is formed by S-$3p$ orbitals, and the lower part of the CB bottom of Sb-$5p$ orbitals from the total DOS using empirical pseudopotential method. Alward and Fong later shed a light on the VB structure of Sb-based chalcohalides in detail.[68] They observed that all the Sb-chalcohalide materials, namely SbSI, SbSBr, and SbSeI, exhibit indirect band gaps of $\sim 2.11$, 2.18, and 1.67 eV, respectively. Among all the constituents of Sb-chalcohalides, Sb is the least electronegative, whereas the halides are the most electronegative. Thus, the lowest unoccupied states originate from the Sb $sp$ states, while the occupied I or Br $sp$ states lie the farthest below the top of the VB. This further explains that the largest portion of the occupied states at the gap must come from the $sp$ states of the S or Se and the remaining states of Sb. Since S atoms are more electronegative than Se, the bond between S and Sb should be more ionic than the bond between Se and Sb, which further concludes the lower band gap in SbSeI than the SbSI and SbSBr. Akkus and Mamedov then reported the electronic structure and linear optical properties of the ferroelectric phase of SbSeI using the DFT in the GGA.[195] Unlike the previous band structure
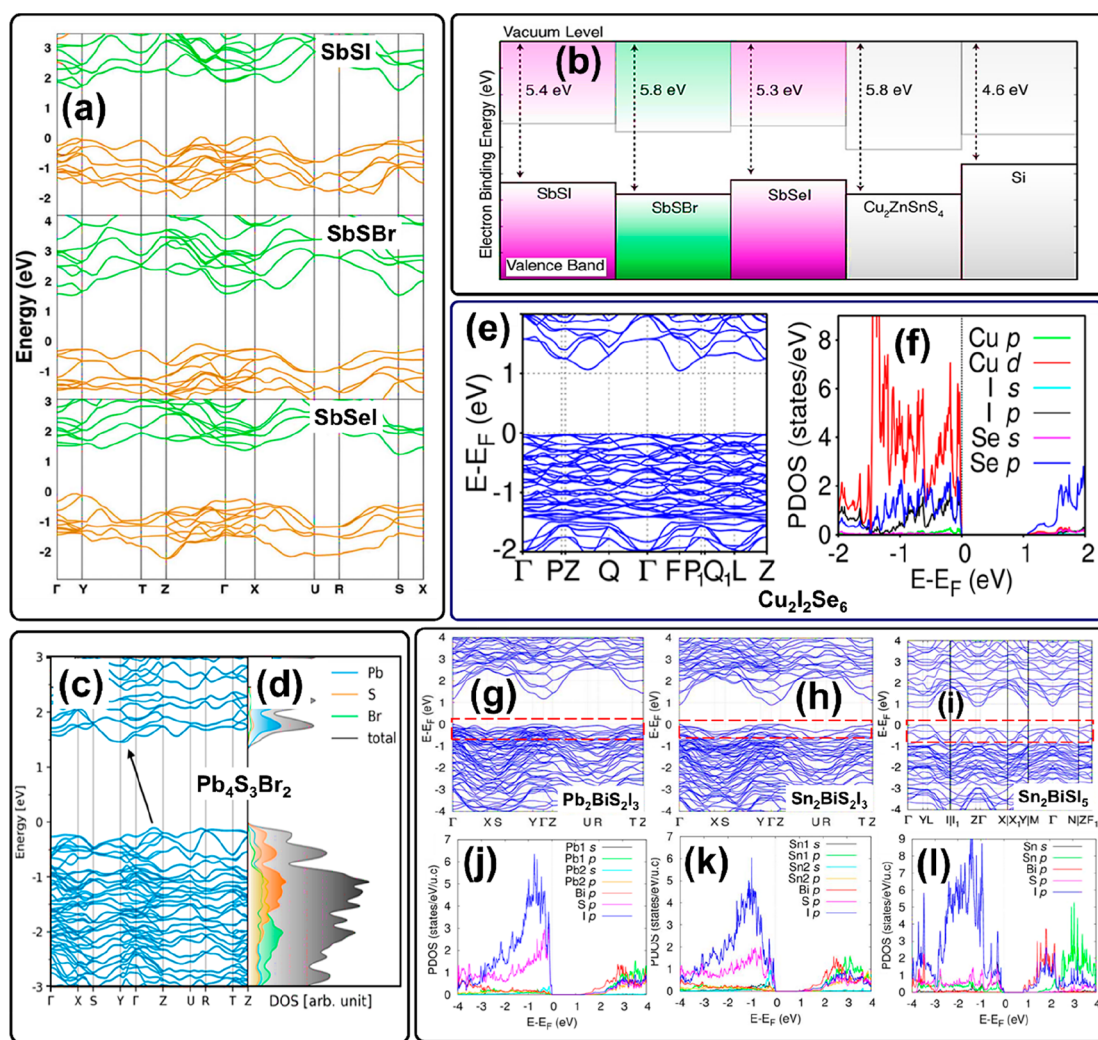
**Figure 10.** (a) Energy−momentum band structures of SbSI (upper panel), SbSBr (middle panel), SbSeI (lower panel); all calculated with GGA-DFT. VBs are colored gold and CBs are in green. The top of the VB is set to 0 eV. Reproduced with permission from ref 74. Copyright 2015 The Royal Society of Chemistry. (b) Comparison of predicated band energies of SbSI, SbSBr and SbSeI with CZTS and Si. Reproduced with permission from ref 197. Copyright 2016 American Institute of Physics. (c) Band structure and (d) DOS of $Pb_4S_3Br_2$. The band structure, calculated using PBE+SOC function, reveals an indirect bandgap, whereas the DOS exhibits that the VB and CB band-edge states are contributed by S and Pb, respectively, while Br-related states fall deeper in the VB. (c, d) Reproduced with permission from ref 112. Copyright 2020 American Chemical Society. (e) Electronic band structure and (f) pDOS of $Cu_2I_2Se_6$. The Fermi level (EF) is set to zero energy. (e, f) Reproduced with permission from ref 111. Copyright 2018 American Chemical Society. (g, h, i) Electronic band structure and (j, k, l) pDOS of $Pb_2BiS_2I_3$, $Sn_2BiS_2I_3$, $Sn_2BiSI_5$. The red highlighted parts in g−i represent the flat VB existed near the VBM. (g−l) Reproduced with permission from ref 109. Copyright 2016 American Chemical Society.

calculations of Sb-based chalcohalide using pseudopotential method, the DFT method allowed authors to use more extensive symmetry directions in a wider range to add more VB in the band structures of SbSeI. They found that the VBM and CBM are located at the Γ and S symmetry points of the Brillouin zone, respectively. Thus, the band gap of SbSeI is indirect with a value of ∼1.65 eV. Employing a similar approach, they also calculated the electronic band structures of SbSBr in para- and ferroelectric phases and found that the SbSBr exhibits an indirect forbidden gap of ∼2.16 and 2.21 eV in the para- and ferroelectric phases, respectively.

Most of the previous reports mainly focused on the electronic band structure and phase transitions, and no attention has been paid to the effective masses of these compounds despite their suitable band gap for energy applications. In this regard, Khan et al.[196] calculated the electronic band structures of SbSI, SbSeI, and SbSBr using ab initio calculations and also the effective masses of electrons and holes from the respective bands at the

top of the VB and the bottom of the CB. They found that the SbSI has a smaller effective mass of electrons ($0.07\ m_e$) and holes ($0.098\ m_h$) and great mobility than SbSeI and SbSBr that described the p-type nature of these chalcohalide materials. Walsh and co-workers also calculated the electronic band structure along with the effective masses of electrons and holes and IPs of SbSI, SbSBr, and SbSeI (Figure 10a).[197] The effectiveness of these Sb-based chalcohalides as an absorber layer was investigated by calculation of the electronic structure properties and by comparing the results of scalar-relativistic (GGA-DFT), HSE, and HSE-SOC. The electronic band structures of SbSI, SbSBr, and SbSeI showed indirect band gaps as displayed in Figure 10a. The upper VB in all cases is composed of chalcogen and halide p orbitals, while the lower CB made up of Sb 5p orbitals that are impacted by SOC. Although SbSI has an indirect gap with the top of the VBM lying close to the X point and the bottom of the CBM being at the S point, the difference between direct and indirect band gaps is 0.15 eV. The

substitution of I by Br, on the other hand, results in a change in the electronic band structure, with the VBM in between Z and Γ and the CBM at Γ. Similarly, replacing S with Se resulted in a significant shift, in which the VBM is between gamma and Y in the first Brillouin zone and the CBM is between Y and T. In SbSeI, the contribution of the chalcogen in upper VBM is increased, owing to the lower IP of Se (<S), which explains the band engineering effect and leads to a narrowing of the gap. The change in band extrema is caused by changes in local environment of Sb, which can be linked to the compositional dependency of the stereochemical activity of the Sb $5s^2$ lone pair electrons. Because of the closely matched lattice parameters and systematic band offsets, epitaxial growth of SbSBr on SbSI with aligned polarization can make great applicants for semiconductor heterojunctions. A similar group found that the effective masses of electrons and holes are all below 0.65 $m_e$ that can support high-mobility band transport. Further, the IPs for SbSI, SbSBr, and SbSeI were predicted as 5.37, 5.80, and 5.26 eV, respectively. The band energies of these materials were also compared with $Cu_2ZnSnS_4$ (CZTS) and Si materials for solar energy applications. As shown in Figure 10b, the position of band energies of SbSBr is like the CZTS and several other Cu-based absorbers ($CuInS_2$, $Cu_2S$), where the upper VB is composed of Cu 3$d$ states. Since the band edge positions are closely related to the nature of the halide ion, the band edge states are highly composed of the halide electronic states. Therefore, the VB of SbSBr is much deeper in energy than the iodide counterparts. Based on the comparison of the energy band positions and low electron affinities of SbSBr, SbSI, and SbSeI compounds, alternative suitable buffer materials such as ZnTe, $Cu_2O$, $Zn_2TiO_4$, $KTaO_3$, $AlTiO_3$, and $MgTiO_3$ for CdS are suggested. Mo would also be a suitable hole collecting contact for SbSBr as it has a similar VB energy to CZTS, whereas Ni and Au would match to SbSI and SbSeI because of their well-matched work functions.

## 4.2. Transition/Post-transition Metal Chalcohalides

### 4.2.1. Pb-Based Chalcohalides.

The DOS calculations of $Pb_4S_3Br_2$, $Pb_4S_3I_2$, and $Pb_3S_2Cl_2$ proved that the band-edge states mainly formed from the Pb and S states with negligible contribution from halide which mainly located deeper below the VB edge in all cases.[112] As an example, the band structure and DOS of $Pb_4S_3Br_2$ are shown in Figure 10c and d. The halide-dependent shift was observed in the band gap energies with indirect band gap values of 1.98, 1.76, and 2.0 eV for $Pb_4S_3Br_2$, $Pb_4S_3I_2$, and $Pb_3S_2Cl_2$, respectively. The optical properties in the materials are caused due to the localized Pb−S interactions due to the halides.[182] Therefore, the electronic band structures and DOS of the hypothetical $Pb_3Se_4$ and $Pb_3Br_4$ were calculated to understand the $Pb_3Se_2Br_2$, which revealed that the anions contribute to the VBM and fully occupied Pb 6$s$ orbitals located far below the VBM and Pb states contribute to the CBM. Unlike earlier reports, Ni et al.[182] found the lower band gap energy for $Pb_4S_3I_2$, where DFT calculations predicted the indirect band gap value of 1.5 eV.[184] They noted that VBM of $Pb_4S_3I_2$ is contributed by all Pb, S, and I, while major contribution was from S and CBM is dominated by Pb states. Thus, as explained in the crystal structural data (section 3.2), the Pb1 atom, which covers half of the Pb atoms in the crystal structure, has a higher DOS value than Pb2 and Pb3. In other words, the different chemical environments of Pb atoms contribute differently at the VBM and CBM, reflecting different DOS values. These unique

and important characteristics made the Pb-based material a promising candidate for energy-related applications.[161,198,199]

### 4.2.2. Cu-Based Chalcohalides.

Kanatzidis and co-workers are the first to report $Cu_2I_2Se_6$ as a new Cu-based chalcohalide semiconductor.[111] This material shows a wide indirect band gap of ∼1.95 eV, a low electron effective mass of 0.32 eV and high chemical stability, which comprehends from the energy-momentum band structures (Figure 10e,f). The calculated band structure revealed that the CBM is located at the F point and the VBM at the L point. The Cu 3$d$, Se 4$p$, and I 5$p$ orbitals mainly contribute to the VBs near the VBM with no dispersion, whereas the CB minimum consists of Se $p$ orbitals with significant dispersion that results in low electron effective masses. The pDOS further revealed that the CBM is mainly dominated by the Se $p$ states with some contribution from Cu $d$-Se $p$ hybridized orbitals. It also shows that the VBM is mainly contributed by the Cu $d$, Se $p$, and I $p$ orbitals, with the dominance of Cu $d$ contribution. Authors thus concluded that the VBM is formed by the sequence of localized and weak Cu $d$−Se $p$ and Cu $d$−I $p$ interactions, which are held responsible for the flat VBM bands and high hole effective masses. Thus, the weak and localized interactions between Cu $d$−Se $p$ and Cu $d$−I $p$ are responsible for the nearly flat character of the VBM and high hole effective masses. Also, the band structure calculations indicate an indirect band gap with the preferable electron transport along the crystallographic ab-plane, superior to that of amorphous Se, making the Cu-based chalcohalide type of curious material for the solar cell.

## 4.3. Mixed-Metals (Pb/Sn/Sb/Bi) Chalcohalides

Like Bi/$Sb_{III}$-VI−VII, the electronic band structure calculations of $Pb_2BiS_2I_3$, $Sn_2BiS_2I_3$, and $Sn_2BiSI_5$ materials revealed that the VB of these materials is dominated by the I$p$ orbital, whereas the CB is attributed mainly to a combination of Bi$p$ and I$p$ orbitals (Figure 10g−i).[109] Detailed observation further explained the differences in their band gaps. A flat VB existed near the VBM (highlighted in Figure 10g−i), in contrast to the dispersive CB near the CBM, which led to the small electron effective masses than the hole effective masses making these materials $n$-type. In the case of $Pb_2BiS_2I_3$, VBM builds from the hybridized S$p$ and I$p$ states with very few contributions from Pb and Bi states, whereas CBM is formed from the Bi$p$ hybridized with I$p$ and few contributions from S$p$ state. However, in the case of $Sn_2BiS_2I_3$, high energetic Sn 5$s$ states made a major contribution and force the VBM toward making the band gap value lower than that of $Pb_2BiS_2I_3$. In $Sn_2BiS_2I_3$, flat VBM and CBM formed from the hybridized Sn$s$, S$p$, and I$p$ states and Bi$p$ and I$p$ states and showed a larger band gap compared to the former states due to the major contribution of $BiI_6$ octahedra in the electronic structure. The physical properties of $Sn_2SbS_2I_3$ have recently been studied using ab initio approaches to understand the atomistic causes of exceptional PV performance by relating the local polarization (previously hidden to macroscopic diffraction techniques) to the high optoelectronic efficiency potential and defect-tolerant properties.[185] Electronic DOS revealed that CBM is generated via Sb$p$−I$p$ interactions, while the VBM is generated by antibonding interactions between the Sn $5s^2$ lone pair and both anion $p$ states. Following molecular dynamics (MD) simulation, the optical absorption spectrum showed a weak onset at the fundamental electronic band gap of 1.08 eV. A low electronic degeneracy at the band extrema (a consequence of the low crystal symmetry) and a weak transition dipole moment between the VBM and CBM electronic states (a
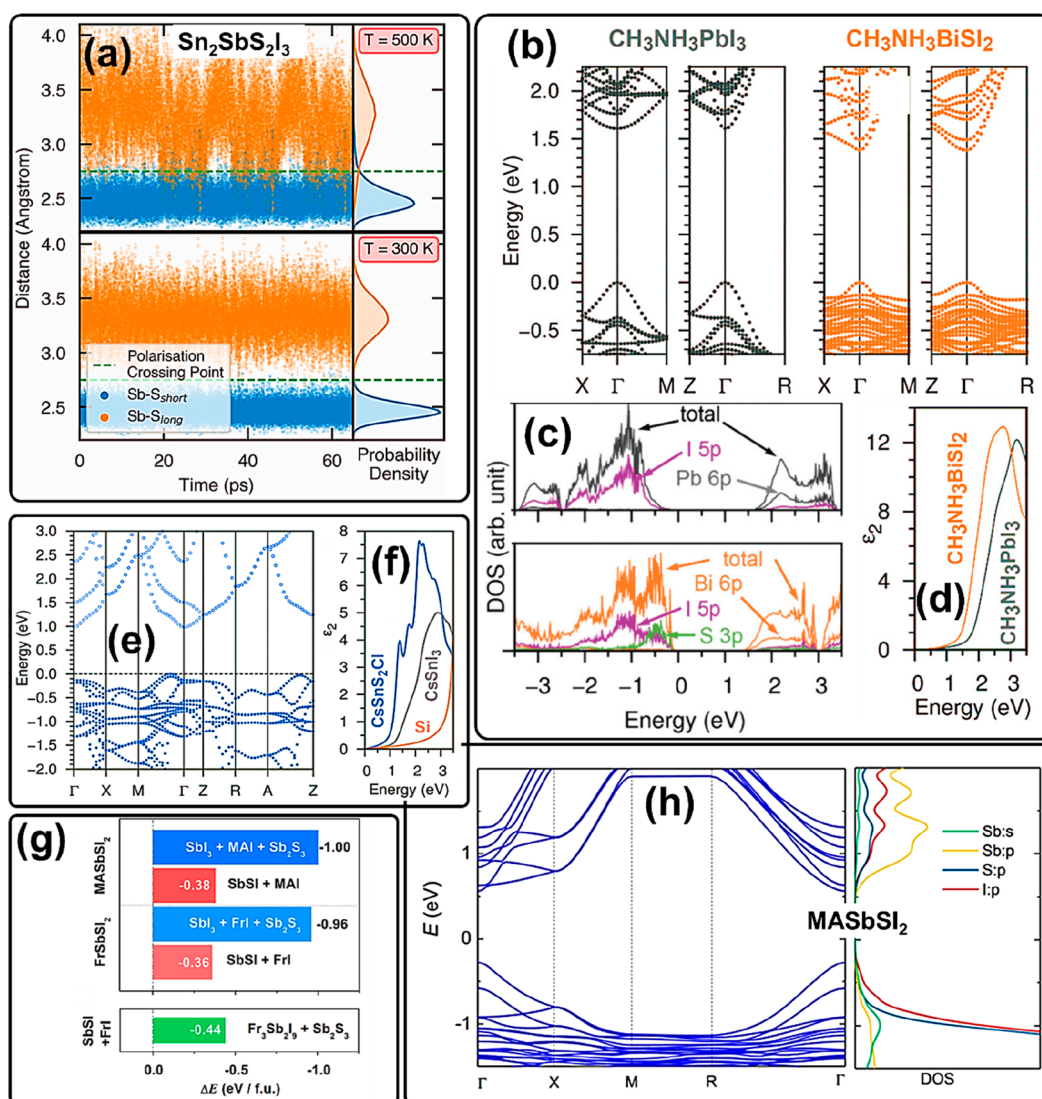
**Figure 11.** (a) Variation of Sb−S bond lengths in $Sn_2SbS_2I_3$ as a function of time during MD simulations. The probability densities are shown on the right given by $4\pi r^2 g(r)$, where $g(r)$ is the radial distribution function. Reproduced with permission from ref 185. Copyright 2021 The Royal Society of Chemistry. Comparison of (b) band structures, (c) DOS, and (d) imaginary part of dielectric function of $CH_3NH_3PbI_3$ and $CH_3NH_3BiSI_2$. The band structures were obtained using a supercell containing eight formula units of $CH_3NH_3PbI_3$ and $CH_3NH_3BiSI_2$. The k-points Γ, X, M, Z, and R have coordinates of (0, 0, 0), (0, 21, 0), (21, 21, 0), (0, 0, 21), and (21, 21, 21), respectively. The DOS of CBs in (c) for both $CH_3NH_3PbI_3$ (upper panel) and $CH_3NH_3BiSI_2$ (lower panel) is increased three times to clearly show the 6p states of Pb or Bi. (e) Band structure of $CsSnS_2Cl$ calculated using the HSE function and (f) imaginary part of dielectric function ($\varepsilon_2$) of $CsSnS_2Cl$, $CsSnI_3$, and Si, all of which have calculated band gaps at about 1.0−1.1 eV using the HSE functional. (b−f) Reproduced with permission from ref 73. Copyright 2016 The Royal Society of Chemistry. (g) Decomposition energies of different reaction pathways for proposed $MASbSI_2$ and $FrSbSI_2$ compounds and (h) band structure and DOS of the proposed $MASbSI_2$ using HSE06. (g, h) Reproduced with permission from ref 72. Copyright 2018 American Chemical Society.

consequence of both symmetry restrictions and low spatial overlap) were roots stated for the prior behavior. The even (gerade) parity of both the VBM and CBM wave functions about the crystal inversion center resulted in a formally symmetry-forbidden transition at the direct gap in the centrosymmetric *Cmcm* structure, while for the *Cmc2₁* ground-state polymorph, this symmetry selection rule was broken by a shift in Sb positions as well as spin−orbit splitting. Despite the fact that these effects have a modest impact on the electrical structure, i.e., $\Delta E_{gCmcm\ vsCmc21} = 0.03$ eV. Figure 11a depicts the persistence of polar distortions at RT, but also dynamic fluctuations at 500 K for Sb−S bonds in $Sn_2SbS_2I_3$ studied using MD simulation. For the RT MD runs within the simulation time scale, no appreciable swapping of the Sb−S bonds corresponding to lattice polarization switching is noted.

During the $T = 500$ K runs, however, transient hopping of Sb atoms occurs as the material approaches a phase transition to higher-symmetry *Cmcm*, at which point the Sb−S bonds become equivalent and the probability densities merge. The overall study predicted a large spontaneous polarization of 37 C cm$^{-2}$, which could be utilized for electron−hole separation in active solar cells, as well as an ideal electronic band gap of 1.08 eV with power-conversion efficiencies of $\eta_{max}$, >30% at the radiative limit for film thicknesses $t > 0.5\ \mu$m. From the perspective of PV applications, the bulk PV effect causes open-circuit voltages above the electronic band gap in such compounds, potentially allowing efficiencies greater than the standard limit for a single-junction solar cell.[185,200]

## 4.4. Hybrid Organic−Inorganic Metal Chalcohalides

In this context, Yan and co-workers first time assessed the viability of mixed halide-chalcogenide perovskites for PV applications through a combination of DFT calculations and solid-state reaction.[187] Theoretical calculations proposed that all of these $CsSbSX_2$, $CsSbS_2X$, $CsBiSX_2$, and $CsBiS_2X$ chalcohalide perovskites are thermodynamically unstable, despite having negative formation enthalpies and thus decomposing into binary and ternary secondary phases or forming nonperovskite phases. Solid-state-reaction attempts supported theoretical predications, as none of the reactions tested produced the desired perovskite phases. These findings suggest that the synthesis of these mixed-anion perovskites is challenging under thermal equilibrium conditions, but these materials could be formed as metastable phases under nonequilibrium conditions or by entropy stabilization. With all of this context and motivation, Sun et al.[73] first reported the chalcohalide perovskites materials based on the split-anion approach by replacing Pb with heterovalent atoms (Bi, Sn) to keep both the charge neutrality and the 3D perovskite structure. $CH_3NH_3BiSeI_2$ and $CH_3NH_3BiSI_2$ materials exhibited suitable direct band gaps (1.3 to 1.4 eV) and optical absorption over $CH_3NH_3PbI_3$, making fit for single-junction solar cells application. Both materials exhibited similar distributions of orbitals in the band structures like $CH_3NH_3PbI_3$ perovskite where VBM $MABiSI_2$ consisted of the antibonding states of Bi $6s$ and $I5p$/ $S3p$ orbitals and the CBM consisted mainly form the $Bi6p$ states (Figure 11b−d). The corresponding $m_e$ of 0.32 and $m_h$ of 0.40 $m_0$ were calculated for $CH_3NH_3BiSeI_2$ and $CH_3NH_3BiSI_2$, respectively, to compare with $MAPbI_3$ perovskite (0.19 and 0.25 $m_0$), suggesting good electron transport properties in these materials as like in $MAPbI_3$. The comparative study indicates that the 3D $MABiSI_2$ perovskites will be good candidates as absorbers for PV devices.

The inorganic mixed anion $CsSnS_2Cl$ perovskites have also shown promising optical absorption even higher than $CsSnI_3$ and have an indirect band gap of approximately 1 eV based on hybrid functional calculation. Figure 11e shows the corresponding band structure of $CsSnS_2Cl$ calculated using the HSE functional and the band gap of 0.98 eV. The CBM located at the Γ point and the VBM at about one-third distance from Γ to M and yielded an indirect band gap that agrees with the GW calculation within 0.01 eV. The imaginary part of the dielectric function ($ε2$) of $CsSnS_2Cl$, along with $CsSnI_3$ and Si for comparison is also shown in Figure 11f. It shows that $CsSnS_2Cl$ must have even greater optical absorption than the direct-gap $CsSnI_3$ below 3 eV and this is partly due to the relatively large DOS near the top of the VBs due to the presence of dual anions, similar to $CH_3NH_3BiSI_2$. There is still a large family of new materials that are based on the split-anion approach, which has been largely unexplored.[73] Therefore, the exploration of alternative synthetic methods that can stabilize chalcohalide perovskite by kinetic factors is necessary since all predictions are focused on theoretical calculations.[201] In contrast to all these reported works, Mitzi and co-workers carried out the combined experimental and computational validation and found no evidence of the formation of the $MASbSI_2$ phase, instead a mixture of the binary and ternary compounds ($Sb_2S_3$ and $MA_3Sb_2I_9$) took place.[72] The corresponding decomposition energies of different reaction pathways for proposed $MASbSI_2$ materials proved this hypothesis (Figure 11g) and only under the nonequilibrium condition can the metastable mixed chalcohalide phase be formed. This combined experimental

and computational study showed a contradiction to the former report of Nie et al.[186] Later, to understand the electronic properties of $MASbSI_2$, the authors calculated the band structure and DOS-based on the relaxed structure with HSE06 functional (Figure 11h). The band structure diagram shows a direct band gap of 0.83 eV significantly less than the reported 2 eV,[186] where the CBM formed mainly from Sb $p$ orbitals, whereas VBM formed from I and S $p$ orbitals. Relatively dispersive band edges in the vicinity of the Γ pointed good carrier mobilities. Therefore, the authors proposed that similar Pb-free mixed chalcohalide phases could still form under nonequilibrium conditions as metastable phases and could be stabilized in a 2D perovskite lattice referring to a potential candidate for PV applications due to the appropriate energy band gap and electronic characteristics. Very recently, Mao et al.[137] performed the first-principles calculations of the band gaps of 192 Pb-free mixed-anion perovskites materials and reported that the band gap increased with an increase in the electronegativity of the anions. They reported that the contribution of anions to the band-edge states is related to electron affinity and structure parameters, whereas cations mainly contributed to the CBM. These recent findings and relevant studies encourage the researchers to try out stable and efficient chalcohalide perovskite synthesis for future optoelectronic applications.

## 5. CHALCOHALIDE MATERIALS SYNTHESIS AND APPLICATIONS IN ENERGY DEVICES

Various synthetic methods have been applied for the synthesis of chalcohalide materials, e.g., growth from melt and vapor, self-flux, the Bridgman, chemical and physical vapor transport, sonochemical, microwave, colloidal, and solvo- and hydro-thermal methods, etc.[122−136] Initially the Bridgeman-Stockbarger melt growth and the vapor growth methods were commonly used by researchers. However, these methods often necessitated a relatively long time at high temperatures as well as several grinding and igniting stages. Because of the inefficiency of solid-state diffusion during the reaction, high temperatures and long durations are unavoidably required for the development of thermodynamically preferable phases. To overcome these limitations, researchers turned to solution-based crystal formation processes. In the next sections, we will review the synthesis of Bi- and Sb-based chalcohalides using different methods and their applications in energy devices such as solar cells, photocatalysis, photodetectors, batteries, supercapacitors, thermoelectrics, and piezo/pyro-electric nanogenerators. We will also briefly describe the development of some new Pb-, Sn-, Ag-, and organic−inorganic perovskites-based chalcohalides and their applications in energy devices.

### 5.1. Synthesis of Heavy Pnictogen Chalcohalides

**5.1.1. Bi-Based Chalcohalides.** Among the various methods reported earlier, the most of techniques normally require complicated equipment with high growth temperature (>600 °C) and control over the temperature gradient, making the process complex and low throughput. The first synthesis of Bi-based sulfoiodide crystals was carried out by wet method and vapor phase growth by the flux method.[213−216] However, the property-based analysis remained unresolved owing to very early work in 1950. Later, in 1960, Nitsche and Merz studied the photoconductivity in BiSI material for the first time, quantifying photoelectric response and revealing maximum photoresponse at ~785 nm.[217] The Bridgeman−Stockbarger technique was then applied to synthesize orthorhombic BiSI crystals in a quartz

**Table 2. Summarized Reports on the Synthesis and Properties of Bi-Based Chalcohalide Materials**

| material | synthesis | reaction conditions | crystal structure | morphology | bandgap (eV) |
|---|---|---|---|---|---|
| BiSI[202] | Bridgeman–Stockbarger | Bi, S, and I powders; 430 °C | orthorhombic | needle-like crystals (4–12 mm) | |
| BiSI[203] | Bridgeman–Stockbarger | $Bi_2S_3$ and $BiI_3$ powders; 450 oC for 100 h | | needle-shaped single crystals | 1.3 |
| BiSI[204] | gel | $BiCl_3$, $Bi_2O_3$, $BiI_3$, thiourea, $H_2S$, KI and HI; RT for 7 days | | single crystals (5 mm) | |
| BiSeI[205] | vapor sublimation | Bi, Se, and I powders; 560 °C for 4 days | | needle-shaped crystals (7 mm); platelets (20 × 10 × 6 mm³) | |
| BiSI[206] | vertical Bridgeman method | High purity Bi, S, and I powders (99.9999%) | orthorhombic | single crystals (50 mm in length and 10 mm in diameter) | 1.59 |
| BiSeI[206] | | High purity Bi, Se, and I powders (99.9999%) | | | 1.28 |
| BiSCl[207] | solvothermal | $BiCl_3$ + S; 180 °C for 5 days | orthorhombic | polygonal tubular (13–18) × (17–21) $\mu m^2$ | |
| $Bi_{19}S_{27}Br_3$[207] | | $BiCl_3$ + Thiourea + NaBr; 180 °C for 1 day | hexagonal | bundle-rodlike (2–8) × (6–20) $\mu m^2$ | |
| BiSI[207] | | $BiCl_3$ + Tu + NaI; 180 °C for 1 day | orthorhombic | bundle-rodlike; (5–10) × (20–70) $\mu m^2$ | |
| BiSI[208] | hydrothermal | $BiCl_3$ + Thiourea + $I_2$ in distilled water 160 °C for 30 h | orthorhombic | bundle-rodlike 0.1 to 2 $\mu m$ in diameter | 1.8 |
| BiSI[209] | ultrasonic spray pyrolysis | A mixed solution $BiCl_3$ + Thiourea in Water and $I_2$ in ethanol; 320 °C for 15 min | orthorhombic | rod-like particles 2 $\mu m$ in length and 100–200 nm in diameter | |
| BiSI[210] | solvothermal | $Bi(NO_3)_3$ + thiourea + $I_2$ in ethanol 160 °C for 30 h | orthorhombic | nanowires | |
| BiSeI[211] | solvothermal | $Bi_2Se_3$ + $BiI_3$ in ethanol or $BiCl_3$ + Se + NaI in ethanol 200 °C for 12 h | orthorhombic | rod-like monocrystals | |
| BiSX (X=I, Br, Cl)[212] | hot-injection | $Bi(Ac)_3$ + $(Me_3Si)_2S)$ + BzX (X = I, Br, Cl) + Oleic acid + Octadecene; 180-250 °C for 15 – 180 min | orthorhombic (BiSI, BiSBr) and novel polymorph (BiSCl) | ribbon-like nanocrystals 170 nm in length and 20 nm in width | 1.5 (indirect), 1.6 (direct) (BiSI) 1.95 (indirect), 2.25 (direct) (BiSBr), 2.05 (indirect), 2.55 (direct) (BiSCl) |

ampule at 430 °C in a furnace with a temperature gradient of 60 °C, using Bi, S, and $I_2$ powders.[202] The as-synthesized BiSI crystals showed the needle-like structure of ~4–12 mm, n-type conductivity, and higher resistivity of ~$10^8$–$10^9$ Ω cm. The anisotropy in the PV effect was stated by measuring the spectral distribution of internal photoconductivity for different BiSI crystals. Similarly, temperature dependence dark conductivity, photoconductivity, and relative spectral sensitivity for ferro-electric BiSI with Curie temperature of −160 °C were reported in that era.[203] An electron drift mobility of 1 cm$^2$/s V along the c-axis was specified for BiSI single crystals. After 1885, the research transitioned toward solution-based techniques. The BiSI crystals were grown at room temperature using the gel technique and the growth conditions of the crystals as well as the effect of reactant concentration, gel density, and the introduction of the neutral gel were investigated.[204] The single and needle-like BiSI crystals of sizes ~5 and ~7 mm, respectively, were produced. One of the important attributes of chalcohalides is their dielectric proper-ties. Ganesha et al.[205] have briefly described the effect of temperature and frequency on the dielectric properties of the BiSeI, where measurements were carried out perpendicular to the cleavage of (110) plane. In addition, the first optical properties of the BiSI material were studied for their applications in optical memories, optical switches, etc., but systematic evaluations remained vague.[188,206] Afterward, Zhu et al.[218] further demonstrated the synthesis of hollow crystals of BiSCl and bundle-rodlike crystals of $Bi_{19}S_{27}Br_3$ and BiSI, using solvothermal synthesis in ethanol at 180 °C. Here authors least explained the mechanism behind the formation of orthorhombic BiSCl, BiSI, and hexagonal $Bi_{19}S_{27}Br_3$ crystals. BiSCl formed from the reaction between Bi (formed after reduction of BiO$^+$ (BiOCl) from ethanol) and atomic S to $Bi_2S_3$ and then to BiSCl gradually in 5 days, whereas $Bi_{19}S_{27}Br_3$ and BiSI formed by reaction between (Bithiourea)$^{3+}$ with $BiBr_3$ and $BiI_3$, respectively. The BiSI crystals were also synthesized hydrothermally from the reaction between stoichiometric $BiCl_3$, thiourea, and $I_2$ at 160 °C for 30 h.[208] The BiSI crystals showed the orthorhombic phase (space group *Pnma*) with a band gap of 1.8 eV. Yet, no detailed studies or material properties have been noted. In between, high-pressure synthesis polycrystalline BiSI films with rod-like crystals were synthesized on glass substrates at 320 °C using an asynchronous ultrasonic spray pyrolysis method.[209] Nonetheless, the development of these materials via the solvothermal method was not reported until the first attempt in 2011 by Cao et al.[210] to synthesize crystalline BiSI particles using a solvothermal method at 160 °C for 30 h. Although the reaction was performed at a lower temperature, it involved both longer reaction times and conditions of high pressure. To avoid these excessive reaction conditions, low temperature and mild solution approach was testified by Zhu et al.[211] for the formation of orthorhombic BiSeI rods from the $BiCl_3$, Se and NaI, or $Bi_2Se_3$ and $BiI_3$ in ethanol at 200 °C for 12 h. However, thorough research on understanding of reaction mechanism has never been carried out to date. Furthermore, the optical band gap of 1.56 eV was estimated by using reflectance ellipsometry.[219] The synthesis of orthorhombic BiSI and $Bi_{19}S_{27}I_3$ NCs was further reported by a one-step solid-state mechanochemical method avoiding the use of aqueous solutions and heat treatment. The as-synthesized BiSI and $Bi_{19}S_{27}I_3$ NCs showed band gaps of 1.80 and 1.14 eV, respectively.[220] UPS study revealed that the $E_{VB}$ and $E_{CB}$ of BiSI were 1.959 and 0.681 eV (vs NHE), respectively, while those of $Bi_{19}S_{27}I_3$ were 1.423 and 0.777 eV (vs NHE), respectively. Unexpectedly, mechanochemically synthesized

BiSI and $Bi_{19}S_{27}I_3$ NCs showed PL spectra with a similar emission band ranging from 425 to 500 nm. It is seen that both materials show a similar emission band ranging from 425 to 500 nm with weaker emission band intensity of $Bi_{19}S_{27}I_3$ than BiSI. Later, growth of large-sized strip-like BiSeI crystals was carried out using the physical vapor transport (PVT) method with self-synthesized BiSeI polycrystals.[105] Centimeter-sized BiSeI crystal showed the n-type conductivity with a bandgap of 1.29 eV and carrier concentration of $2.1 \times 10^{16}$ cm$^{-3}$ and Hall mobility of ~238 cm$^2$ V$^{-1}$ s$^{-1}$. Until recently, most of the above mentioned reports on Bi-based chalcohalides are mainly aimed at synthesis methods and their basic physiochemical characterizations. Table 2 summarizes the progress in the synthesis of these Bi-based chalcohalide materials along with their reported structural, morphological, electrical, and optical properties.

**5.1.2. Sb-Based Chalcohalides.** The synthesis of Sb-VI–VII (where VI = S, Se, Te; VII = Cl, Br, I) materials has been demonstrated in the 18th century and their structure was further revealed by E. Donges in 1950 as the rhombic-bipyramidal using X-ray diffraction.[213,216] SbSI is the first material discovered to be ferroelectric as well as photoconductive in the family of chalcohalide materials. The photoelectric properties of SbSI were investigated by Nitsche and Mertz,[70] whereas the ferroelectricity was first revealed by Fatuzzo et al.[71] by measuring the dielectric constant-temperature dependence in 1962. The discovery of ferroelectricity in SbSI was a significant breakthrough that piqued the interest of researchers to further explore this family of materials. Harbeke[65] and Fridkin et al.[69] investigated the intrinsic absorption in SbSI and found that the ferroelectric phase transition in SbSI occurred as a result of a jump of the intrinsic absorption edge of ~0.06 eV, and by a change in the temperature dependence coefficient of the forbidden bandwidth. Fridkin et al.[64] further found that the SbSBr, like SbSI, exhibited semiconducting ferroelectric proper-ties, whereas SbSCl and SbSeCl compounds were nonferro-electric.[221] An interesting finding was further reported by Audzijonis et al.[222] where they found that the SbSI and SbSeI exist in various phases depending on temperatures, such as ferroelectric (T < 295 K, SbSI), antiferroelectric (T < 410 K, SbSI and SbSeI), and paraelectric (T > 410 K, SbSI and SbSeI). This behavior can be linked to the ns$^2$ lone pair electrons associated with Sb(III). The conductivity of these materials was reported to be in the range from $10^{-7}$ to $10^{-10}$ Ω$^{-1}$ cm$^{-1}$ depending upon the composition and phase.[67]

Although, the first synthesis of Sb-based chalcohalide materials dates back to the 18th century, tremendous studies on the different synthesis processes and structural, optical, and electrical characterizations have been conducted thereafter. However, actual applications of this exciting class of materials in energy devices have been less explored to date. The ferroelectric transition in these materials, which results in one phase with spontaneous polarization, indicates that these materials can be an ideal candidate for exhibiting bulk and poly crystalline photoferroic effects.[223] However, this class of materials has been mostly overlooked as promising candidates for their applications in energy devices. In recent years, tremendous progress and exciting outcomes on these materials by applying advanced theoretical calculations (discussed in sections 2 and 3) have revealed these materials as promising candidates in energy devices in a recent renaissance.

## 5.2. Applications of Heavy Pnictogen Chalcohalides

Chalcohalide materials with tunable compositions and favorable optical and electrical properties, as well as their ease of processing, open up a new avenue for their applications in various energy devices. The applications of these chalcohalide materials in various energy devices, such as solar cells, photocatalysis, photodetectors, batteries, supercapacitors, thermoelectrics, and piezo/pyro-electric nanogenerators, are discussed in this section with the aim of encouraging potential new applications. Tables 3 and 4 summarize the performance of these chalcohalide materials for above-mentioned applications.

**5.2.1. Solar Cells.** The idea of this timely review on chalcohalide compounds for energy device applications is induced by the tremendous and rapid progress in perovskite solar cells with an unprecedented device efficiency of over 25% in a short period.[28] As aforementioned, these chalcohalides have emerged as urge to find an alternatives to Pb-based halide perovskites solar cells. These chalcohalides, containing mixed chalcogen and halogens, exhibit $ns^2$ electronic configuration same as Pb-halide perovskites, and are thus predicted to produce efficient solar cells with high stability. Theoretical predications have quickly led their implementation in solar cells and have already demonstrated efficiencies up to 4−5%. In this section, the advances made in solar cells based on these chalcohalide materials are discussed.

*5.2.1.1. Bi-Based Chalcohalides.* Mullins and co-workers were the first to demonstrate the potential of Bi-based chalcohalide materials in photoelectrochemical (PEC) cells after extensive efforts in investigating different synthesis methods and fundamental properties. In 2012, the first PEC performances of n-type BiSI and BiSSeI micro rods synthesized using spray pyrolysis technique were reported.[106,224] These spray-pyrolysis synthesized BiSI thin films showed the indirect and direct band gaps of 1.57 and 1.63 eV, respectively. Initial PEC testing of BiSI films in NaI/acetonitrile showed photocurrent density up to 5 mA/cm² with a maximum $V_{oc}$ of 0.37 V with an $I/I_3$ couple under AM 1.5 G illumination and EQE of 25 to 40% across the visible range (Figure 12a).[224] Detailed analysis further revealed that BiSI absorbers had the mean hole diffusion length of $\sim 5 \times 10^{-6}$ cm ($\sim 50$ nm), which is lower than the most common solar cell absorber materials.[224] This lower value is most likely due to the polycrystalline nature and the high defect concentration in the BiSI absorbers. Because the effective screening of the electric field at the heterojunction may also prevents electron and hole separation leading to the recombination in the neutral bulk region. Therefore, the authors tuned the optical properties and performances of BISI absorbers by incorporating Se.[106] The optical band gaps were tuned from 1.63 eV (BiSI) to 1.48 eV (BiS$_{1-x}$Se$_x$I, $x = 0.6$). The EQE spectra in Figure 12b confirms that the Se incorporation led to the improved conversion of NIR photons, correlating with the optical band gap values. However, the incorporation of Se did not improve the conversion of UV and visible photons (Figure 12b) as well as the PEC performance of BiS$_{1-x}$Se$_x$I absorbers compared to its BiSI counterpart (a PCE of 0.25%). This was attributed to an enhanced rate of recombination, which could have been induced by the inclusion of defects following Se incorporation. Immediately after, a first working solid-state heterojunction device based on *n*-type BiSI absorber and *p*-type CuSCN window layer was demonstrated.[106] However, due to charge recombination in the BiSI layer and light scattering by the CuSCN layer, the device had a very low efficiency of 0.01%. The low performance was also related to the poor electronic band alignment of the absorber with the hole and electron contact materials, which limited $V_{oc}$. Nevertheless, this first attempt at fabricating solid-state solar cell devices further promised the potential of BiSI as a light absorber in solar cells.

Kunioku et al.[76] reported the synthesis of orthorhombic BiSI and BiSeI powders from BiOI, and BiSeBr$_{1-x}$I$_x$ from BiOBr$_{1-x}$I$_x$ by a low-temperature treatment (<150 °C) and within a short time (<1 h) under H$_2$S and H$_2$Se gas, respectively. Surprisingly, the synthesis carried out at high temperature (>200 °C) resulted in the formation of Bi$_{12.7}$S$_{18}$I$_2$ impurities in BiSI due to the volatilization of I$_2$. The absorption edge of BiSI was significantly shifted from ∼ 630 to 780 nm with a successful phase transition from BiOI to BiSI. A similar trend was observed in BiSeI, however, BiSeI exhibited longer absorption (>900 nm) compared to that of the BiSI. The indirect band gap of BiSeBr$_{1-x}$I$_x$ was continuously tailored in between 1.71 to 1.51 eV by controlling Br/I ratio, which significantly contribute to VB formation. To check the validity of the synthesized BiSI as absorber materials in PEC device, comparative $J-V$ measurements of BiSI electrode prepared from BiSI NCs and electrophoretic deposited BiOI/FTO under H$_2$S/Ar atmosphere was investigated. The BiSI-based PEC device exhibited the highest current at all potentials as a result of the decreased resistance and/or increased number of absorbed photons by densely packed particles. The IPCE spectra as shown in Figure 12c showed an IPCE of 64% at 700 nm at 0.2 V vs Ag/AgCl, which is significantly higher than the reported value by Mullins and co-workers for the BiSI photoelectrodes (e.g., ∼38% at 500 nm at 0.4 V vs Ag/AgCl) under similar conditions.[76] This work demonstrated the effective film preparation method that can be used to achieve high photocurrent density for BiSI films. Inspired by this work, a two-step solution process was demonstrated to fabricate orthorhombic BiSI films using thiolamine solution (step I) and then BiI$_3$ (step II) deposition at a low temperature of 200 °C.[225] As deposited BiSI film showed the formation of nanorods (60−100 nm in diameter) on TiO$_2$-blocking layer (BL) coated FTO substrates, rather than a continuous film. The electronic structure of *n*-type BiSI semiconductor film was studied from UPS, which showed $E_F$ of 4.5 eV, $E_V$ of 5.9 eV, and $E_C$ of 4.3 eV (Figure 12d). The fabricated PV device using TiO$_2$-BL as electron transport layer (ETL) and P$_3$HT as hole-transporting material (HMT) did not work properly, which was attributed to poor electron transfer from BiSI to TiO$_2$ and mismatched band alignment with HTM (Figure 12d). It was concluded that materials engineering via doping/alloying to tune the electronic structure of BiSI or the use of alternative ETL and HTM can further improve the efficiency of BiSI solar cells.[225]

One of the key challenges in fabricating high-efficiency BiSI solar cells is the formation of secondary phases during the multistep synthesis process. In this regard, Tiwari et al.[190] demonstrated an interesting single-precursor solution (thermolysis) approach for the deposition of phase pure, paraelectric BiSI thin films. The film composed of flake-shaped grains stacked in highly compact manner over lengths of several micrometers. A band gap of 1.57 eV estimated from absorption and PL spectra was found to be in close agreement with the theoretical calculation. Based on the detailed thermodynamic analysis, calculated IP values, and band structures, a PV device with the architecture of glass/FTO/SnO$_2$/BiSI/F8/Au was fabricated that showed the record power conversion efficiency (PCE) of 1.32% with $J_{sc}$ of 8.44 mA/cm², $V_{oc}$ of 0.445 V, and FF of 35.14% under standard AM 1.5G illumination (Figure 12e). Probing

**Table 3. Summarized Reports of Bi-Based Chalcohalide Materials in Different Energy Device Applications**

| application | material | deposition | reaction conditions | band gap (eV) | device structure / measurement conditions | performance |
|---|---|---|---|---|---|---|
| solar cells | BiSI[224] | spray pyrolysis | $Bi(NO_3)_3$ + $NH_4I$ + thiourea in ethylene glycol; sprayed at 275 °C | 1.57 (indirect) and 1.63 (direct) | FTO/n-BiSI in NaI + acetonitrile electrolyte | $J_{sc}$ = 5 mA/cm² at 0.4 vs Ag/AgCl; onset potential = −0.25 V vs Ag/AgCl; IPCE = ~38% at 500 nm at + 0.4 V vs Ag/AgCl |
| | $BiS_{1-x}Se_xI$[106] | | $Bi(NO_3)_3$ + $NH_4I$ + thiourea in ethylene glycol and $SeO_2$+ ethanol; sprayed at 275 °C | 1.63 ($x = 0$) direct, 1.48 ($x = 0.4$) direct | FTO/n-BiSI/p-CuSCN | $J_{sc}$ = 2.5 mA/cm²; $V_{oc}$ = 0.25–0.38 V; PCE = 0.25% |
| | BiSI[76] | electrophoretic | Annealing BiOI/FTO at 150 °C for 10 min. under 5% $H_2S$/Ar atm | 1.58 | FTO/BiSI in NaI + acetonitrile electrolyte | $J_{sc}$: ~3.2 mA/cm²; IPCE: 64% at 700 nm at + 0.2 V vs Ag/AgCl |
| | BiSI[225] | two-step spin coating | Step 1 $Bi_2S_3$; $Bi_2O_3$ + Thiourea in 2-mercaptoethanol: ethanolamine (1:4 v/v); drying at 200 °C for 5 min; Step 2 BISI: $BiI_3$ + N-methyl-2-pyrrolidinone (NMP) coated solution on $Bi_2S_3$; annealing at 200 °C for 30 min. in a glovebox | 1.61 | FTO/TiO$_2$/BiSI/P3HT/Au | $J_{sc}$ = 0.1 mA/cm²; $V_{oc}$ = 0.4 mV |
| | BiSI[190] | spin coating | $Bi(NO_3)_3$ + thiourea + $NH_4I$ in 2-methoxyethanol: acetylacetone (4:1 v/v); heating at 200 °C in the air for 5 min. | 1.57 (direct) | FTO/SnO$_2$/BiSI/ F8/Au | $J_{sc}$ = 8.44 mA/cm²; $V_{oc}$ = 0.445 V; FF = 35.14%; PCE = 1.32% |
| | $Bi_{13}S_{18}I_2$[181] | solvothermal | $BiI_3$ + methylammonium iodide + thiourea in ethylene glycol; 195 °C for 12 h | 0.75 (indirect) | Photoanode: FTO/TiO$_2$/Bi$_{13}$S$_{18}$I$_2$ and Counter electrode: FTO/Pt; Electrolyte: LiI + I$_2$ + BMII + TBP + GT + acetonitrile:valeronitrile (85:15 v/v) | $J_{sc}$ = 3.82 mA/cm²; $V_{oc}$ = 0.58 V; FF = 38.3%; PCE = 0.85% |
| photocatalysis | $Bi_{19}S_{27}Br_3$[226] | microwave-assisted aqueous process | $Bi(NO_3)_3$ + thiourea + CTAB in distilled water:HNO$_3$ (10:1 v/v); 80 °C for 30 min | 1.42 | Reagent: RhB; Incident light: $\lambda \geq 420$ nm | degradation rate = 95% after 70 min visible light irradiation |
| | $Bi_{19}Br_3S_{27}$[227] | solvothermal | $Bi(NO_3)_3$ + thiourea + CTAB in ethanol: glycerol (3:1 v/v); 130 °C for 6 h | 1.49 | Reagent: 2,4-dichlorophenol; Light source: Xenon Lamp (150 W); Incident light: $\lambda \geq 420$ nm | degradation rate = 85.6% after 10 h reaction of the visible light irradiation; TOC removal efficiency: 76.2% after 3 h visible light irradiation; stability: 3% decay after 5 cycles |
| | $Bi_{19}Cl_3S_{27}$[228] | solvothermal | $BiCl_3$ + thiourea in ethanol; 180 °C for 72 h | 1.6 | Reagent: RhB and Cr(VI) solution; Light source: Xenon Lamp (350 W); Incident light: 420 nm | degradation rate for RhB = 95% after 30 min. the reaction of the visible light irradiation; stability = negligible decay after 4 cycles |
| | $Bi_{19}S_{27}Cl_3$[229] | solvothermal | $BiCl_3$ + thiourea in ethanol; 180 °C for 72 h | 1.6 | Catalysts = MoS$_2$/ Bi$_{19}$S$_{27}$Cl$_3$; Sacrificial reagents: 30 mM Na$_2$SO$_3$ + 10 mM Na$_2$S; Light source: Xenon Lamp (350 W) | H$_2$ evolution rate = 876.6 $\mu$mol g$^{-1}$ h$^{-1}$ |
| | BiSI[108] | solvothermal | $Bi(NO_3)_3$ + thioacetamide + NaI in acetic acid; 180 °C for 10 h | 1.6 | Catalysts: BiSI/MoS$_2$/CdS Sacrificial reagents: 0.2 m L$^{-1}$ Na$_2$SO$_4$ + 10% vol. 2-hydroxypropaonic acid; Light source: Xenon Lamp (300 W) | H$_2$ evolution rate = 21 mmol g$^{-1}$ h$^{-1}$ |
| | $Bi_{19}X_3S_{27}$ ($X = Cl$, Br)[230] | solvothermal | $BiCl_3$/BiBr$_3$ + thiourea in ethanol; 120–220 °C for 72 h | 1.32 (Bi$_{19}$Br$_3$S$_{27}$) | Catalysts: Bi$_{19}$X$_3$S$_{27}$ ($X$ = Cl, Br); Sacrificial reagents: 30 mM Na$_2$SO$_3$ + 10 mM Na$_2$S; Light source: Xenon Lamp (350 W) | H$_2$ evolution rate = 195.1 $\mu$mol g$^{-1}$ h$^{-1}$ (Bi$_{19}$Cl$_3$S$_{27}$) and 466.7 $\mu$mol g$^{-1}$ h$^{-1}$ (Bi$_{19}$Br$_3$S$_{27}$) |

**Table 3. continued**

| application | material | deposition | reaction conditions | band gap (eV) | device structure /measurement conditions | performance |
|---|---|---|---|---|---|---|
| photodetector | $Bi_{19}S_{27}(Br_{3-x}I_x)$[174] | hot injection | TMS in ODE and Al(acac)$_3$ + BiBr$_3$ in OA + OLA + ODE; 180 °C for 30 min | 0.81 ($Bi_{19}S_{27}Br_3$) | p$^+$-Si/SiO$_2$/Au/Bi$_{19}$S$_{27}$Br$_3$ | I$_p$@V$_{Bias}$ = ~140 nA at +5 V, 60 mW cm$^{-2}$ |
| | $Bi_{19}S_{27}I_3$[175] | solvothermal | Bi(NO$_3$)$_3$ + mercaptosuccinic acid + I$_2$ in ethylene glycol + EDRA-2Na in distilled water; 180 °C for 20 h | 0.83 (direct) | Si/SiO$_2$/Bi$_{19}$S$_{27}$I$_3$/Ag | I$_p$@V$_{Bias}$ = ~3.5 $\mu$A at +10 V and 900 nm, 150 W xenon lamp |
| | BiSI[231] | two-step process: spin coating and post-thermal annealing | BiI$_3$ + THF - spin-coated on FTO, hydrolyzed in a 1:1 methanol:water + annealed in an H$_2$S atm at 150 °C for 4 h | 1.57 (indirect); 1.63 (direct) | Si/SiO$_2$/BiSI/Au | I$_p$@V$_{Bias}$ = ~11 $\mu$A at +10 V, 70 mW cm$^{-2}$; responsivity = 62.1 mA W$^{-1}$; detectivity = 2.0 × 10$^{13}$ Jones |

into the possible origin of efficiency losses by RT time-resolved PL (Figure 12f) further revealed the short carrier lifetime of ~1 ns and the presence of bulk recombination centers associated with the Bi$_s$ and V$_s$ (sulfur vacancy) point defects.[190] This record device efficiency for BiSI solar cells later sparked an interest in the research community to realize the potential of Bi-based derivatives as a counter electrode in DSSCs and as an electron acceptor in halide perovskite solar cells. In this regard, Wu et al.[192] simulated the adsorption and desorption behavior of iodine species in Bi$_{19}$S$_{27}$Br$_3$ nanowires (NWs) to demonstrate their potential as CE in DSSCs followed by their initial attempts on the colloidal synthesis. Interestingly, NWs were found to exhibit reversible adsorption behavior of iodine species, showing their electrocatalytic activity toward the iodine reduction reaction (IRR) in DSSCs. The adsorption (1.98 eV) and desorption (1.97 eV) of the I atoms on Bi−S−Br were more spontaneous and reversible than those on the surface of Pt. Inspired by this, DSSC devices based on Bi$_{19}$S$_{27}$Br$_3$, and Bi$_{19}$S$_{27}$I$_3$ NWs yielded PCEs of 8.72 and 8.71%, respectively (Figure 12g), validating of multifunctionality of Bi-based chalcohalide materials. Recently, Yoo et al.[104] demonstrated that the in situ formed BiSI layer at the interface of the ETL and BiI$_3$ absorber layer, acts as an electron acceptor to further improve the rate of photoinduced charge separation and extraction of electrons in BiI$_3$ solar cells. An innovative and interesting approach of annealing of In$_2$S$_3$/BiI$_3$ structure at 200 °C was used for in situ formation of BiSI at the interface, however, the underlying mechanism and the role of In$_2$S$_3$ for in situ formation of BiSI remained unexplored. A device was fabricated with the architecture of the ITO/SnO$_2$/BiSI/BiI$_3$/spiro-OMeTAD/Au that showed a PCE of 1.21% with J$_{sc}$ of 12.6 mA/cm$^2$, V$_{oc}$ of 0.33 V and FF of 29%. Transient absorption studies were further carried out to propose the charge separation/transfer mechanism in the SnO$_2$/BiSI/BiI$_3$/spiro-OMeTAD, which is shown in Figure 12h. It was proposed that the presence of BiSI allowed a rapid transfer of photogenerated electrons in BiI$_3$, intercepting the photogenerated electron in the BiI$_3$ before they decayed back to the ground state and thus improving the rate of hole transfer from the BiI$_3$ to spiro-OMeTAD. Most of the above reports showed the growth of Bi-based chalcohalides directly on conductive substrates, which often resulted in poor control over the microstructure, which has a significant impact on device performance. To overcome these issues, colloidal synthesis of BiSX (X = I, Br, Cl) NCs using hot-coinjection approach has been introduced recently.[212] By coinjecting both the chalcogen (S) and the halogen (X = I, Br, Cl) precursors to the solution of bicarboxylate complexes in a noncoordinating solvent, a compositionally tunable BiSX NCs with high absorption coefficients and indirect band gaps (~1.5 to 2.05 eV) was synthesized. The photoelectrodes fabricated using these BiSX NCs-based ink showed quantum efficiency above 10% across the entire visible light spectrum. Although few attempts have been made on the demonstration of working devices based on BiSI as an absorber or as electron acceptor, and a single attempt on the use of Bi$_{19}$S$_{27}$Br$_3$ and Bi$_{19}$S$_{27}$I$_3$ as CEs in DSSCs, no attempts have been made to fabricate devices based on other derivatives of Bi-based chalcohalide materials until recently. Li et al.[181] reported a facile solvothermal process for the synthesis of Bi$_{13}$S$_{18}$I$_2$ nanorod film on a porous TiO$_2$ film using a mixture of BiI$_3$, thiourea, and methylammonium iodide in ethylene glycol at 195 °C for 12 h. The S/Bi ratio was found to have a profound effect on the phase formation, where a low S/Bi mole ratio formed the BiSI, and a high S/Bi ratio led to the formation of

**Table 4. Summarized Reports of Sb-Based Chalcohalide Materials in Different Energy Device Applications**

| application | material | deposition | reaction conditions | band gap (eV) | device structure /measurement conditions | performance |
|---|---|---|---|---|---|---|
| photodetector | SbSI[259] | hydrothermal | SbCl$_3$ + thiourea + NH$_4$I in aqueous HCl: 160 °C for 4 h | 1.80 (indirect) | Si/SiO$_2$/SbSI/ITO | I$_p$@V$_{Bias}$ = ~2.6 nA at +5 V, 147.2 mW/cm$^2$; noise equivalent power = 1.7 × 10$^{-10}$ W/Hz$^{1/2}$ |
| | SbSI[156] | chemical bath + vapor annealing | step 1 Sb$_2$S$_3$: sodium thiosulfate in water + SbCl$_3$ in acetone + water: reaction for 2 h at RT + annealing in Ar atm at 300 °C for 5 min; step 2 SbSI: thermal treatment of Sb$_2$S$_3$ in an inert atm using SbI$_3$ vapor at 250 °C for 5–10 min | 1.9 (indirect) | FTO/SbSI/PMMA/Au | I$_p$@V$_{Bias}$ = ~40 nA at 0 V, 100 mW/cm$^2$; specific detectivity = 10$^9$ Jones |
| | SbSI[260] | hydrothermal | aqueous SbCl$_3$ + thiourea + I$_2$: 180 °C for 10 h | 1.9 (indirect) | Si/SiO$_2$/SbSI/PbI$_2$/Ag | I$_p$@V$_{Bias}$ = ~1 nA at 5 V, 0.65 mW/cm$^2$, under 650 nm light irradiation; responsivity = 26.3 mA W$^{-1}$; specific detectivity = 4.37 × 10$^{13}$ Jones at 650 nm and a light intensity of 0.084 mW/cm$^2$ |
| | SbSI[261] | hydrothermal | aqueous SbCl$_3$ + S powder + I$_2$: 180 °C for 20 h | 1.87 (indirect) | Si/SiO$_2$/SbSI/Ag (Rigid); PI/SbSI/Ag (flexible) | I$_p$@V$_{Bias}$ = ~2.918 nA (rigid) at 0.81 mW cm$^{-2}$ and ~1.7 nA (flexible) at 0.5 mW/cm$^2$ at 5 V and 635 nm light irradiation, respectively; responsivity = 18.50 mA W$^{1-}$ (rigid) and 13.74 mA W$^{1-}$ (flexible); specific detectivity = 7.32 × 10$^{10}$ Jones (rigid) and 5.43 × 10$^{10}$ Jones (flexible) |
| nanogenerators | SbSI[262] | solid-state reaction | Sb + S + I$_2$ powders heated in tubular furnace at 250 and 350 °C for 1 h | - | PET/SbSI/PMMA/Ag (PNG) | V = ~5 V; I = ~150 nA |
| | SbSeI[263] | sonochemical | Sb + Se + I$_2$ powders in ethanol: 50 °C for 2 h | - | Au/SbSeI/Au | V = 0.012 V; I = 11 nA; P$_d$ = 0.59 μW/m$^2$ |
| photocatalysis | SbSI[246] | sonochemical | Sb + S + I$_2$ powders in isopropyl alcohol: 60 °C for 6 h | 1.91 (indirect) | electrode = PET/ITO/SbSI; reagents = 0.1 M KNO$_3$ + 10 mM KI, Ar purged; light source: xenon lamp (150 W) | I = ~−0.5 μA at 0 V vs SHE (+400 nm illumination) |
| | SbSI[247] | reflux | SbCl$_3$ + thioacetamide + KI in glacial acetic acid; 110 °C for 2 h | 1.84 (indirect); 1.94 (direct) | reagent: methyl orange; light source: 1 Sun, 1.5G; incident light: λ ≥ 400 nm; scavenging reagents = benzoquinone, ammonium oxalate, sodium azide, and isopropanol | degradation efficiency = 97% after 20 min under the visible light irradiation; stability = negligible decay after 5 cycles |
| | SbSI[253] | hydrothermal + ball milling | step 1 SbSI crystals: SbCl$_3$ + thiourea + NH$_4$I in aqueous HCl: 160 °C for 24 h; step 2 SbSI NCs: SbSI crystals + ball mill for 5 h | 1.77 | reagent: methyl orange; light source: xenon lamp, power of ~400 mW/cm$^2$; incident light: λ ≥ 420 nm | degradation efficiency = 98% after 5 min under the visible light irradiation; stability = fairly good |
| | SbSI[248] | sonochemical | Sb + S + I$_2$ powders in methanol ultrasonication at 65 °C for 80 min, followed by drying at 90 °C for 3 h | 1.85 | catalysts: SbSI@CNTs; reagent: acid blue 92 (AB92); light source: xenon lamp, power of ~400 mW/cm$^2$; incident light: λ ≥ 420 nm | degradation efficiency = 90% after 90 min. under the visible light irradiation; stability = favorable |

**Table 4. continued**

| application | material | deposition | reaction conditions | band gap (eV) | device structure / measurement conditions | performance |
|---|---|---|---|---|---|---|
| solar cells | SbSI[147] | chemical bath + spin coating | step 1 $Sb_2S_3$: sodium thiosulfate in water + $SbCl_3$ in acetone + water: reaction at 10 °C, followed by annealing in Ar atm at 300 °C for 5 min; step 2 SbSI: $SbI_3$ in DMF spin coated on $Sb_2S_3$, followed by annealing at 150 °C for 5 min in an inert atm | 2.15 | FTO/BL-TiO₂/mp-TiO2/SbSI/PCPDTBT/Au | $J_{sc}$ = 9.11 mA/cm², $V_{oc}$ = 0.58 V, FF = 57.7%, PCE = 3.05% |
| | SbSI[232] | two-step spin coating | step 1 $Sb_2S_3$: $SbCl_3$ + thiourea in DMF spin-coated, followed by heat treatment at 150 °C for 5 min inside glovebox; step 2 SbSI: spin coating of $SbI_3$ in NMP/DMSO solution on $Sb_2S_3$ followed by annealing at ~200 °C for 1 h | 1.96 | FTO/TiO₂/SbSI/P₃HT/Au | $J_{sc}$ = 5.45 mA/cm², $V_{oc}$ = 0.548 V, FF = 31%, PCE = 0.93% |
| | $Sb_{0.67}Bi_{0.33}SI$[234] | chemical bath + spin coating | step 1 $Sb_2S_3$: sodium thiosulfate in water + $SbCl_3$ in acetone + water, reaction at 10 °C, followed by annealing in Ar atm at 300 °C for 5 min; step 2 $Sb_{0.67}Bi_{0.33}SI$: $BiI_3$ in DMF spin coated on $Sb_2S_3$ followed by annealing at 250 °C for 2 min in an inert atm | 1.62 | FTO/BL-TiO₂/mp-TiO2/SbSI/PCPDTBT/Au | $J_{sc}$ = 14.54 mA/cm², $V_{oc}$ = 0.53 V, FF = 52.8%, PCE = 4.07% |

$Bi_{13}S_{18}I_2$. BiSI and $Bi_{13}S_{18}I_2$ were crystallized in orthorhombic (*Pnma*) and hexagonal (*P6₃*) phases exhibiting an *n*-type indirect band gap of 0.75 and 1.57 eV, respectively. The preliminary $Bi_{13}S_{18}I_2$-based solar cell showed the highest PCE of 0.85% with $J_{sc}$ of 3.82 mA/cm², $V_{oc}$ of 0.58 V, and FF of 38.3% with high repeatability and stability (Figure 12i). The lower device performance was due to the diminished device structure, and poor crystallinity, which caused low $J_{sc}$ and FF. The authors further demonstrated a physical vapor deposition (PVD) method to prepare uniform $Bi_{13}S_{18}X_2$ (X = I, Br, Cl) thin films, which is a prerequisite for fabricating high-efficiency solar cells. Solar cells were fabricated based on $Bi_{13}S_{18}X_2$ thin films with device configuration of FTO/TiO₂/$Bi_{13}S_{18}X_2$/($I_3^-$/$I^-$ redox couple)/Pt. Interestingly, device efficiencies increased in the order of $Bi_{13}S_{18}I_2$ (0.75%) < $Bi_{13}S_{18}Cl_2$(0.91%) < $Bi_{13}S_{18}Br_2$ (1.12%). The higher performance of $Bi_{13}S_{18}Br_2$ among other devices is attributed to its higher light-absorption ability as well as the ability of the PVD method to deposit highly dense and controlled $Bi_{13}S_{18}X_2$ film. It has been demonstrated that these Bi-based chalcohalides are indirect band gap semiconductors, implying that a thicker absorber is required to maximize light absorption. However, it causes trap densities in the absorber, resulting in lower device efficiency, and thus minimizing impurities is an effective way of improving device performance in solar cell devices. Therefore, future work focusing on reducing trap densities by optimizing the impurities in Bi-based chalcohalides is considered critical for fabricating high-efficiency solar cell devices.

*5.2.1.2. Sb-Based Chalcohalides.* Seok and co-workers at UNIST, South Korea reported a first working solar cell device based on SbSI with PCE of 3.05% under standard illumination conditions of 100 mW/cm².[147] A two-step approach demonstrated by Godel and Steiner[156] with slight modification was used to deposit SbSI absorber. First, $Sb_2S_3$ was deposited onto a mesoporous (ms)-TiO₂ electrode as an ETL using chemical bath deposition at 90 °C, followed by a spin coating of $SbI_3$ in DMSO solution and then subsequent annealing at 150 °C for 5 min. in an inert atmosphere (Figure 13a) and finally, the device was finished by depositing the different HTM, and evaporating Au as front contacts. Figure 13b and its inset show the cross-sectional FE-SEM image and photograph of the completed device with the FTO/BL/mp-TiO₂/SbSI/HTL/Au, respectively. Initial devices fabricated using different HTL showed a highest efficiency of 2.84% for a poly[2,6-(4,4-bis(2-ethylhexyl)-4H-cyclopenta[2,1-b;3,4-b′]dithiophene)-alt-4,7-(2,1,3-benzothiadiazole)] (PCPDTBT) HTL, which was further improved to 3.05% by thorough optimization of annealing temperature and $SbI_3$ solution concentration. Notably, unencapsulated SbSI solar cell device retained 93% of its initial efficiency after storing for 15 days in ambient conditions (~60% humidity, ~25 °C temperature). This work demonstrated the potential of SbSI as an absorber in solar cells that sparked an interest in the researchers to further demonstrate alternative synthesis methods as well as to improve the device efficiency. Choi et al.[232] demonstrated an alternative two-step approach. The $Sb_2S_3$ was deposited using molecular solution processing that was further converted to SbSI by reacting with $SbI_3$. The motivation behind employing molecular solution processing for $Sb_2S_3$ was to overcome the issues associated with the CBD method such as the formation of impurity phases and difficulty in controlling the Sb/S ratio.[233] Controlled experiments were carried out to elucidate the effect of annealing temperatures, $SbCl_3$/thiourea ratio, reaction times after spin coating of $SbI_3$ solution, and
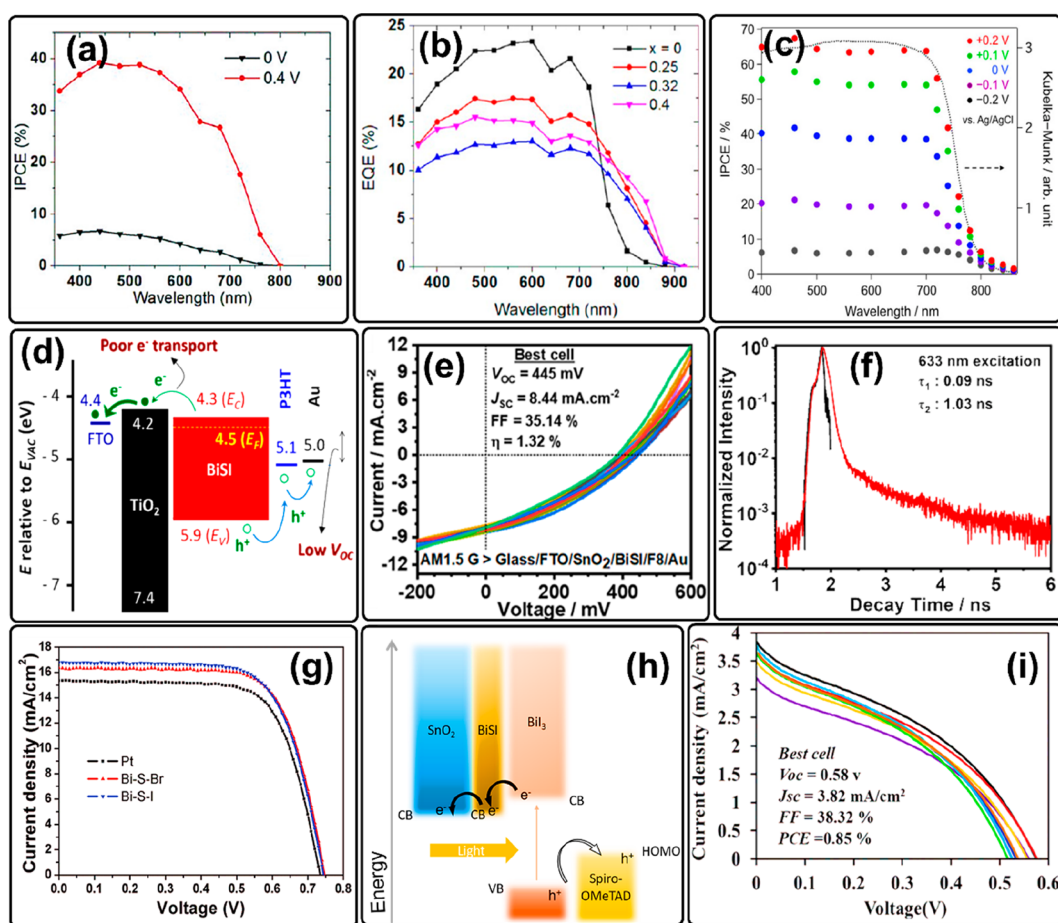
**Figure 12.** (a) IPCE spectra of BiSI films deposited at 275 °C. Reproduced with permission from ref 224. Copyright 2012 American Chemical Society. (b) Short-circuit IPCE values measured for films ($BiS_{1-x}Se_xI$) with various Se/(S + Se) levels measured in a two-electrode cell containing $I^-/I_2$ in acetonitrile. Reproduced with permission from ref 106. Copyright 2012 American Chemical Society. (c) IPCE spectra of the BiSI electrode in an acetonitrile solution containing 0.1 M NaI at various applied potentials and absorption spectrums of BiSI. Reproduced with permission from ref 76. Copyright 2016 Nature Publishing Ltd. (d) Energy-level band diagram of BiSI with a conducting oxide (FTO), ETL ($TiO_2$), HTM (P3HT), and electrode (Au). Reproduced with permission from ref 225. Copyright 2019 MDPI. (e) $J−V$ characteristics of 16 devices with the architecture of glass/ F-$SnO_2$/$SnO_2$/BiSI(150 nm)/F8/Au. (f) Time-resolved PL of BiSI films employing 633 nm excitation. (e, f) Reproduced with permission from ref 190. Copyright 2019 American Chemical Society. (g) $J−V$ curves of the DSSCs using bismuth-based chalcohalide and Pt as CEs. Reproduced with permission from ref 192. Copyright 2017 The Royal Society of Chemistry. (h) Schematic illustration of charge transfer processes in BiSI-based device. The energy levels of BiSI and $BiI_3$ are based on literature data: CB of $SnO_2$, −4.5 eV; CB of BiSI, −4.5 eV; CB of $BiI_3$, −4.1 eV; VB of $BiI_3$, −5.9 eV; HOMO of spiro-OMeTAD, −5.1 eV. Reproduced with permission from ref 104. Copyright 2019 American Chemical Society. (i) $J−V$ curves of eight devices based on $Bi_{13}S_{18}I_2$-based solar cells. Reproduced with permission from ref 181. Copyright 2020 The Royal Society of Chemistry.

different solvents for $SbI_3$ dissolution, on the growth of SbSI films. Finally, solar cell device fabricated based on SbSI absorber using $TiO_2$ as ETL and poly(3-hexylthiophene) (P3HT) as HTL with the configuration of FTO/mp-$TiO_2$/SbSI/P3HT/Au showed a PCE of 0.93% and well maintained PCE after exposing to ambient air for a month. Seok and co-workers further demonstrated improved PCE of SbSI-based devices to 4.07% by partially substituting Sb by Bi ($Sb_{0.67}Bi_{0.33}SI$, ASBSI).[234] Authors focused on achieving better performance by tuning the bandgap as substituting Sb by Bi can decrease the bandgap between 1.83 eV (SbSI) to 1.51 eV (BiSI). Following their previous recipe with slight modifications, the authors prepared ASBSI absorbers showing the bandgap energy of 1.62 eV (Figure 13c, inset). The visual appearance of thin films from Figure 13c, inset also confirms the tuned band gap energy of ASBSI thin films. Thorough investigations were carried out for controlled sensitization of the absorber layer onto the pores of mp-$TiO_2$ because sufficient infiltration of HTL is necessary for high-performance solar cell devices. Authors revealed that a higher

CBD time of 3.5 h sensitized excessive ASBSI absorber layer onto the mp-$TiO_2$, which obstructed the penetration of HTL, leaving behind more pores at the bottom of the device (Figure 13d,e). They concluded that if HTL does not uniformly infiltrate to the bottom of the electrode (Figure 13e, left), the holes generated in the ASBSI cannot be efficiently transferred to the front contact. Finally, the best performing device was fabricated using FTO/BL-$TiO_2$/mp$TiO_2$/ASBSI/PCPDTBT:PC60BM (10:5)/PEDOT:PSS/Au configuration that showed the highest efficiency of 4.07% (Figure 13f). Notably, the unencapsulated solar cell device exhibited outstanding stability and retained ∼93% of the initial PCE after illumination for ∼20.9 h at RT (Figure 13g), and ∼92% of its initial PCE after storing for 360 h at 85 °C in air under 40% average relative humidity in the dark (Figure 13h). SbSeI has a narrow band gap energy of ∼1.67 eV (compared to 2.1 eV for SbSI), which maximizes the light absorption and thereby the device performance.[235,236] In addition, the closer ionic radii match between $Se^{2-}$ (198 pm)[237] and $I^{1-}$ (220 pm)[237] compared to that between ionic
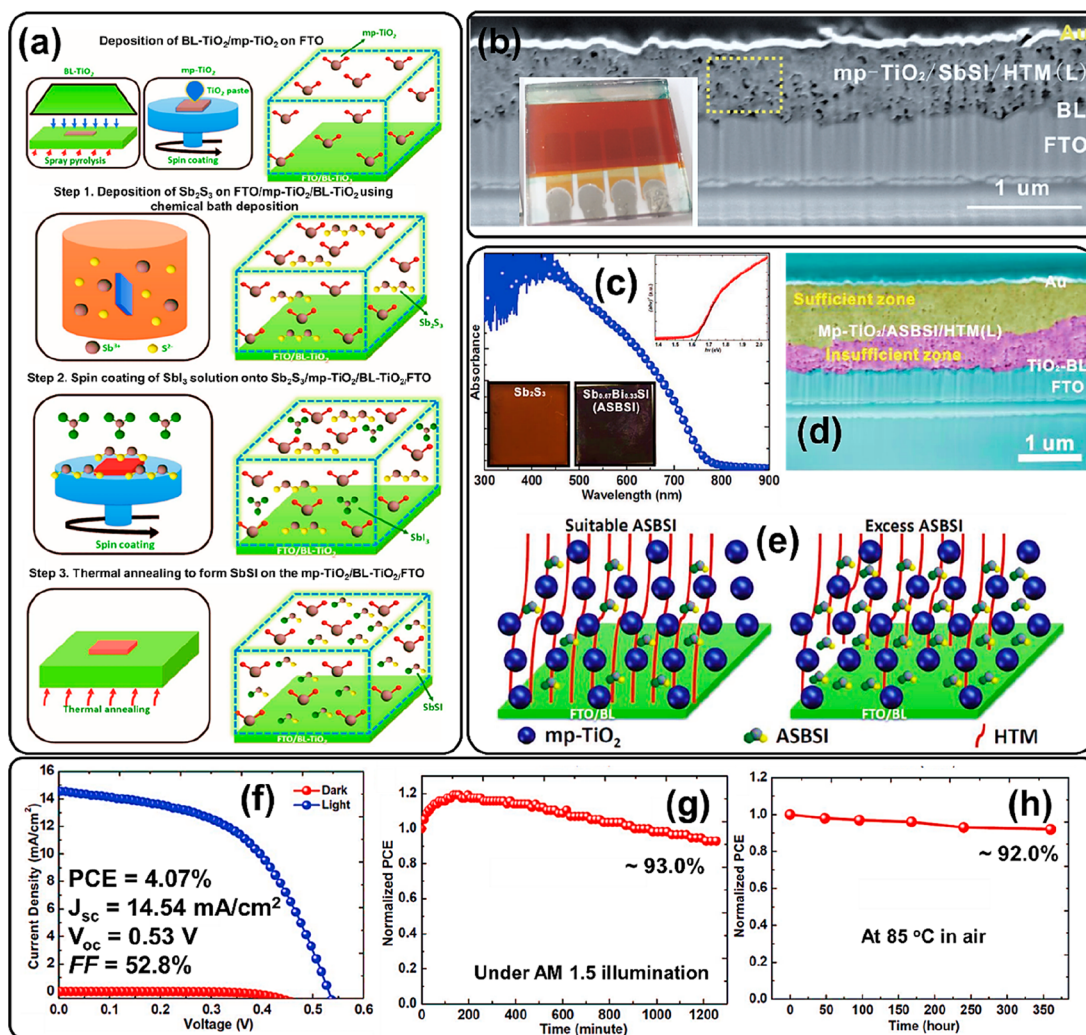
**Figure 13.** (a) Schematic illustration of the preparation of SbSI via two-step process followed by thermal annealing. (b) Cross-sectional FE-SEM image of the device with the FTO/BL/mp-TiO$_2$/SbSI/HTL/Au structure. The inset of (b) shows the photograph of the finished device. (a, b) Reproduced with permission from ref 147. Copyright 2018 John Wiley and Sons. (c) UV−visible absorption spectrum of Sb$_{0.67}$Bi$_{0.33}$SI (ASBSI). The insets in (c) are the Tauc plot of ASBSI and the photos of Sb$_2$S$_3$ and ASBSI thin films. (d) Cross-sectional FE-SEM image of the device with FTO/BL/mp-TiO$_2$/ASBSI/HTM(L)/Au structure fabricated via CBD of Sb$_2$S$_3$ for 3.5 h. (e) Schematic demonstrating the influence of the ASBSI amount on the infiltration of HTM in ASBSI devices. (f) $J−V$ curves under dark and standard illumination conditions, and stability tests showing normalized PCE (g) under standard AM 1.5G illumination at RT for 1200 min and (h) measured at 85 °C in air for 350 h under 40% average relative humidity in the dark. (c−h) Reproduced with permission from ref 234. Copyright 2019 John Wiley and Sons.

radii of S$^{2−}$ (184 pm)[237] and I$^{1−}$ (220 pm)[237] could produce superior and more stable crystal phases and thereby improve the device stability. Considering these benefits, a first solar cell device based on SbSeI with the efficiency of ~4.1% and stability ~38 h was demonstrated.[238] A two-step solution approach was determined to prepare SbSeI thin films, where SbI$_3$ solution was spin-coated on Sb$_2$Se$_3$ prepared by thermal decomposition of single-source precursor $[((SbL_2Cl_2)Cl)_2 \cdot (CH_3)_2CO$, where L = $N,N$-dimethyl selenourea]. Although the device efficiency of these Sb-based chalcohalide materials is significantly lower than that of Pb halide-based perovskite solar cells, promising initial device efficiencies demonstrated by a group of Prof. Seok at UNIST, South Korea, and comprehensive stability of these materials, demonstrate their potential in next-generation solar cell devices. The device performance of Sb-based chalcohalides is influenced by several important parameters. It includes immature synthesis methodologies, insolubility of some necessary precursors (in solution processing), poor microstructure, phase impurities (usually halide), unoptimized device

structure, and meager understanding of defect states, recombination losses, HTL, and ETL. We urge future studies on the systematic investigation of these key limiting factors that will certainly help the research community to realize the full potential of Sb-based chalcohalide materials as a Pb-free alternative solar cell technology.

**5.2.2. Photocatalysis.** Fundamental criteria of ideal photocatalysts are (1) optimal band gap, (2) suitable band alignment, and (3) stability in an electrolyte solution.[239] Few other desirable properties are good electron and hole mobilities as well as high carrier mobility to enhance charge separation and transfer, respectively. Since photocatalysis only occurs on the surfaces of the photocatalyst, the photogenerated charge carriers must diffuse toward the surface of the photocatalyst.[240,241] Therefore, crystallinity and active surface area of the photocatalyst are also of interest as high crystallinity enhances the charge transport, whereas a high active surface area offers more active sites for photocatalysis.[242] Because of their highly tunable physicochemical and optoelectronic properties, chalcohalides
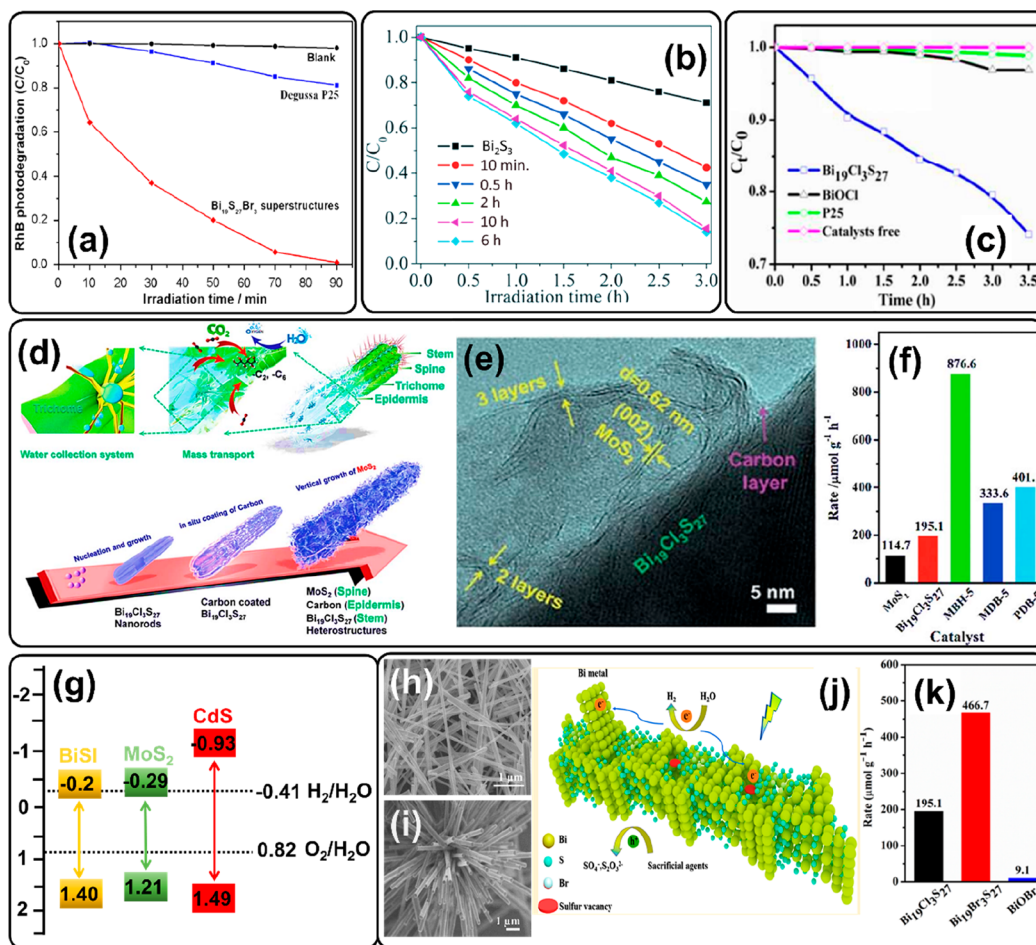
**Figure 14.** Photodegradation efficiency curves of (a) RhB using $Bi_{19}S_27Br_3$ superstructures. Reproduced with permission from ref 226. Copyright 2013 Elsevier. (b) 2,4-Dichlorophenol samples with $Bi_2S_3$ and $Bi_{19}Br_3S_{27}$ prepared over different reaction times. Reproduced with permission from ref 227. Copyright 2015 The Royal Society of Chemistry. (c) Reduction Cr(VI) solution using $Bi_{19}Cl_3S_{27}$ nanorods photocatalyst. Reproduced with permission from ref 228. Copyright 2017 The Royal Society of Chemistry. (d) Schematic diagram of the $MoS_2/Bi_{19}Cl_3S_{27}$ (MBH) biomimetic heterostructure. (e) HR-TEM images of MBH-5. (f) Photocatalytic hydrogen evolution rate of $MoS_2$, $Bi_{19}Cl_3S_{27}$, MBH-5, MDB-5, and PDB-5. (d−f) Reproduced with permission from ref 229. Copyright 2018 The Royal Society of Chemistry. (g) Schematic of experimental energy potentials of BiSI, $MoS_2$, and CdS. Reproduced with permission from ref 108. Copyright 2019 American Chemical Society. (h, i) SEM images of $Bi_{19}Cl_3S_{27}$ nanorods and $Bi_{19}Br_3S_{27}$ nanograsses prepared at 180 and 200 °C, respectively. (j) Schematic representation of charge carrier recombination in $Bi_{19}Br_3S_{27}$ nanograsses prepared at 220 °C. (k) Photocatalytic hydrogen evolution rate of $Bi_{19}Cl_3S_{27}$ nanorods and $Bi_{19}Br_3S_{27}$ nanograsses prepared at 180 and 200 °C, respectively, and BiOBr nanosheets. (h−k) Reproduced with permission from ref 230. Copyright 2019 American Chemical Society.

have received a lot of attention as photocatalytic materials for both water electrolysis and wastewater treatment. Furthermore, chalcohalides with mixed chalcogen and halogen ions have structural flexibility, including layered structures with aniso-tropic charge transfer properties, which have a significant impact on their photocatalytic properties. There have been a number of chalcohalide-based photocatalysts reported to date, with some demonstrating efficiency superior/comparable to their chalco-genide[243,244] and halide perovskite counterparts.[163,245] As a result, we believe that mixed anion-based photocatalyst materials hold great promise for future practical applications.

*5.2.2.1. Bi-Based Chalcohalides.* One of the most extensively researched applications of these Bi-based chalcohalide materials is photocatalysis. Attempts have been made to utilize the different Bi-based chalcohalide materials in different nanostruc-tures/heterostructures as photocatalysts for photodegradation of rhodamine B (RhB)/2,4-dichlorophenol/Cr species and $H_2$ evolution. As described in section 5.1, the synthesis of Bi-based chalcohalides was mostly limited to the growth of single crystals or nanorod crystals using common techniques such as vapor

transport, hydrothermal, and solvothermal methods. The microwave-assisted aqueous approach was used for the first time in 2013 to produce 2D fabric-like hexagonal $Bi_{19}S_{27}Br_3$ superstructures with a band gap energy of 1.42 eV.[226] $Bi_{19}S_{27}Br_3$ superstructures showed an outstanding degradation efficiency rate of 95% toward RhB as a visible light photocatalyst, far superior to the Degussa P25 (Figure 14a). It is well-known that the 1D nanostructures often offer significant photocatalytic activity toward $H_2$ evolution or photodegradation of dyes over their 2D and 3D nanostructures. Keeping this in mind, 1D nanorods of hexagonal $Bi_{19}Br_3S_{27}$ with a band gap of 1.49 eV were prepared through a general and facile one-pot solvothermal method in a mixture of glycerol/ethanol solvent.[227] The formation of 1D $Bi_{19}Br_3S_{27}$ nanorods occurred via fast nucleation and anisotropic growth process. As a result of thiourea hydrolysis, the Biglycerol complex first reacted with the $S^{2-}$ anions to form $Bi_2S_3$ NCs. Similarly Biglycerol complex reacted with $Br^-$ to form $BiBr_3$. Finally, the in situ reaction of formed $Bi_2S_3$ NCs with $BiBr_3$ led to the nucleation of $Bi_{19}Br_3S_{27}$ crystals. The excess use of CTAB as a capping agent was further
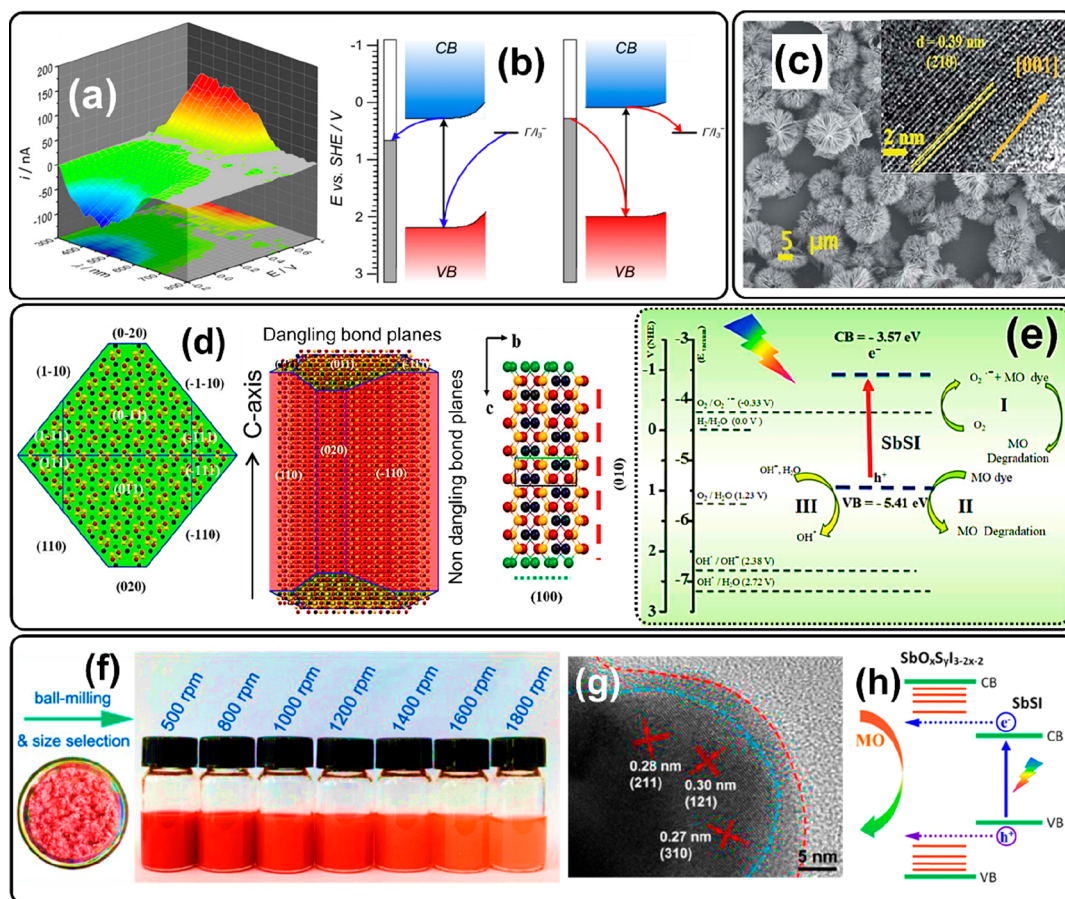
**Figure 15.** (a) Photocurrent action spectrum recorded at different steps for SbSI electrode in 0.1 M KNO$_3$ + 10 mM KI under Ar purging condition. (b) Schematic representation of anodic (left panel) and cathodic (right panel) photoelectrochemical current switching effect in SbSI electrodes in the electrolyte. (a, b) Reproduced with permission from ref 246. Copyright 2015 IOP Publishing Ltd. (c) Low-magnification SEM image of "urchin" shaped SbSI. Inset shows the HR-TEM image with $d$-spacing value corresponds to (210) plane of SbSI. (d) View of the simulated morphology of SbSI along the $c$-axis (left) and $b$-axis (center) and corresponding stacked $[(SbSI)_\infty]_2$ ribbons along $a$-axis (right). Red dotted lines are a representation of nondangling bond planes. Where, red, black, yellow, and green spheres represent Sb, I, S, and the dangling bond atoms, respectively. (e) Schematic diagram of the photodegradation mechanism of methyl orange (MO) using SbSI photocatalyst, suggesting that the pathways (I and II) are more favorable than III. (c—e) Reproduced with permission from ref 247. Copyright 2016 The Royal Society of Chemistry. (f) Photographs of hydrothermally synthesized SbSI crystals (left) and ball milled SbSI followed by the size-selective precipitated nanocrystals dispersed in water (right). (g) HR-TEM image of a SbSI NC showing crystalline core and an amorphous shell. (h) Schematic illustration of defect state-facilitated charge carrier transfer mechanism in core/shell SbSI NC-based photocatalyst. (f—h) Reproduced with permission from ref 253. Copyright 2018, American Chemical Society.

selectively absorbed onto certain crystal planes to accelerate the preferential growth along with the polar direction of Bi$_{19}$Br$_3$S$_{27}$ crystal nuclei, leading to the formation of 1D nanorods. The 1D Bi$_{19}$Br$_3$S$_{27}$ nanorod photocatalyst showed a photodegradation of 2,4-dichlorophenol with an efficiency of ∼85.6% after visible light irradiation for 3 h, which is significantly higher than the Bi$_2$S$_3$ (∼28.8%), demonstrating the potential of chalcohalides over their chalcogenide counterparts (Figure 14b).[227] Immediately after, single-crystalline hexagonal Bi$_{19}$S$_{27}$Cl$_3$ nanorods with several micrometers in length and ∼25 nm in diameter were synthesized via a one-pot template-free solvothermal method.[228] Nanorods displayed a narrow band gap of 1.6 eV, assisted for photoreduction of hazardous Cr(VI) species (Figure 14c) and photodegradation of RhB. The 1D nanorods offer an efficient electron transfer rate because of closer contact of Cr(VI) ions or RhB and Bi$_{19}$S$_{27}$Cl$_3$. In addition, nanorods can also facilitate the diffusion of reactants and products during photocatalysis. Thus, these different factors synergistically led to the excellent photocatalytic activity of Bi$_{19}$S$_{27}$Cl$_3$ nanorods compared to

BiOCl and commercial P25. Similar to nanostructures, heterostructures offer several advantages such as a strong coupling of different active structures, enhanced electron transfer rate at the interface and a promising platform to enable synergistic effects. In this regard, the earlier group shortly reported the in situ hydrothermal synthesis of cactus-like MoS$_2$/Bi$_{19}$S$_{27}$Cl$_3$ (MBH) biomimetic heterostructures. Bi$_{19}$S$_{27}$Cl$_3$ acted as a backbone to provide a stem for MoS$_2$, whereas glucose served as a binder to help MoS$_2$ nanosheets grow along the Bi$_{19}$S$_{27}$Cl$_3$ longitudinal axis during the heterostructure formation (Figure 14d).[229] It was further revealed that the MoS$_2$ nanosheets in MBH showed less stacking and fewer layers. It was also confirmed that the carbon from glucose promoted the transmission of carriers and acted as a binder for MoS$_2$ and Bi$_{19}$S$_{27}$Cl$_3$ to form MBH heterostructure (Figure 14e). Consequently, the MBH photocatalyst outperformed among the different photocatalysts and exhibited a photocatalytic H$_2$ evolution rate up to 876.6 mmol g$^{-1}$ h$^{-1}$ for optimal loading of 5 wt% MoS$_2$ (Figure 14f) with great stability. Following this work,

multi-interface n−p−n double heterojunctions based on BiSI/MoS$_2$/CdS were demonstrated as photocatalyst for H$_2$ evolution.[108] The built-in electric field along the radial direction of the BiSI nanorod and MoS$_2$ interlayer assisted to transport carriers within the lifetime, which was optimized by the multi-interface structure using PL and UV−vis. This also explained the increased photoactivity from the perspective of optical and dynamic properties of BiSI/MoS$_2$/CdS photocatalyst. Moreover, the favorable band alignment between BiSI, MoS$_2$, and CdS (Figure 14g) further allowed the effective separation of photogenerated charge carriers; as a result, BiSI/MoS$_2$/CdS photocatalyst showed an H$_2$ evolution rate of 21 mmol g$^{-1}$ h$^{-1}$, which was significantly higher than its other counterparts. Recently, the influence of halogens on the photocatalytic H$_2$ evolution for Bi$_{19}$X$_3$S$_{27}$ (X = Cl, Br) nanomaterials synthesized by the solvothermal method was investigated.[230] The halogen anions had an impact not only on the morphology but also on the H$_2$ evolution performance of Bi$_{19}$X$_3$S$_{27}$ nanomaterials. It was found that Bi$_{19}$Cl$_3$S$_{27}$ synthesized at 180 °C showed nanorods morphology, whereas Bi$_{19}$Br$_3$S$_{27}$ synthesized at 200 °C showed nanograsses morphology (Figure 14h.i), which was attributed to the difference in properties caused by changes in halogen anions. Surprisingly, Bi$_{19}$Br$_3$S$_{27}$ nanograsses prepared at 220 °C showed an adverse tendency in PL intensity. This was attributed to the presence of metallic Bi and sulfur vacancies that supplied recombination sites as schematically shown in Figure 14j. Consequently, photocatalysts based on Bi$_{19}$Cl$_3$S$_{27}$ nanorods and Bi$_{19}$Br$_3$S$_{27}$ nanograsses showed significantly different H$_2$ evolution rates of 195.1 $\mu$mol g$^{-1}$ h$^{-1}$ and 466.7 $\mu$mol g$^{-1}$ h$^{-1}$, respectively (Figure 14k). The superior performance of Bi$_{19}$Br$_3$S$_{27}$ nanograsses was attributed to the effective carrier separation compared to that of BiOBr and Bi$_{19}$Cl$_3$S$_{27}$.

*5.2.2.2. Sb-Based Chalcohalides.* Early developments in Sb-based chalcohalide materials revealed that these materials have suitable properties that are prerequisites for photocatalysis and PEC water splitting. Despite the above, these compounds have only been explored for their application in photocatalysis, i.e., photodegradation of dyes and contaminants. Kwolek et al.[246] studied the photoelectrochemistry of SbSI nanowires synthesized using common but most attractive sonochemical method. The 1D structure, large static dielectric constant ($\varepsilon$ = ∼5 × 10$^4$),[71] and outstanding stability in aqueous solution make SbSI an ideal candidate for visible light photocatalysis. To investigate the PEC properties of SbSI, photocurrent spectroscopy was used, in which a constant potential was applied to the SbSI, which was then illuminated with monochromatic light in a specific wavelength range. The photocurrent action spectra of SbSI electrodes in Figure 15a indicates the switching effect, which is caused by the appropriate polarization of the SbSI electrode. Figure 15b further explains the mechanism of the switching effect in the SbSI electrode. Anodic photocurrent was generated when the hole from the VB of SbSI oxidized the iodide in the electrolyte, whereas the cathodic photocurrent was generated when the CB edge of the SbSI higher than the reduction potential of the molecular oxygen-dissolved in the electrolyte. The investigation of photoelectrochemistry of SbSI material further attracted researchers to explore SbSI for photocatalytic applications. Tamilselvan and Bhattacharyya synthesized highly crystalline 1D microrods of SbSI and self-assembled into 3D urchin-shaped structure (Figure 15c) using a simple reflux method at a relatively low temperature of 110 °C for 2 h.[247] It is well-known that the dangling bonds at the surfaces introduce the defects, which act as a center for photogenerated charge carrier recombination in light-absorbing materials.[158] Therefore, thorough investigation on the dangling bonds present at the surface planes of SbSI was carried out using Bravais, Friedel, Donnay, and Harkar (BFDH) law. Figure 15d shows the corresponding simulated morphology of SbSI along the b- and c-axes, as well as the stacked [(SbSI)]$_2$ ribbons along a axis. The results from this modeled structure revealed that the SbSI has a lower proportion of dangling bonds at the surface, suggesting that no/few defects exist in the SbSI urchin-shaped structure, making it the suitable candidate for photocatalysis. The photocatalytic performance of SbSI was further investigated by photodegradation of methyl orange (MO), methylene blue (MB), and RhB dyes. The corresponding photodegradation mechanism for MO dye is presented in Figure 15e, which indicates that the photogenerated holes and O$^{2-}$ generated by the injection of electrons from the CB to the singlet oxygen are primary reactive species in the MO degradation process.

A similar mechanism was reported by Tasviri and Sajadi-Hezave for the visible light photocatalytic activity of SbSI nanowires encapsulated by carbon nanotubes (SbSI@CNTs) toward the degradation of Acid Blue 92 (AB92) organic dye in an aqueous solution.[248] The SbSI@CNTs hybrid 1D nanostructure showed unprecedented improvement in the catalytic activity and photostability toward the visible light photodegradation of AB92 dye when compared to bare SbSI nanowires, demonstrating the effectiveness of designing novel hybrid nanostructures for high-performance energy devices. Controlling the nano size, crystal structure, and surface engineering where charges and/or excitons interact with the reagent, are among the various prerequisites for developing highly efficient visible light photocatalysts.[249−252] Guided by these, Wang et al.[253] demonstrated an interesting two-step approach utilizing the hydrothermal method to prepare bulk SbSI crystals and then ball milling of SbSI crystals followed by the size-selective centrifugation to synthesize SbSI NCs. Figure 15f shows the photographs of hydrothermally synthesized SbSI crystals (left) and ball milled SbSI followed by the size-selective precipitated nanocrystals dispersed in water (right). Along with size control in SbSI NCs, the authors also found the in situ surface engineering of SbSI NCs where the amorphous shell (3 to 5 nm) was formed during the preparation (Figure 15f). Further quantitative analysis revealed that the shell should be composed of SbO$_x$S$_y$I$_{3-2x-2y}$. This core/shell nanostructure was further used as photocatalyst for visible light photodegradation of MO and the possible mechanism related to the SbO$_x$S$_y$I$_{3-2x-2y}$ ($x \approx 1.14$, $y \approx 0.22$) shell was proposed, which is shown in Figure 15g. The shell in type-I structure may passivate the surface trap states in SbSI, leading to a longer lifetime of photogenerated charge carrier, but the wider band gap of shell confines the exciton in the core and acts as a physical barrier that hinders the access of photogenerated charges to the surface and solvent. Theoretically, this type-I structure is not suitable for photocatalysis. Another possible mechanism is related to the doping features of S and I in the amorphous shell that may introduce the additional defects within the amorphous Sb$_2$O$_3$ shell. This allows an easy transfer of charge carriers to the shell surface when part of these interband states lies between the band gap of the SbSI core (Figure 15h). This would result in the formation of type-II structure, which allows efficient charge separation between core and shell, and, as a result, promotes photocatalytic activity. This work established a pathway for further improving the photocatalytic activity of SbSI materials by designing a type-II structure with other compounds. Other
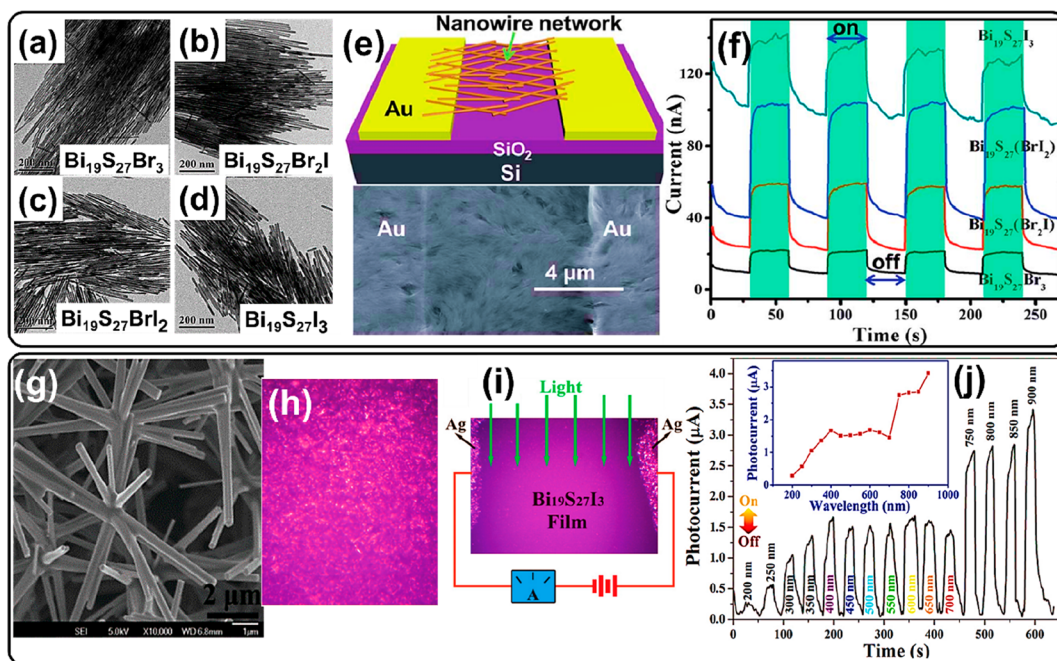
**Figure 16.** Low magnified TEM images of (a) $Bi_{19}S_{27}Br_3$, (b) $Bi_{19}S_{27}Br_2I$, (c) $Bi_{19}S_{27}BrI_2$, and (d) $Bi_{19}S_{27}I_3$ NWs. The scale bars in a, b, c, and d are all 200 nm. (e) Schematic illustration of the photodetector device-based on $Bi_{19}S_{27}(Br_{3-x}I_x)$ NW networks ($x$ = 0, 1, 2, 3) and (f) its transient photoresponse to pulsed incident light at a bias of +5 V. (a−f) Reproduced with permission from ref 174. Copyright 2015 The Royal Society of Chemistry. (g) SEM and (h) optical microscopy images of the $Bi_{19}S_{27}I_3$ nanorod film grown on a glass slide for 20 h. The scale bar for (g) is 2000 nm. (i) Schematic illustration of the photodetector device based on the $Bi_{19}S_{27}I_3$ nanorod cluster film, and (j) its photoresponsivity to light with different wavelengths in the range of 200−900 nm at a fixed DC bias voltage of 10 V. The inset in (j) is the corresponding spectral-dependent photoresponse curve. (g−j) Reproduced with permission from ref 175. Copyright 2018 The Royal Society of Chemistry.

Sb-based chalcohalides, on the other hand, have yet to be investigated for photocatalysis and PEC water splitting.

What is limiting the researchers from exploring these exciting Sb-based chalcohalide materials for photocatalysis and PEC water splitting? First and foremost, there is a lack of recognition of which Sb-based chalcohalides are suitable and which of their properties would contribute to these applications. Second, there is a lack of understanding of band alignment of CBM and VBM in Sb-based chalcohalides concerning normal hydrogen electrode (NHE) potential. On the other hand, the band alignment of the materials is highly dependent on the environment, grain orientation, and interface configuration, etc., and this can be rather complicated.[254−258] Future research should focus on theoretical simulation and experimental measurements of band alignment of Sb-based chalcohalides to assess band positions and ultimately realize their application in high-efficiency photocatalysis and water splitting devices.

**5.2.3. Photodetectors.** Photodetectors, which can convert incident light (ultraviolet (UV), visible, or infrared (IR)) into electrical signals, are attracting increasing attention for variety of scientific and industrial applications including image sensing, optical communications, chemical/biological detection, and environmental monitoring.[264−266] A crucial component of a photodetector is a high-quality semiconductor, which produces electrical current by absorbing light, generating electron−hole pairs, and separating them using an applied and built-in electric field.[264,265] These chalcohalides have been investigated for their potential use in light detection due to their similar optoelectronic properties to halide perovskites, but with the added benefits of high stability. Few exciting results for chalcohalide photodetectors fabricated with various device configurations have been reported in recent years,[267−270] some

of which have demonstrated significant photodetecting performances. In this section, we discuss their recent advances with an emphasis on their unique properties and performance, and we highlight the most interesting works in this field.

*5.2.3.1. Bi-Based Chalcohalides.* Wu et al.[174] were the first to report the photodetector device based on $Bi_{19}S_{27}(Br_{3-x}, I_x)$ alloyed NWs. Notably, this is also the first attempt to demonstrate a facile, colloidal approach to synthesize well-defined $Bi_{19}S_{27}(Br_{3-x}, I_x)$ alloyed NWs using $Al^{3+}$ ions to mediate the oriented growth. The presence of both $Al(acac)_3$ and $AlCl_3$ produced NWs; however, the reaction conditions also played an important role in producing NWs with narrow size distributions. For example, the length of as-synthesized $Bi_{19}S_{27}Br_3$ NWs tuned in the range of 0.15−2 $\mu$m by varying the reaction time, whereas mean diameters tuned from ~6.9 to ~12 nm by varying the reaction temperature. The synthesis expanded to *p*-type $Bi_{19}S_{27}(Br_{3-x}, I_x)$ ($0 \leq x \leq 3$) alloyed nanowires, where diameters increased gradually from ~9.0 to ~13.9 nm as the I content increased (Figure 16a−d). $Bi_{19}S_{27}Br_3$ NWs showed a direct band gap of 0.815 eV, whereas $Bi_{19}S_{27}(Br_{3-x}, I_x)$ NWs ($0 \leq x \leq 3$) exhibited an unusual composition-independent band gap of ~ 0.82 eV, which can be attributed to the smaller contributions of the halogens to the VBM and CBM, confirmed from the theoretical studies. The photodetector device was fabricated using alloyed NWs directly drop casted on a preprepared Au electrode (50 nm) paired onto a $SiO_2$ (300 nm)/$P^+$-Si substrates as shown in Figure 16e. The photodetector demonstrated sensitivity to white light, with a pronounced photoresponse and high stability (Figure 16f), confirming the good potential of chalcohalides in light detection applications.[174] Similarly, the photodetector based on $Bi_{19}S_{27}I_3$ nanorod clusters (Figure 16g,h) directly grown on glass
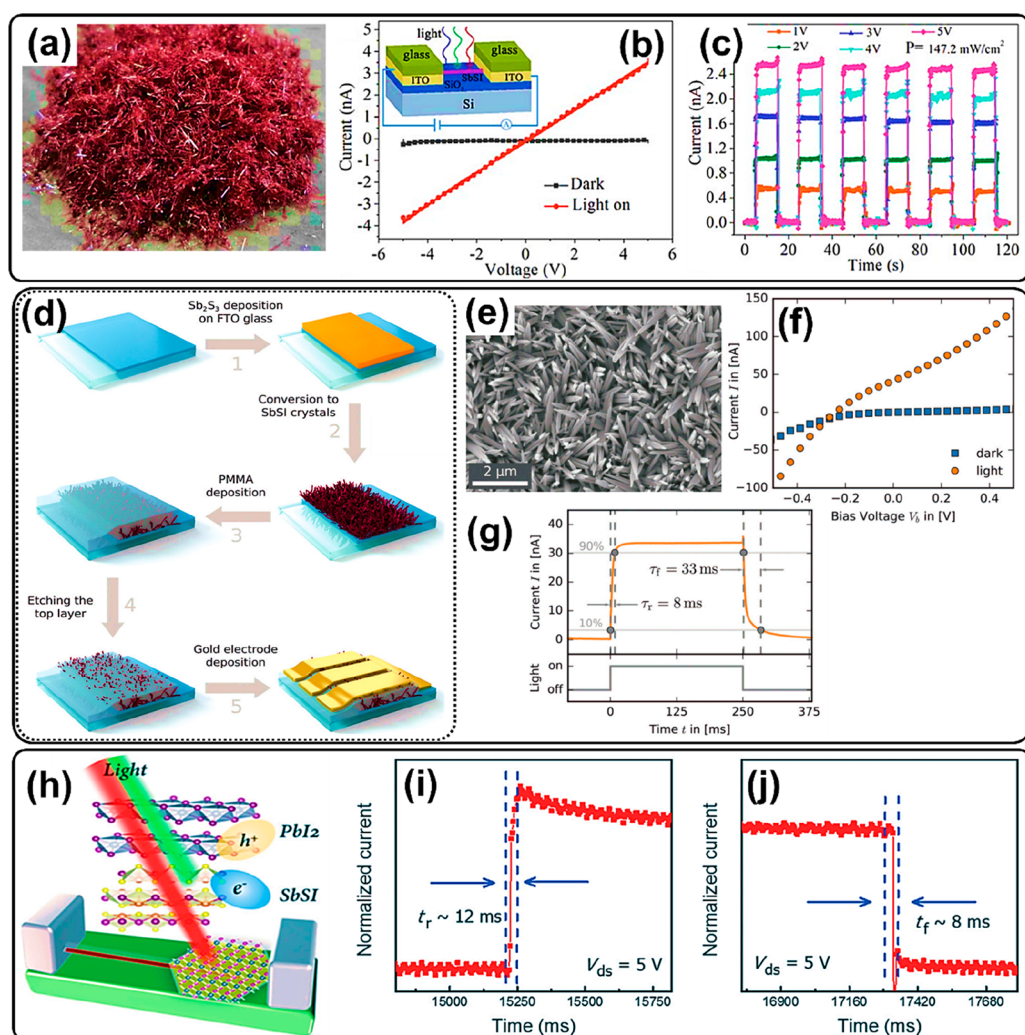
**Figure 17.** (a) Photograph of SbSI crystals synthesized via fast (4 h) and low-temperature (160 °C) hydrothermal method, (b) $I{-}V$ curves of the device in the dark and light (the inset is the schematic of the individual SbSI microrod based photodetector, and (c) its on−off photocurrent response as a function of the time at a bias of 1−5 V with a fixed light intensity of 147.2 mW/cm². (a−c) Reproduced with permission from ref 259. Copyright 2015 The Royal Society of Chemistry. (d) Schematic representation of SbSI photodetector fabrication process in 5 steps. (e) SEM image of as-prepared SbSI microcrystals. (f) $I{-}V$ characteristics of the SbSI photodetector. (g) Detailed view of one modulation cycle of time response of photocurrent of SbSI photodetector showing the rise-time ($\tau_r$) and fall-time ($\tau_f$). (d−g) Reproduced with permission from ref 156. Copyright 2016 The Royal Society of Chemistry. (h) Schematic representation of the vdW heterojunction device formed from the PbI₂ flake and SbSI single-crystal whisker. (i, j) Time-resolved photoresponse of the SbSI/PbI₂ vdW heterojunction device at 5 V bias. The photocurrent raised with a rising time of ∼12 ms when the light was on and dropped rapidly with a falling time of ∼8 ms when the light was switched off. (h−j) Reproduced with permission from ref 260. Copyright 2019 The Royal Society of Chemistry.

substrates using a facile solvothermal method was also reported recently.[175] Bi₁₉S₂₇I₃ nanorod clusters grown on glass showed a strong absorption spanning the whole visible to the near-IR region with band gap energy of 0.83 eV. Notably, the Bi₁₉S₂₇I₃ nanorod photodetector device (Figure 16i) still exhibited a very broad photoresponse ranging from UV to near IR region. As shown in Figure 16j, the device showed a limited photoresponse in the UV region; however, it was able to harness the whole visible light region and notably larger photocurrent in the near-IR region. It was also found that the photocurrent of the Bi₁₉S₂₇I₃ nanorod cluster film was ∼400-times higher than that of powder sample, demonstrating the effectiveness of nanorod structure as well as the great potential of this material in photodetectors. The first photodetector device based on BiSI was recently demonstrated employing an entirely new process for preparing highly pure, carbon-free BiSI thin films.[231] An established simple three-step process includes (1) spin coating of BiI₃ in

tetrahydrofuran (THF) solution on FTO substrate, (2) hydrolysis of BiI₃ in a 1:1 methanol/water solution to form BiOI, and (3) annealing of BiOI in H₂S atmosphere at 150 °C for 4 h to form BiSI thin films. The BiSI thin-film photodetector outperformed among all other chalcohalide in terms of its responsivity and detectivity owing to its controlled band gap. Given that the chalcohalides are still at an early stage of development, these results are very encouraging. Understanding the role of halide ions as well as incorporating different charge transport materials with BiSI and employing encapsulating strategies are key to further improve the performance of Bi-based chalcohalide photodetectors.

*5.2.3.2. Sb-Based Chalcohalides.* Early investigations on the photoelectric property of SbSI material encouraged researchers to further demonstrate its applications in photodetectors. Chen et al.[259] were the first to report detailed studies on the photoresponse performance of 1D SbSI crystal-based photo-

detector. They demonstrated an alternative, low-cost hydro-thermal method to grow 1D crystalline SbSI crystals (Figure 17a). A photodetector based on SbSI microrod equipped with ITO contacts were first-ever fabricated on a $SiO_2/Si$ substrate (Figure 17b and inset), which displayed a noteworthy responsivity of 0.035 mA W$^{1-}$ to visible light with an on–off ratio up to 727 (Figure 17c), a detectivity of $2.3 \times 10^8$ Jones and short response/recovery times (300/190 ms) with high stability. Earlier, most of the reports demonstrated the use of common synthesis methods such as sonochemical or hydrothermal or chemical vapor deposition at high temperatures, which usually require high processing times of 4 h and more and usually result in bulk SbSI crystals. Keeping this in mind, Godel and Steiner demonstrated a novel thin-film deposition method for SbSI microcrystals using two-step methodology as shown in Figure 17d.[156] $Sb_2S_3$ was first deposited using low-temperature chemical bath deposition and then converted to crystalline SbSI using $SbI_3$ vapor at 250 °C for 5 min. The as-deposited SbSI microcrystals (Figure 17e) thin films were further used into sandwich-type photodetector device fabrication, which showed notable improvements in the optoelectronic properties, particularly response (Figure 17f) and recovery time (Figure 17g) by one to 2 orders of magnitude compared to previously reported values in the literature. This sandwich-type SbSI photodetector outperformed the halide perovskite and a high-performance CdSe-nanowire photodetector, revolutionizing the photodetector device fabrication technique for future high efficiency and low-cost light detectors. It has been demonstrated that mixed dimensional van der Waals (vdW) heterostructures show considerable performances and tunable properties and are a multifunctional platform for next-generation optoelectronic devices.[271] Considering the flexibility of strict lattice mismatch-ing requirements in mixed-dimensional vdW heterostructures, Sun et al.[260] reported the first fabrication of a large area (millimeter-sized) heterostructure based on an individual single-crystal SbSI whisker and individual $PbI_2$ flake (Figure 17h) that demonstrates the vdW interaction at the interface. Photo-detector device based on this mixed-dimensional heterostruc-ture showed a photoresponsivity of up to 26.3 mA W$^{1-}$ and a rapid response time (rising/falling time of 12/8 ms, Figure 17i and j, respectively). Although the response time of mixed-dimensional SbSI/$PbI_2$ vdW heterojunction-based photodetec-tor was fast, the photoresponsivity was not remarkable. However, the heterojunction device showed stable and reproducible optoelectronic properties. The authors further claimed that the effective junction area of their device can reach up to $10^5$ $\mu m^2$, which was significantly higher than reported heterostructures.[272] Recently, a similar group reported the first fabrication of a flexible photodetector device based on SbSI micro rods prepared using a hydrothermal method with $SbCl_3$, $I_2$, and sulfur powder.[261] A flexible SbSI microrods-based photodetector device showed a responsivity up to 13.74 mA W$^{1-}$ and the faster response speed (rising/falling time of 61/128 ms), which was superior to previously reported rigid photo-detector devices based on SbSI microcrystals. Raman studies on SbSI microcrystals further revealed the redshift in Sb-S atomic vibrations in SbSI microcrystals than the previously reported SbSI whisker and bulk SbSI crystals, suggesting the decreased force constant of Sb-S bond in SbSI microcrystals. This decrease in force constant of the Sb-S bond adopts a strain parallel to the ab plane or perpendicular to the c-axis, which could relate to the use of sulfur powder instead of commonly used thiourea during the hydrothermal synthesis. This also explained the improved

flexibility of SbSI micro rods than that of SbSI whiskers. However, detailed studies are needed to further understand the effect of sulfur source on improving flexibility.

Although several reports have been focused on the fabrication of SbSI-based photodetectors, the performance of these devices is still comparatively lower than that of state-of-the-art photodetectors.[273] Most of the previous reports used bulk or microcrystal of SbSI to fabricate the devices, which seem to be rather reflective and thus affect the optical absorption of photodetectors. Moreover, the electrical conductivity of SbSI bulk crystals or microcrystals is significantly lower compared to state-of-the-art photodetectors. Future work should focus on developing facile synthesis processes for preparing SbSI NCs by colloidal means, which can improve the optical absorption losses due to their antireflective nature. Additionally, utilizing novel device architecture to fabricate SbSI-based photodetectors, such as Schottky junction with highly conducting carbon compounds, can overcome the conductivity issues and enhance the device performance in the near future. Though SbSI has been used to fabricate photodetector devices, no attempt has been made to fabricate photodetector devices based on its other counterparts such as SbSX (where X = Cl, Br) and SbSeX (where X = I, Cl, Br), which can be explored in future.

**5.2.4. Battery and Supercapacitor.** With the growing demand for the deployment of renewable energy conversion devices, high-performance and low-cost energy storage devices such as batteries and supercapacitors are indeed antici-pated.[274−283] A unique structural properties of chalcohalides, e.g., $Bi_{13}S_{18}I_2$ show ribbon-like subunits of $[(Bi_2S_3)_2]_\infty$ that form six spokes around a central hexagonal channel at the corners of the unit cells and BiSI has a layered structural arrangement, which is suitable for ion-migration making these chalcohalides a promising candidates in energy storage devices. This section summarizes recent advances in the use of chalcohalide materials as electrodes and electrolytes in batteries and supercapacitors.

*5.2.4.1. Bi-Based Chalcohalides.* Bi-based chalcohalides, namely BiSI and $Bi_{13}S_{18}I_2$, have been used as anode materials in lithium-ion battery (LIB) systems.[284] A half-cell retained capacity of 703 mAh g$^{-1}$ was achieved with BiSI/$Bi_{13}S_{18}I_2$, which was comparatively higher than of $Bi_{13}S_{18}I_2$ (601 mAh g$^{-1}$) anode material. The coalescence of structural features was cited as a key to the LIB's high performance. The first chalcohalide reported for use as an electrode material for supercapacitor is a hexagonal $Bi_{13}S_{18}I_2$, which was prepared by thermal decom-position of a precursor solution containing bismuth xanthate, organobismuth material, and $BiI_3$. The $Bi_{13}S_{18}I_2$-based super-capacitor showed the areal capacitance of 210.68 mF cm$^2$ with 99.7% capacitance retention after 5000 cycles, featuring promising energy storage capabilities and better long-term cycle stability.[176] The presence of both Bi(III) and Bi(II) ions in the material resulted in higher capacitance values because the lowest unoccupied CB states are predominantly derived from the $Bi^{2+}$ centers with contributions from the adjacent $Bi^{3+}$ and sulfur ions and the highest occupied VB states were predominantly of iodide in character. This demonstrated the potential of the Bi center to integrate various charges and illustrated the capacitance mechanism.[285] However, the potential of this chalcohalides in energy storage devices including batteries and supercapacitors still remains largely untapped. The precise mechanism of charge storage in chalcohalides is currently unknown. Furthermore, the transport properties of chalcohalides that are affected by defects, carrier concentration, and intrinsic doping are still underexplored.
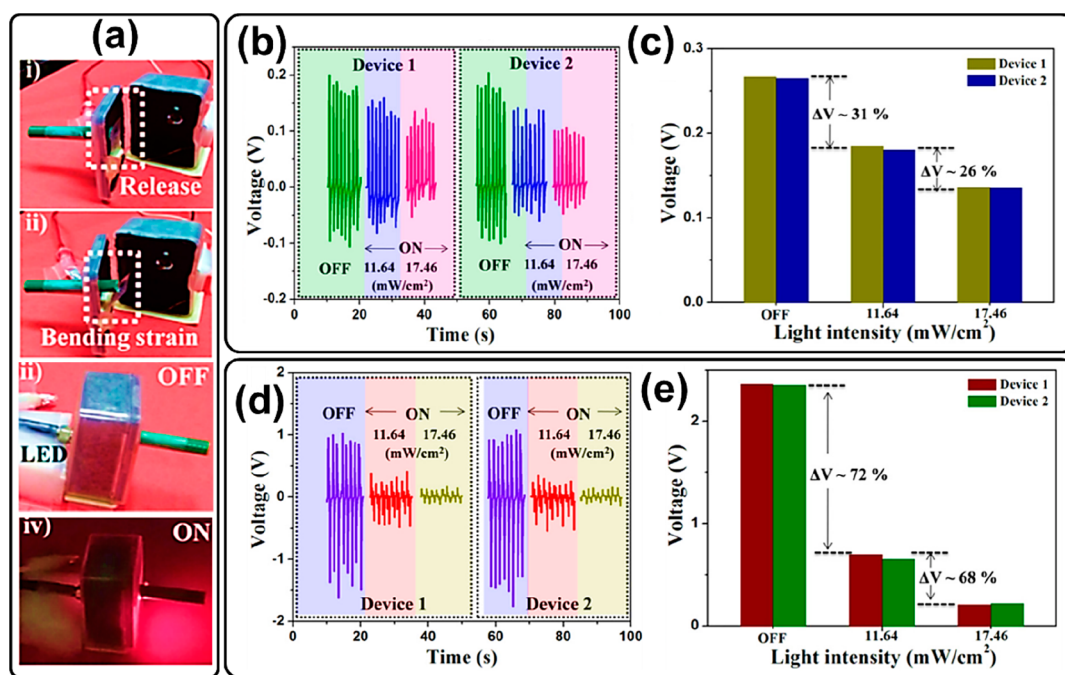
**Figure 18.** (a) Optical images of experimental set up used for applying bending force on a SbSI microrod (SMR)-based piezoelectric nanogenerator (PNG) in ON/OFF states. (b) Piezoelectric response and (c) corresponding deviation in piezoelectric voltage of SbSI/PMMA-based PNG. (d) Photoactive electrical response and (e) corresponding changes in the performance of SMR-PNG under ON/OFF conditions. (a−e) Reproduced with permission from ref 262. Copyright 2019 Elsevier.

Future research could perhaps focus on (1) theoretical and experimental understandings of the interaction between alkali ion transport and electrostatic forces in chalcohalides and (2) thorough investigations into topological defects and dopants in chalcohalides, both of which can significantly improve the overall performance of batteries and supercapacitors.

*5.2.4.2. Sb-Based Chalcohalides.* All solid-state batteries (ASSBs) hold the promise of next-generation high energy density and safe storage systems by using a solid-state electrolyte (SSE) and (ideally) a lithium metal anode.[286,287] Mixed-anion chemistry of chalcohalides is promising candidates as SSEs for LIBs, due to their high ionic conductivities and air stability. The first Sb-based argyrodites reported for use as an SSE for LIBs was a solid solute of $Li_{6+x}M_xSb_{1-x}S_5I$ (M = Si, Ge, Sn).[288] The substitution of $Si^{4+}$ onto the $Sb^{5+}$, and $Li^+$ into the lattice was significantly found to lower the activation energy barrier for Li-ion mobility, which was related to the slightly increased $S^{2-}/I^-$ site disorder but mostly to the disordered $Li^+$ distribution. It was also found that the additional $Li^+$ ion populates in new high energy lattice sites for $Li^+$ diffusion and activate concerted ion migration, leading to a low activation energy barrier. As a result, $Li_{6.6}Sb_{0.6}Sb_{0.4}S_5I$ exhibited a superionic conductivity, the highest reported to date, up to 24 mS $cm^{-1}$ for sintered pellets that enabled ASSB prototype with promising properties. Furthermore, first-principle calculations combined with experiments confirmed that the concerted Li-ion migration leads to high Li-ion diffusivity and thereby high ionic conductivity in the Si-rich $Li_{6.75}Sb_{0.25}Si_{0.75}S_5I$ SSE.[289] Similar observation was also reported in the case of Ge-substituted Sb-based argyrodites, $Li_{6.5}Sb_{0.5}Ge_{0.5}S_5I$ SSE, and was further confirmed using ab initio MD.[290] The $Li_{6.5}Sb_{0.5}Ge_{0.5}S_5I$ SSE showed good compatibility with ASSB using NCM523, after applying $Li_3YCl_6$ as a catholyte, demonstrating a high discharge density of 164 mAh $g^{-1}$ and good cycle stability.

This highlights the potential of chalcohalides as SSE in batteries, however, work on employing chalcohalides as anodes or cathodes in batteries is still limited. Understanding the specific structural features (e.g., reduced dimensionality), in our opinion, is an effective way to improve Li storage, given that the layered structure of chalcohalides has more areas accessible to accommodate more Li-ions. We postulate that chalcohalides, which have superior ionic mobility and a large surface area for charge storage, could effectively function as an alternative electrodes or electrolytes in batteries and supercapacitors.

**5.2.5. Thermoelectrics.** Thermoelectric (TE) generators, which can convert waste heat generated by home heating, automotive exhausts, and industrial processes to electricity, have become an area of attention for renewable energy sources.[291−294] Chalcohalides are expected to be promising TE materials owing to their low thermal conductivity and high carrier mobility; however, there are limited reports on TE properties of only Bi-based chalcohalides.[258,295−298] This section offers a brief review of progress in chalcohalide-based TE generators.

*5.2.5.1. Bi-Based Chalcohalides.* Sulfur/iodine flux system was used to synthesize $Bi_{13}S_{18}I_2$ and BiSI phases.[178] Bismuth was reacted in sulfur melts with varying amounts of iodine to investigate the effects of iodine concentration and reaction temperatures on phase production and purity. The authors reported the ability to control iodine concentration in the $S/I_2$ flux that allowed for the isolation of the metastable and difficult to synthesize phase of $Bi_{13}S_{18}I_2$. The experimental data showed the broad absorption edge around 0.82 eV, as well as a second slightly sharper absorption edge at ~0.90 eV. The results were in accordance with a theory that displayed the direct transitions along Γ occur at 0.76 and 0.91 eV, stating that this chalcohalide could be used in TE. Xu et al.[177] synthesized bulk polycrystalline and nanocrystalline $Bi_{13}S_{18}I_2$ by spark plasma sintering of commercial $Bi_2S_3$ and $BiI_3$, and by solution-phase method,

respectively, to study their TE properties. The maximum figure of merit (zTmax) of 1.0 was achieved at 788 K along the in-plane direction of nano $Bi_{13}S_{18}I_2$ + 2% $BiCl_3$ sample, whereas zTmax of 0.8 was obtained at 738 K along the cross-plane direction. The nanoundoped sample showed lower zTmax as compared to the doped sample in two directions. Bulk undoped $Bi_{13}S_{18}I_2$ showed the highest zTmax of 0.7 at 763 k. Although theoretical predications of TE properties of chalcohalides are promising, experimental investigation of their performance has only recently begun, necessitating additional effort to validate the intriguing theoretical predications. Low electrical conductivity in Bi-based chalcohalides hinders their further progress as TE materials. Improving their conductivity via self-doping or extrinsic dopants may improve their TE properties. Given the advancements in chalcogenide and halide perovskite as TE materials, we postulate that chalcohalides based on Sn, Pb, and Sb may be promising for TE applications; however, further theoretical and experimental investigations are required.

**5.2.6. Piezo/Pyro-electric Nanogenerators.** Over the last two decades, nanogenerators have emerged as promising energy conversion devices for transforming mechanical and thermal energy into electric power.[299,300] Based on their energy conversion mechanism, such as mechanical to electrical energy or thermal to electrical energy, these devices are classified as piezoelectric and pyroelectric nanogenerators, respectively.[301−303] Apart from exciting ferroelectric and optoelectronic properties of chalcohalides, Sb-based chalcohalides have interesting characteristics such as a pyroelectric coefficient of ~6 × $10^{-2}$ $Cm^{2-}$ $K^{-1}$ and piezoelectric coefficient of ~1 × $10^{-9}$ C/N ($d_{33}$) along with the highest known curie temperature of ~22 °C, making them promising candidates for piezo-/pyro-electric nanogenerators.

*5.2.6.1. Sb-Based Chalcohalides.* Purusothaman et al.[262] were the first to report the development of SbSI-based piezoelectric nanogenerators (PNGs) with different polymer matrix interfaces such as polydimethylsiloxane (PDMS), polyvinylidene fluoride (PVDF), and poly methyl methacrylate (PMMA). SbSI micro rods were synthesized using a facile and low-cost solid-state reaction at a temperature of 250 °C using commonly available raw materials. The authors first fabricated SbSI (1 wt%)/PMMA photodetector with metal−semiconductor−metal configuration to investigate the involvement of semiconducting and photoactive properties in mechanical energy harvester. The fabricated photodetector device demonstrated a responsivity of ~4.5 $\mu$A $W^{1-}$ and a response time (rising/falling time of 100/10 ms). This encouraged authors to further fabricate the PNGs based on SbSI/PMMA and SbSI microrods as active layers onto a cleaned indium tin oxide (ITO) substrate, followed by deposition of Ag electrode. The experimental setup used for applying external bending force onto the device in ON/OFF states is as shown in Figure 18a. When the light was off, SbSI-based PNG delivered an output voltage of ~2.4 V (Figure 18b), which was significantly larger than the SbSI/PMMA PNG (~0.26 V) (Figure 18c). Upon irradiation of the LED source of 630 nm, the piezoelectric voltage dropped gradually in both PNGs (Figure 18d). Notably, the SbSI-based PNG showed a high photoactive sensitivity with 72% and 68% changes in piezoelectric voltage (Δ$V$) than SbSI/PMMA based PNG, which showed Δ$V$ of 31% and 26% (Figure 18e). This high photoactive sensitivity in SbSI-based PNG is a result of a direct metal−semiconductor−metal interface in single SbSI micro rods, which was limited in SbSI/PMMA PNG by a dielectric PMMA medium. This work offers new insights

into the multifunctional properties of SbSI as semiconductor-photoactive-ferroelectric, which established a pathway to further explore these properties in harvesting mechanical energy toward the development of next-generation self-powered devices. Immediately after, Misterwicz et al.[263] demonstrated a simple, scalable, and cost-effective method to fabricate pyroelectric nanogenerator (PENG) based on sonochemically synthesized SbSeI nanowires and their high-pressure compression at RT to a bulk sample. The SbSeI PENG generated an output voltage of 12 mV, short-circuit current of 11 nA, pyroelectric energy harvesting figure of merit of 2.430(6) J $m^{-3}$ $K^{-2}$ and the maximum output power density of 0.59(4) $\mu$W/$m^2$. Although the output voltage and power density are significantly lower than the reported $BaTiO_3$ and $PbZrTiO_3$, the initial device performance is encouraging. The authors claimed that further improvements in the device performance can be achieved by decreasing the series resistance by increasing the compression pressure during the SbSeI PENG fabrication process and by aligning SbSeI nanowires perpendicular to electrodes to increase the energy harvesting efficiency. These early attempts on exploring the piezo- and pyroelectric nanogenerator applications of Sb-based chalcohalides are promising and could be further applied to other binary or ternary chalcohalide materials.

## 5.3. Synthesis and Applications of New Emerging Chalcohalides

**5.3.1. Transition/Post-transition and Mixed-Metals Chalcohalides.** *5.3.1.1. Pb-Based Chalcohalides.* The discovery of Pb-based chalcohalides began with the structural characterizations of stable $Pb_5S_2I_6$ and $Pb_7S_2Br_{10}$ chalcohalides from the PbS-PbBr$_2$ system and metastable $Pb_4SCl_6$ and $Pb_4SeBr_6$ chalcohalides from the PbS-PbCl$_2$ and PbSe-PbBr$_2$ systems.[78,102,183,304] The polycrystalline $Pb_7S_2Br_{10}$, $Pb_5S_2I_6$, $Pb_4SeBr_6$, and $Pb_3Te_5I_8$ materials were obtained by annealing stoichiometric amounts of the binary phases below the peritectic temperatures of 381, 418, 383, and 385 °C, respectively.[78] The band gap values of 1.6, 2, 2, and 2.5 eV were reported for $Pb_4SeBr_6$, $Pb_5S_2I_6$, $Pb_7S_2Br_{10}$, and $Pb_4SCl_6$, respectively. Although the synthesis and properties of such materials were unknown at the time, this earlier study served as a starting point for future investigations.

Ni et al.[182,184] synthesized bulk $Pb_4S_3I_2$ and $Pb_3Se_2Br_2$ using high-pressure solid-state reaction, and both materials indicated higher resistivity (>$10^8$ Ω cm) and indirect band gaps. Later, $Pb_3Se_2Br_2$ was synthesized through a high-pressure solid-state reaction by using PbBr$_2$, Pb powder and elemental Se shots at 700 °C for 3 h under 4 GPa pressure and then quenching the reaction at RT.[182] Noncentrosymmetric cubic crystal structure (*I43d*) was determined for $Pb_3Se_2Br_2$ with the small amounts of PbSe and PbBr$_2$ impurities. However, it confirmed to be a diamagnetic semiconductor with an experimentally determined indirect band gap of 1.48 eV. The $Pb_3Se_2Br_2$ material showed the dipole moment (one-unit cell) to be 1.73 × $10^{-28}$ Cm, and high resistivity (>$10^8$ Ω cm) at ambient temperature and pressure. The spontaneous polarization was calculated to be around 21 $\mu$C/$cm^2$ from DFT. Similar to $Pb_3Se_2Br_2$, $Pb_4S_3I_2$ was also synthesized from the reaction of a stoichiometric ratio of Pb, S and PbI$_2$ at 4 GPa and 600 °C for 3 h.[184] The material showed an orthorhombic crystal structure (*Pnma*) determined by XRD and an indirect band gap of ~1.6 eV from diffuse reflectance measurements, which was further confirmed by DFT calculations.
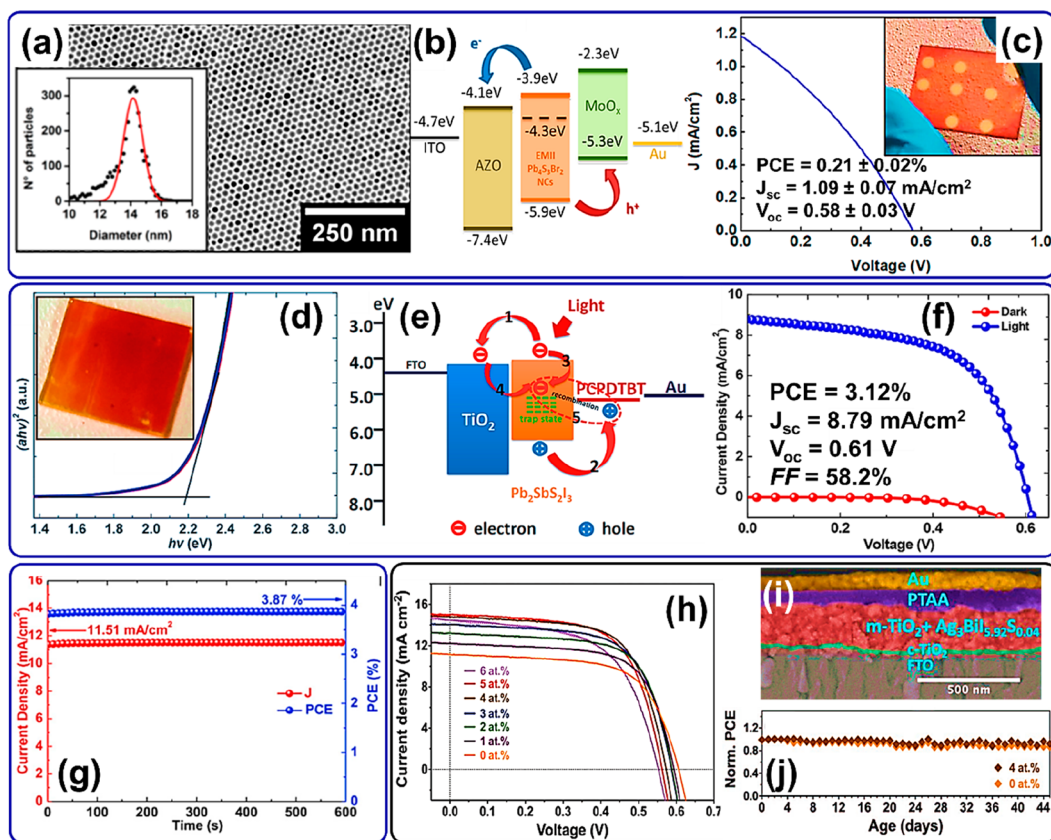
**Figure 19.** (a) TEM image of $Pb_4S_3Br_2$ NCs prepared at 180 °C. Inset shows the size distribution of $14.2 \pm 0.7$ nm. (b) Energy level alignment and (c) $J-V$ curve of the finished device with $ITO/AZO/Pb_4S_3Br_2/MoO_x/Au$ structure. The inset of (c) shows the digital photo of the representative device. (a−c) Reproduced with permission from ref 112. Copyright 2020 American Chemical Society. (d) Tauc plots of $Pb_2SbS_2I_3$ layers prepared at various concentrations of the $PbI_2$ solution on glass/mp-$TiO_2$ substrates. The inset of (d) shows the digital photo of $Pb_2SbS_2I_3$ thin film. (e) Schematic diagram of energy levels to describe the role of trap states and (f) $J-V$ curves in dark and under standard illumination conditions of the FTO/mp-$TiO_2/Pb_2SbS_2I_3/PCPDTBT/Au$ device. (d−f) Reproduced with permission from ref 305. Copyright 2018 American Chemical Society. (g) Photocurrent density and PCE of $Sn_2SbS_2I_3$ device obtained while holding the solar cells at their maximum voltage point (0.336 V). Reproduced with permission from ref 306. Copyright 2020 Cell Press. (h) $J-V$ curves of the Au/PTAA/$Ag_3BiI_{6-2x}S_x$ + m-$TiO_2/c$-$TiO_2$/FTO device with $x = 0$ to 6 at%. (i) Cross-sectional FE-SEM image of the Au/PTAA/$Ag_3BiI_{6-2x}S_x$ + m-$TiO_2/c$-$TiO_2$/FTO. (j) Normalized PCE of the Au/PTAA/$Ag_3BiI_{6-2x}S_x$ + m-$TiO_2/c$-$TiO_2$/FTO device with $x = 0$ and 4 at% stored in air under diffuse light. (h−j) Reproduced with permission from ref 110. Copyright 2018 John Wiley and Sons.

Further advances in the synthesis of the Pb-based chalcohalides were made with developing a colloidal synthetic approach for synthesizing $Pb_4S_3X_2$ (X = Cl, Br, I) NCs by Manna and co-workers.[112] A heat-up approach was developed in which the thermal decomposition of thiocyanate ($SCN^-$) ions (as a source of $S^{2-}$) was carried out in the presence of the corresponding $PbBr_2$, $PbI_2$, $PbCl_2$ precursors and OLA and OA solvents at a lower temperature (<190 °C). The $Pb_4S_3Br_2$ NCs showed a narrow size distribution and size tunability over the range ∼7 to 30 nm.[112] Indirect band gaps of 1.98, 1.76 and 2.02 eV were reported for $Pb_4S_3Br_2$, $Pb_4S_3I_2$ and $Pb_3S_2Cl_2$ NCs, respectively with the applicability of $Pb_4S_3Br_2$ in photodetector and solar cell. $Pb_4S_3I_2$ formed anisotropically exhibiting polydisperse and elongated rod type morphology with size ranging in hundreds of nm, whereas $Pb_3S_2Cl_2$ formed roughly spherical shaped NCs of ∼7.0 ± 0.8 nm (Figure 19a). The growth kinetics was studied by quenching aliquots of the reaction batch at different temperatures and surprisingly the optical absorption was found to be independent of the size of NCs. The absorption spectra of all materials were identical; however, there was a weak red-shift from chloride to bromide and subsequently to iodide-based NCs, resulting in slight

variation in band gap. The former two phases showed the orthorhombic crystal structure, whereas $Pb_3S_2Cl_2$ did not show resemblance to the orthorhombic, and resembled a pseudocubic structure, yet the coordination polyhedra for all three structures were quite similar. The energy alignment (Figure 19b) after the ligand exchange on the $Pb_4S_3Br_2$ NCs was studied to test its suitability to fabricate solar cell devices. The nonencapsulated solar cell device (Figure 19c, inset) with the configuration of $ITO/AZO/Pb_4S_3Br_2/MoOx/Au$ showed a PCE of 0.21 ± 0.02% with $J_{sc}$ of 1.09 mA/cm² and $V_{oc}$ of 0.58 V under standard AM1.5G illumination in the air (Figure 19c). Though the need for alternative energy materials to Pb-based compounds is of huge demand, this study demonstrates a pathway to further explore this class of chalcohalide materials that to date are untapped at the nanoscale.

The synthesis of quaternary $Pb_2SbS_2I_3$ material, an isostructural to $Sn_2SbS_2I_3$ was first reported by Dolgikh for their dielectric properties.[307] Later, Starosta et al.[308] synthesized ingots of $Pb_2SbS_2I_3$ materials by modifying the earlier reported Bridgman method. The weighed quantities of the stoichiometric elements Sb, Pb, S in quartz glass ampule were allowed to react with resublimed iodine at 650 °C for 36 h in the furnace. The as-

synthesized $Pb_2SbS_2I_3$ material showed band gap of 2.0 eV.[308] As explained in section 3, $Pb_2BiS_2I_3$, $Sn_2BiS_2I_3$, $Sn_2BiSI_5$, and $Pb_5S_2I_6$ possess the close relation in their structural properties, which form from infinite ribbon $[MS_2I_4]_m = \alpha$ (M = Sn, Pb, Bi) along the crystallographic c-axis. These materials show high electrical resistivities > 1 MΩ cm and experimental optical direct band gaps ranging between 1.2 and 1.6 eV, suitable for solar absorbers. These results are well accordance with theoretically results explained in section 4. After successfully demonstrating SbSI[147] and $Sb_{0.66}Bi_{0.33}SI$[234] solar cells, Seok and co-workers reported the first working device based on $Pb_2SbS_2I_3$ absorbers prepared using a two-step approach[305] based on their prior recipes.[147,234] A solution of $PbI_2$ in DMF (different concentrations 0.05, 0.10, and 0.20 mol/L) was spin coated on a chemical bath deposited $Sb_2S_3$ layers onto m-$TiO_2$, which was further subjected to annealing at 300 °C for 2 min. in Ar atmosphere to from $Pb_2SbS_2I_3$ absorbers. The as-prepared films showed a bandgap of ~2.19 eV (Figure 19d), correlating with its orange appearance of thin film. Solar cell devices based on $Pb_2SbS_2I_3$ absorbers, $TiO_2$ as ETL, and PCPDTBT as HTL were fabricated using standard device configuration and effect of $PbI_2$ solution concentration on the device performance was studied. The role of trap states was investigated to elucidate the mechanisms underlying the different recombination processes, which is shown in Figure 19e. Following their previous work for the further optimization, e.g., spin coating conditions, the thickness of m-$TiO_2$ and $Sb_2S_3$ deposition time, the PCE of ~3.12% with $J_{sc}$ of 8.79 mA/cm$^2$, $V_{oc}$ of 0.61 V, and FF of 58.2% (Figure 19f) was reported. The stability studies further demonstrated that irrespective of different stability conditions, devices retained ~90% of their initial performance, explaining the impressive stability of chalcohalide materials over Pb-halide perovskite materials. While promising, these results show a wide band gap and a low short-circuit current density from the multifaceted deposition method and yet there is still plenty of room for the thorough examination.

*5.3.1.2. Sn-Based Chalcohalides.* The first preparation of $Sn_2SbS_2I_3$ with orthorhombic structure (*Cmcm*) was reported by Oliver-Fourcade et al.[309] in 1980, owing to its significant semiconducting and ferroelectric properties.[310] Strarosta et al.[308] demonstrated the fabrication of $Sn_2SbS_2I_3$ single crystals using a modified Bridgman method almost a decade later, reporting exact lattice parameter values as well as band gap of 1.5 eV. Despite promising semiconducting properties and a suitable optical bandgap, the use of $Sn_2SbS_2I_3$ in energy devices remained unexplored until recently. Taking this into consideration, Seok and co-workers demonstrated a single-step solution process to prepare heteroleptic $Sn_2SbS_2I_3$ solar cells using $SbCl_3$-thiourea complex and $SnI_2$ solution with the first notable PCE of 4.04%.[306] Insufficient light absorption and charge transfer, and either too low or too high concentrations of $SbCl_3$ precursor solution were shown to lead poor device efficiency. The poor device efficiency (at a higher concentration of $SbCl_3$ precursor solution) is mainly caused by the higher trap density and deep level traps states. Notably, the uncapsulated devices demonstrated remarkable thermal and photostability as well as long-term stability when stored for 504 h, demonstrating high stability of $Sn_2SbS_2I_3$ material compared to the Sn-based halide perovskites. Recently, Kanatzidis and co-workers revisited Sn-based sulfoiodides and demonstrated the synthesis of new quaternary $Sn_2BiS_2I_3$ and $Sn_2BiSI_5$ materials using isothermal heating and chemical vapor transport methods.[109] Interestingly, these compounds are found to be stable in water and air, with

band gaps of 1.2−1.3 eV, making them promising for solar energy conversion applications, albeit no actual application has been demonstrated.

*5.3.1.3. Ag-Based Chalcohalides.* $Ag_3SI$ and $Ag_3SBr$ were first discovered by Reuter and Hardel in 1960,[311] while Takahashi and Yamamoto researched them in 1966, particularly for use as solid electrolytes due to their superionic conductivity.[312] However, costly synthesis and deposition methods hinder the development of silver chalcohalide for PV or other energy harvesting device applications.[311−314] Yet, due to their ecologically benign nature, chemical adaptability, and suitable band gap (0.9−1.1 eV), Ag-based chalcohalides look to be the most promising, which would make them interesting for single-junction solar cells as well low-band gap bottom cells in tandem configurations in the near future.[315,316] Consequently, different cation- or anion-replacements have been reported for $Ag_3SBr$. Silver iodobismuthates (Ag-Bi-I) materials have been emerged as potential absorber materials in PV owing to their high stability and direct band gaps of 1.85−1.90 eV that enable harvesting of a broader spectrum of solar radiation. A slightly wider band gap of these compounds than the ideal value of ~1.6 eV makes them unsuitable for single-junction solar cells; however, they can be an exciting alternate as top cells for silicon PV. On the other hand, the electronic structures of silver bismuth iodides and sulfides suggest a mixed anion structure, such as $Ag_aBi_bI_{a+3b−2x}S_x$ with a suitable band gap and energy position, could be an ideal candidate for high-efficiency solar cells. In this regard, Pai et al.[110] developed a new class of PV materials of silver bismuth sulfoiodide using well-established solution processing, easing the barriers of a wide band gap and a downshifted VBM. The effects of the partial anionic sulfide substitution in a range of silver bismuth iodides ($AgBiI_4$, $Ag_2BiI_5$, $Ag_3BiI_6$, and $AgBi_2I_7$) on their structure, optoelectronic properties and performance as light harvesters in solar cells were studied thoroughly. The solar cell device fabricated with the architecture of Au/PTAA/$Ag_3BiI_{6−2x}S_x$ + m-$TiO_2$/c-$TiO_2$/ FTO demonstrated an improved efficiency from 4.33 ± 0.05 to 5.44 ± 0.07% upon changing x from 0 to 4 at% (Figure 19h,i). $Ag_3BiI_{5.92}S_{0.04}$ based devices showed long-term stability and it retained more than 90% of their initial efficiency after 45 days of storage under ambient conditions (Figure 19j). While further combined theoretical and experimental efforts for optimal iodide-to-sulfide substitution, $V_{oc}$ and FF improvement are needed to understand the charge carrier dynamics at the interface.[110]

**5.3.2. Hybrid Organic−Inorganic Metal Chalcohalides.** Theoretical findings and relevant investigations motivate researchers to attempt with a stable and efficient chalcohalide perovskite, without ruling out the potential of generating the phase in nonequilibrium environments. The efforts have been made to synthesize $MASbSI_2$ chalcohalide perovskite by Nie et al.,[186] however, the authors did not reveal much on the formation mechanism and their optoelectronic properties. The $MASbSI_2$ was prepared via a two-step solution process that involved a spin coating followed by thermal annealing at low temperatures. The fabricated solar cell devices based on $MASbSI_2$ with FTO/BL-$TiO_2$/m-$TiO_2$)/$MASbSI_2$/HTM/Au configuration demonstrated the PCE of 3.08% (Figure 20a) and retained ~ 91% of the initial PCE after storing for 30 days. Following to this report, $MA_3Bi_2I_{9−2x}S_x$ based thin film with hexagonal structure ($P6_3/mmc$) was also fabricated by the low-pressure vapor-assisted solution process.[317] Resulting S-doped $MA_3Bi_2I_{9−2x}S_x$ film showed a band gap of 1.67 eV with a PCE of
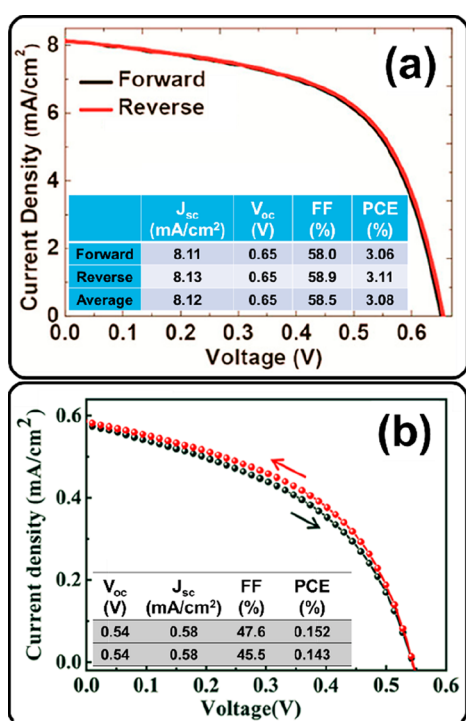
**Figure 20.** (a) *J−V* curves in forward- and reverse-scan modes of the best-performing of MASbSI₂. Reproduced with permission from ref 186. Copyright 2018 American Chemical Society. (b) *J−V* curves in forward- and reverse-scan modes of $MA_3Bi_2I_{9−2x}S_x$ devices. Reproduced with permission from ref 317. Copyright 2019 John Wiley and Sons.

0.15%, for $FTO/c\text{-}TiO_2/mes\text{-}TiO_2/MA_3Bi_2I_{9−2x}S_x/Spiro\text{-}OMeTAD/Au$ device configuration (Figure 20b). Further, MABiI₂S (MBIS) material was synthesized by a two-step solid-state reaction process and exhibited band gap of 1.52 eV with a wide absorption range that extends to over 1000 nm.[318] The fabricated device of $FTO/c\text{-}TiO_2/m\text{-}TiO_2/MBIS/PCPDTBT/Au$ configuration has shown the PCE up to 0.13% displaying high defect tolerance ability.

The performance of these chalcohalide materials-based solar cells is summarized in Table 5. As suggested by Yan and co-workers from combined theory and experimental approaches, these chalcohalide perovskites decomposes into secondary phases or phase segregate or form nonperovskite phases under thermal equilibrium conditions. Therefore, similar to prior studies on silver-bismuth compounds,[110] these materials are also considered as chalcogenide-doped metal halides rather than chalcohalides at this stage. We postulate that the synthesis of chalcohalide perovskites may be possible as metastable phases under nonequilibrium conditions using colloidal hot-injection or heat-up approaches; however, a careful choice of chalcogen and halogen precursor is highly necessary. Future research should focus on thorough understanding of their synthesis, reaction mechanism, phase formation with advanced characterizations, along with combined experimental and theoretical approaches.

## 6. SUMMARY AND FUTURE PERSPECTIVES

Overall, this review has greatly advanced the understanding of the emerging chalcohalide materials from both theoretical and experimental viewpoints. There has been substantial progress made in computational approaches for understanding their

structural, electrical, and optoelectronic properties. In the quest for alternative, highly stable and nontoxic materials with high defect tolerance ensued from its ns² electronic configuration, Bi- and Sb-based chalcohalide materials are being realized for a range of practical applications. In section 1, we introduced the emerging chalcohalide materials, and compared them to halide perovskites and chalcogenides. In section 2, we briefly introduced the efforts of computational and experimental designs to predict new chalcohalide semiconductor materials and investigate their fundamental structural and optoelectronic properties. Later, we focused on the materials properties allowing attributes toward energy conversion applications covering the most promising Bi- and Sb-based chalcohalides and a few new Cu-, Pb-, Sn-, Ag-, and chalcohalide perovskite-based materials. In section 3, we focused on their structural features and commented on their correlation with the optoelectronic properties. In section 4, we thoroughly summarized the progress made in the theoretical calculations of the band structures and predicting the electronic properties of these materials. And finally, in section 5, we reviewed the advances made in the synthesis of these chalcohalide materials and their promising results in energy conversion and storage devices. Most works have been aimed at utilizing the pnictogen chalcohalide materials for solar cells, photocatalysis, and photodetectors, and recently for batteries, supercapacitors, thermoelectrics, and piezo/pyro-electric nanogenerators. While the new transition and post-transition and mixed-metals chalcohalides (Pb-, Sn-, and Ag-based) have yet gained the interest for solar cells. It is reasonable to conclude that computational studies and experimental investigations are still required to realize their full potential in energy conversion and storage applications, which are still in their early stages.

In the following, we summarize some current challenges and future perspectives on computational and theoretical studies to understand the fundamental properties of existing chalcohalide materials and to discover new ones as well as next steps that can be taken to design and engineer these materials experimentally.

1. Fundamental properties and materials discovery. Advanced computational tools ranging from DFT calculations to machine learning can be used for investigating the structural, optical, and electronic properties of the previously synthesized chalcohalides in databases and to advance the screening process. Future research can be focused on developing novel materials based on structural analogies like halide perovskites and chalcogenides. The promising new stoichiometries and chemistries can be proposed through computational design (e.g., CsBiSI₂, CsSbSI₂, CsSnS₂Cl, and Cu₂ZnSI₂). Defining the distribution and degree of order−disorder of two or more anions is a unique challenge in these mixed-anion materials.[319] A range of structure-search algorithms, such as cluster expansions, specific quasirandom structures, and genetic algorithms, which are often employed in multicomponent alloys and single-anion compounds, could be utilized to analyze phase stability and solve structures in these chalcohalide compounds.[319−322]

2. Defects, dopants, and synthesizability. Only a few attempts have been made to understand the dopants, defects, and synthesizability of these chalcohalide materials through computational screening. Recent advances in high throughput computational screening offer new tools (e.g., PyCDT, PyLADA) to facilitate the

**Table 5. Summarized Reports of Other (Pb-, Ag-, Sn-, and Perovskite-Based) Chalcohalide Materials in Different Energy Device Applications**

| material | deposition | reaction conditions | band gaps (eV) | device structure / measurement conditions | performance |
|---|---|---|---|---|---|
| Pb$_2$SbS$_2$I$_3$[305] | chemical bath + spin coating | step 1 Sb$_2$S$_3$: sodium thiosulfate in water + SbCl$_3$ in acetone + water: reaction at 10 °C, + annealing in Ar atm at 300 °C for 5 min; step 2 SbSI: PbI$_3$ in DMF spin coated at 500−2000 rpm for 60 s on Sb$_2$S$_3$, annealing in Ar atm at 300 °C for 2 min | 2.19 | FTO/BL-TiO$_2$/mp-TiO$_2$/Pb$_2$SbS$_2$I$_3$/PCPDTBT/Au | $J_{sc}$ = 8.79 mA/cm$^2$; $V_{oc}$ = 0.61 V; FF = 58.2%; PCE = 3.12% |
| Pb$_3$S$_2$X$_2$ (X = Cl, Br, I)[112] | colloidal heat-up | PbX$_2$ (X = Cl, Br, I) and Pb(SCN)$_2$ in ODE + OLA + OA, reaction at 130 to 170 °C for 1 h | 1.76 (Pb$_3$S$_2$I$_2$), 1.98 (Pb$_3$S$_2$Br$_2$), 2.02 (Pb$_3$S$_2$Cl$_2$) | ITO/AZO/Pb$_3$S$_2$Br$_2$/MoO$_x$/Au | $J_{sc}$ = 1.2 mA/cm$^2$; $V_{oc}$ = 0.57 V; PCE = 0.21% |
| Ag$_a$Bi$_b$I$_{a+3b-2x}$S$_x$[110] | spin coating | AgI + BiI$_3$ + Bi(S$_2$CAr)$_3$ in DMSO:DMF:HI (3:1 v/v) spin-coated at 1000 rpm for 10 s followed by 4000 rpm for 30 s, annealing at 130 °C for 15 min. in an N$_2$-filled glovebox | 1.76−1.87 (direct) | FTO/c-TiO$_2$/m-TiO$_2$/Ag$_3$BiI$_{5.92}$S$_{0.04}$/PTAA/Au | $J_{sc}$ = 14.7 mA/cm$^2$; $V_{oc}$ = ~0.57 V; FF = 65.9%; PCE = 5.56% |
| Sn$_2$SbS$_2$I$_3$[306] | spin coating | SbCl$_3$, thiourea, and SnI$_2$ in DMF spin-coated at 1000−2000 rpm for 1 min, annealing at 300 °C for 5 min in Ar atm | 1.41 | FTO/BL-TiO$_2$/mp-TiO$_2$/Sn$_2$SbS$_2$I$_3$/PCPDTBT/PEDOT:PSS/Au | $J_{sc}$ = 16.1 mA/cm$^2$; $V_{oc}$ = 0.44 V; FF = 57%; PCE = 4.04% |
| MASbSI$_2$[186] | chemical bath + spin coating | step 1 Sb$_2$S$_3$: sodium thiosulfate in water + SbCl$_3$ in acetone + water, reaction at 10 °C, annealing in Ar atm at 300 °C for 5 min; step 2 SbSI: SbI$_3$ in DMF spin coated on Sb$_2$S$_3$, annealing at 150 °C for 5 min in an inert atm; step 3: MAI in 2-propanol; spin-coated on SbSI, annealing at 150 °C for 5 min in Ar atm | 2.03 | FTO/c-TiO$_2$/mp-TiO$_2$/MASbSI$_2$/PCPDTBT/PEDOT:PSS /Au | $J_{sc}$ = 8.13 mA/cm$^2$; $V_{oc}$ = 0.65 V; FF = 58.9%; PCE = 3.11% |

defect calculations in the materials. More defects calculations of these materials are much needed to understand their physical properties and potential in future applications. Utilizing advanced theoretical and computational screening to understand the stability, degradation, and defect tolerance in chalcohalide materials is essential to demonstrate the material's ability in energy conversion devices.

3. Investigation on the band gap and optical properties. The most of the chalcohalide materials showed the indirect band gap, with few demonstrating minor differences in their direct and indirect band gaps. According to a few observations, this discrepancy can result in higher optical absorption because carriers are thermalized to valleys with varying electron velocities, resulting in a high degeneracy of bands and low electron–hole recombination.[197,323] The findings that have been revealed so far neither completely demonstrate the existence of a direct band gap nor do they completely invalidate it. In fact, indirect band gap materials can be just as effective as direct band gap materials if the minority carrier diffusion length is greater than the absorption length.

   Due to the frequent consideration of many of these indirect band gap materials in optoelectronics and energy harvesting devices, the indirect to direct band gap transition may receive more attention. This would be accomplished by applying several previously reported strategies, and the significant aspect is to identify suitable approaches to greatly enhance optical transitions at the band gap without compromising materials inherent properties.[324] For example, careful nanostructuring and surface engineering could result in considerable intervalley mixing in the CBM, which positively impacted optical transitions at the band edge.[324] Studying strain engineering and the stabilization of metastable crystalline phases might even lead to favorable optical transitions.[325−328] Additionally, it might be achieved by changing from ordered to disordered material (antisite defect), such as by disordering the cations in its sublattice.[329,330]

4. Band offset and alignments. Only a portion of these materials have been studied for their band offset and alignments, and the majority of them remain unexplored from a device design point of view; such studies are also important to facilitate their applications in solar water splitting and solar cell. This can be realized experimentally by synthesizing the heterojunctions such as SbSI/SbSBr and measuring their interfacial band offset. We postulate that designing new device architectures using these chalcohalide materials and incorporating both *n*-type and *p*-type chalcohalide materials into existing devices can lead to high-performing solar water splitting and solar cells devices.

5. Experimental investigations. The continued research into combining Bi- and Sb-based chalcohalides with complementary properties (section 2) to achieve the desired device functionality will be beneficial. This includes the continued exploration of anion and cation alloying in these materials such as doping/substituting A site cations with MA, FA, Cs, Rb, Cu, Ge, etc. and anions such as Se, Te, I, Br, and Cl to realize their full potential at device level. As discussed previously in this review, as exemplified by the halide perovskites and chalcogenide materials,

many materials breakthroughs can be achieved by tuning the properties. Anionic distribution and composition, as well as local structures, and their tuning need to be studied using advanced analytical techniques such as X-ray and neutron scattering, in situ and operando techniques, electron energy loss spectroscopy (EELS) combined with scanning transmission electron microscopy (STEM), X-ray absorption near edge structure (XANES) of X-ray absorption spectroscopy, and magic angle-spinning (MAS) nuclear magnetic resonance (NMR).[319,331,332]

6. New synthesis methods and postprocessing. Most of the previous reports have been focused on growing large crystals of Bi- and Sb-based chalcohalides using sonochemical, hydrothermal, solvothermal methods, etc., and very few are focused on direct thin film formation that has a great potential in solar energy conversion device implications. Those works mostly rely on two-step methods (except for BiSI and $AgBiS_xI_{1−x}$) due to competitive chemistry between chalcogen and halogen anions. These multistep processes usually result in nonuniform microstructure, affecting the charge transport properties. New processing techniques such as one-step solution processing, vapor transport method, as well as nonequilibrium synthesis methods (such as hot-injection or heating approach) and postprocessing for high-quality materials that will be used to promote charge transport and controlled doping/alloying in chalcohalide materials.

7. Device engineering. Device engineering is a key step in fabricating high-performance energy devices. The main intention of this review is to demonstrate the potential of these promising materials in solar energy conversion devices. Most of the reported solar cell devices based on chalcohalide materials are still focused on using the dye-sensitized device architecture. A thorough understanding of their electrical properties, band structure and alignments is needed to design a suitable device architecture. We suggest adopting planer device structures with a focus on utilizing different ETM (such as $SnO_2$, ZnO, MgZnO, NiO, etc.) and HTMs (e.g., P3HT, spiro-OMeTAD, PTAA, etc.). For example, as mentioned previously in section 5, SbSbr has good band structure alignment like CZTS materials. Therefore, solid-state thin-film solar cells device structure could also be tested for these chalcohalide materials.

8. Perspective of future applications. (i) Light-emitting devices. With highly tunable optical properties (by alloying chalcogen and halogen anions) and defect tolerance, chalcohalide materials should also be an ideal light emitter. So far, no LED devices based on chalcohalide materials have been demonstrated, emphasizing the importance of focusing on synthesis methodologies and knowledge on the structural defects in these materials. An in-depth understanding of the origin of nonradiative recombination in PL emission must be achieved to realize the potential of these materials in LEDs. Future efforts should be devoted to the fundamental understanding of PL emission using computational screening and advanced optical characterizations. (ii) Solar fuels for energy storage. It has been proposed and experimentally demonstrated that the chalcohalide materials are air and moisture stable, which suggests their future deployment in devices producing solar fuels. We postulate that chalcohalides could

effectively serve as either photoanode or photocathode taking advantage of their structural and optoelectronic properties analogues to halide perovskites with the additional benefits of high stability.

Furthermore, the dimensionality and structures of chalcohalide materials are a less explored but efficient way of studying their anisotropic properties. Since anisotropic nanostructures have been shown to have higher light-harvesting efficiency than simple, isotropic building blocks, it would involve a range of possible combinations in order to ensure chalcohalide materials. Therefore, anisotropic chalcohalides, which comprise various compositions, phases, shapes, and sizes, hold great promise for future photonics, catalysis, sensing, biomedical, and energy technologies. The chemistry of the $ns^2$ lone pair led to the revealed properties (section 2), but the explanations provided elsewhere are unclear, making it difficult to establish a comprehensive understanding of these materials that would allow the development of effective optoelectronic devices. As a result, many of such questions warrant more research in order to comprehend the structure−property correlations and reveal their realistic possibilities.

This review motivates the continued research into investigating the fundamental properties of chalcohalide materials and their further energy applications. The insights gained in these studies will surely contribute to a greater understanding of using an ionic-covalent mixed-framework for exploratory surveys of chemical systems. We envision that the future advances into materials containing mixed chalcogen and halogen anions and devices based on the suite of these materials can be a key in realizing an alternative robust, cost-effective, and nontoxic family of materials for the imminent high-performance energy storage and conversion. Knowing the underlying science and then selecting promising technologies, these materials can be developed to better comprehend the existing impediments.

## AUTHOR INFORMATION

### Corresponding Author

**Mahesh P. Suryawanshi** − *School of Photovoltaic and Renewable Energy Engineering, University of New South Wales, Sydney, New South Wales 2052, Australia;* ⊙ orcid.org/0000-0003-4711-7655; Email: m.suryawanshi@unsw.edu.au

### Authors

**Uma V. Ghorpade** − *Department of Chemical Sciences and Bernal Institute, University of Limerick, Limerick V94 T9PX, Ireland; School of Photovoltaic and Renewable Energy Engineering, University of New South Wales, Sydney, New South Wales 2052, Australia;* ⊙ orcid.org/0000-0001-8631-7030

**Martin A. Green** − *School of Photovoltaic and Renewable Energy Engineering, University of New South Wales, Sydney, New South Wales 2052, Australia;* ⊙ orcid.org/0000-0002-8860-396X

**Tom Wu** − *School of Materials Science and Engineering, University of New South Wales, Sydney, New South Wales 2052, Australia;* ⊙ orcid.org/0000-0003-0845-4827

**Xiaojing Hao** − *School of Photovoltaic and Renewable Energy Engineering, University of New South Wales, Sydney, New South Wales 2052, Australia;* ⊙ orcid.org/0000-0001-5903-4481

**Kevin M. Ryan** − *Department of Chemical Sciences and Bernal Institute, University of Limerick, Limerick V94 T9PX, Ireland;* ⊙ orcid.org/0000-0003-3670-8505

Complete contact information is available at:
https://pubs.acs.org/10.1021/acs.chemrev.2c00422

## REFERENCES

(1) Green, M. A. How Did Solar Cells Get So Cheap? *Joule* **2019**, 3, 631−633.

(2) Green, M. A. Commercial Progress and Challenges for Photovoltaics. *Nat. Energy* **2016**, 1, 15015.

(3) Green, M. A.; Bremner, S. P. Energy Conversion Approaches and Materials for High-Efficiency Photovoltaics. *Nat. Mater.* **2017**, 16, 23−34.

(4) *Photovoltaic Research: Best Research-Cell Efficiency Chart*; NREL, 2022. https://www.nrel.gov/pv/cell-efficiency.html (accessed 10-20-2022).

(5) Green, M. A.; Dunlop, E. D.; Hohl-Ebinger, J.; Yoshita, M.; Kopidakis, N.; Hao, X. Solar Cell Efficiency Tables (Version 58). *Prog. Photovolt.* **2021**, 29, 657−667.

(6) *First Solar Achieves Yet Another Cell Conversion Efficiency World Record*; First Solar, Inc., 2016. https://investor.firstsolar.com/news/press-release-details/2016/First-Solar-Achieves-Yet-Another-Cell-Conversion-Efficiency-World-Record/default.aspx (accessed 10-20-2022).

(7) Nakamura, M.; Yamaguchi, K.; Kimoto, Y.; Yasaki, Y.; Kato, T.; Sugimoto, H. Cd-Free Cu(In,Ga)(Se,S)$_2$ Thin-Film Solar Cell With Record Efficiency of 23.35%. *IEEE J. Photovolt.* **2019**, 9, 1863−1867.

(8) Geisz, J. F.; France, R. M.; Schulte, K. L.; Steiner, M. A.; Norman, A. G.; Guthrey, H. L.; Young, M. R.; Song, T.; Moriarty, T. Six-Junction III-V Solar Cells with 47.1% Conversion Efficiency Under 143 Suns Concentration. *Nat. Energy* **2020**, 5, 326−335.

(9) Grimme, S.; Antony, J.; Ehrlich, S.; Krieg, H. A Consistent and Accurate Ab Initio Parametrization of Density Functional Dispersion Correction (DFT-D) for the 94 Elements. H-Pu. *J. Chem. Phys.* **2010**, 132 (154104), 1−19.

(10) Suryawanshi, M. P.; Agawane, G. L.; Bhosale, S. M.; Shin, S. W.; Patil, P. S.; Kim, J. H.; Moholkar, A. V. CZTS Based Thin Film Solar Cells: A Status Review. *Mater. Tech.* **2013**, 28, 98−109.

(11) Zhou, H.; Hsu, W.-C.; Duan, H. S.; Bob, B.; Yang, W.; Song, T. B.; Hsu, C.-J.; Yang, Y. CZTS Nanocrystals: A Promising Approach for Next Generation Thin Film Photovoltaics. *Energy Environ. Sci.* **2013**, *6*, 2822−2838.

(12) Ghorpade, U.; Suryawanshi, M.; Shin, S. W.; Gurav, K.; Patil, P.; Pawar, S.; Hong, C. W.; Kim, J. H.; Kolekar, S. Towards Environmentally Benign Approaches for the Synthesis of CZTSSe Nanocrystals by a Hot Injection Method: A Status Review. *Chem. Commun.* **2014**, *50*, 11258−11273.

(13) Kumar, M.; Dubey, A.; Adhikari, N.; Venkatesan, S.; Qiao, Q. Strategic Review of Secondary Phases, Defects and Defect-Complexes in Kesterite CZTSSe Solar Cells. *Energy Environ. Sci.* **2015**, *8*, 3134−3159.

(14) Giraldo, S.; Jehl, Z.; Placidi, M.; Izquierdo-Roca, V.; Perez-Rodriguez, A.; Saucedo, E. Progress and Perspectives of Thin Film Kesterite Photovoltaic Technology: A Critical Review. *Adv. Mater.* **2019**, *31*, No. e1806692.

(15) Hadke, S.; Huang, M.; Chen, C.; Tay, Y. F.; Chen, S.; Tang, J.; Wong, L. Emerging Chalcogenide Thin Films for Solar Energy Harvesting Devices. *Chem. Rev.* **2022**, *122*, 10170−10265.

(16) Li, J.; Wang, D.; Li, X.; Zeng, Y.; Zhang, Y. Cation Substitution in Earth-Abundant Kesterite Photovoltaic Materials. *Adv. Sci.* **2018**, *5*, No. e1700744.

(17) Scragg, J. J.; Ericson, T.; Kubart, T.; Edoff, M.; Platzer-Björkman, C. Chemical Insights into the Instability of $Cu_2ZnSnS_4$ Films During Annealing. *Chem. Mater.* **2011**, *23*, 4625−4633.

(18) Ramanujam, J.; Bishop, D. M.; Todorov, T. K.; Gunawan, O.; Rath, J.; Nekovei, R.; Artegiani, E.; Romeo, A. Flexible CIGS, CdTe and a-Si:H based thin film solar cells: A Review. *Prog. Mater Sci.* **2020**, *110*, 100619.

(19) Green, M. A.; Ho-Baillie, A.; Snaith, H. J. The Emergence of Perovskite Solar Cells. *Nat. Photonics* **2014**, *8*, 506−514.

(20) Akkerman, Q. A.; Raino, G.; Kovalenko, M. V.; Manna, L. Genesis, Challenges And Opportunities for Colloidal Lead Halide Perovskite Nanocrystals. *Nat. Mater.* **2018**, *17*, 394−405.

(21) Yin, W. J.; Yang, J.-H.; Kang, J.; Yan, Y.; Wei, S.-H. Halide Perovskite Materials for Solar Cells: A Theoretical Review. *J. Mater. Chem. A* **2015**, *3*, 8926−8942.

(22) Jena, A. K.; Kulkarni, A.; Miyasaka, T. Halide Perovskite Photovoltaics: Background, Status, and Future Prospects. *Chem. Rev.* **2019**, *119*, 3036−3103.

(23) Fu, Y.; Zhu, H.; Chen, J.; Hautzinger, M. P.; Zhu, X. Y.; Jin, S. Metal Halide Perovskite Nanostructures for Optoelectronic Applications and the Study of Physical Properties. *Nat. Rev. Mater.* **2019**, *4*, 169−188.

(24) Stranks, S. D.; Snaith, H. J. Metal-Halide Perovskites for Photovoltaic and Light-Emitting Devices. *Nat. Nanotechnol.* **2015**, *10*, 391−402.

(25) Snaith, H. J. Perovskites: The Emergence of a New Era for Low-Cost, High-Efficiency Solar Cells. *J. Phy. Chem. Lett.* **2013**, *4*, 3623−3630.

(26) Snaith, H. J. Present Status and Future Prospects Of Perovskite Photovoltaics. *Nat. Mater.* **2018**, *17*, 372−376.

(27) Correa-Baena, J.; Saliba, M.; Buonassisi, T.; Grätzel, M.; Abate, A.; Tress, W.; Hagfeldt, A. Promises and Challenges of Perovskite Solar Cells. *Science* **2017**, *358*, 739−744.

(28) Min, H.; Lee, D. Y.; Kim, J.; Kim, G.; Lee, K. S.; Kim, J.; Paik, M. J.; Kim, Y. K.; Kim, K. S.; Kim, M. G.; et al. Perovskite Solar Cells with Atomically Coherent Interlayers on SnO2 Electrodes. *Nature* **2021**, *598*, 444−450.

(29) Babayigit, A.; Duy Thanh, D.; Ethirajan, A.; Manca, J.; Muller, M.; Boyen, H. G.; Conings, B. Assessing the Toxicity of Pb- and Sn-Based Perovskite Solar Cells in Model Organism Danio Rerio. *Sci. Rep.* **2016**, *6*, 18721.

(30) Savory, C. N.; Walsh, A.; Scanlon, D. O. Can Pb-Free Halide Double Perovskites Support High-Efficiency Solar Cells? *ACS Energy Lett.* **2016**, *1*, 949−955.

(31) Xiang, W.; Tress, W. Review on Recent Progress of All-Inorganic Metal Halide Perovskites and Solar Cells. *Adv. Mater.* **2019**, *31*, No. e1902851.

(32) Babayigit, A.; Ethirajan, A.; Muller, M.; Conings, B. Toxicity of Organometal Halide Perovskite Solar Cells. *Nat. Mater.* **2016**, *15*, 247−251.

(33) Rong, Y. G.; Hu, Y.; Mei, A. Y.; Tan, H. R.; Saidaminov, M. I.; Seok, S. I.; McGehee, M. D.; Sargent, E. H.; Han, H. W. Challenges for Commercializing Perovskite Solar Cells. *Science* **2018**, *361*, No. eaat8235.

(34) Correa-Baena, J. P.; Saliba, M.; Buonassisi, T.; Gratzel, M.; Abate, A.; Tress, W.; Hagfeldt, A. Promises and Challenges of Perovskite Solar Cells. *Science* **2017**, *358*, 739−744.

(35) Turkevych, I.; Kazaoui, S.; Ito, E.; Urano, T.; Yamada, K.; Tomiyasu, H.; Yamagishi, H.; Kondo, M.; Aramaki, S. Photovoltaic Rudorffites: Lead-Free Silver Bismuth Halides Alternative to Hybrid Lead Halide Perovskites. *ChemSusChem* **2017**, *10*, 3754−3759.

(36) *Lead poisoning*; World Health Organization, 2022. https://www.who.int/news-room/fact-sheets/detail/lead-poisoning-and-health (accessed 10-20-2022).

(37) Zhang, D.; Li, D.; Hu, Y.; Mei, A.; Han, H. Degradation Pathways In Perovskite Solar Cells and How to Meet International Standards. *Commun. Mater.* **2022**, *3*, 1−14.

(38) Zhao, Y.; Ma, F.; Qu, Z.; Yu, S; Shen, T.; Deng, H.; Chu, X.; Peng, X.; Yuan, Y.; Zhang, X.; You, J. Inactive $(PbI_2)_2RbCl$ Stabilizes Perovskite Films for Efficient Solar Cell. *Science* **2022**, *377*, 531−534.

(39) Luther, J. M.; Schelhas, L. T. Perovskite Solar Cells Can Take The Heat. *Science* **2022**, *376*, 28−29.

(40) Chen, S. S.; Dai, X. Z.; Xu, S.; Jiao, H. Y.; Zhao, L.; Huang, J. S. Stabilizing Perovskite-Substrate Interfaces for High-Performance Perovskite Modules. *Science* **2021**, *373*, 902−907.

(41) Jiang, Q.; Tong, J.; Xian, Y.; Kerner, R. A.; Dunfield, S. P.; Xiao, C.; Scheidt, R. A.; Kuciauskas, D.; Wang, X.; Hautzinger, M. P.; et al. Surface Reaction For Efficient and Stable Inverted Perovskite Solar Cells. *Nature* **2022**, DOI: 10.1038/s41586-022-05268-x.

(42) Boyd, C. C.; Cheacharoen, R.; Leijtens, T.; McGehee, M. D. Understanding Degradation Mechanisms and Improving Stability of Perovskite Photovoltaics. *Chem. Rev.* **2019**, *119*, 3418−3451.

(43) Saparov, B.; Sun, J.-P.; Meng, W.; Xiao, Z.; Duan, H.-S.; Gunawan, O.; Shin, D.; Hill, I. G.; Yan, Y.; Mitzi, D. B. Thin-Film Deposition and Characterization of a Sn-Deficient Perovskite Derivative $Cs_2SnI_6$. *Chem. Mater.* **2016**, *28*, 2315−2322.

(44) Konstantakou, M.; Stergiopoulos, T. A Critical Review on Tin Halide Perovskite Solar Cells. *J. Mater. Chem. A* **2017**, *5*, 11518−11549.

(45) Li, W.; Wang, Z.; Deschler, F.; Gao, S.; Friend, R. H.; Cheetham, A. K. Chemically Diverse and Multifunctional Hybrid Organic-Inorganic Perovskites. *Nat. Rev. Mater.* **2017**, *2*, 16099.

(46) Li, M.; Li, F.; Gong, J.; Zhang, T.; Gao, F.; Zhang, W.-H.; Liu, M. Advances in Tin(II)-Based Perovskite Solar Cells: From Material Physics to Device Performance. *Small Struct.* **2022**, *3*, 2100102.

(47) Sun, N.; Gao, W.; Dong, H.; Liu, Y.; Liu, X.; Wu, Z.; Song, L.; Ran, C.; Chen, Y. Architecture of p-i-n Sn-Based Perovskite Solar Cells: Characteristics, Advances, and Perspectives. *ACS Energy Lett.* **2021**, *6*, 2863−2875.

(48) Yang, W. F.; Igbari, F.; Lou, Y. H.; Wang, Z. K.; Liao, L. S. Tin Halide Perovskites: Progress and Challenges. *Adv. Energy Mater.* **2020**, *10*, 1902584.

(49) Ke, W.; Stoumpos, C. C.; Kanatzidis, M. G. "Unleaded" Perovskites: Status Quo and Future Prospects of Tin-Based Perovskite Solar Cells. *Adv. Mater.* **2019**, *31*, No. e1803230.

(50) Stoumpos, C. C.; Frazer, L.; Clark, D. J.; Kim, Y. S.; Rhim, S. H.; Freeman, A. J.; Ketterson, J. B.; Jang, J. I.; Kanatzidis, M. G. Hybrid Germanium Iodide Perovskite Semiconductors: Active Lone Pairs, Structural Distortions, Direct And Indirect Energy Gaps, and Strong Nonlinear Optical Properties. *J. Am. Chem. Soc.* **2015**, *137*, 6804−6819.

(51) Stoumpos, C. C.; Malliakas, C. D.; Kanatzidis, M. G. Semiconducting Tin And Lead Iodide Perovskites with Organic Cations: Phase Transitions, High Mobilities, and Near-Infrared Photoluminescent Properties. *Inorg. Chem.* **2013**, *52*, 9019−9038.

(52) Ke, W.; Kanatzidis, M. G. Prospects For Low-Toxicity Lead-Free Perovskite Solar Cells. *Nat. Commun.* **2019**, *10*, 965.

(53) Hu, H.; Dong, B.; Zhang, W. Low-Toxic Metal Halide Perovskites: Opportunities and Future Challenges. *J. Mater. Chem. A* **2017**, *5*, 11436−11459.

(54) Liang, L.; Gao, P. Lead-Free Hybrid Perovskite Absorbers for Viable Application: Can We Eat the Cake and Have It too? *Adv Sci.* **2018**, *5*, 1700331.

(55) Park, B. W.; Philippe, B.; Zhang, X.; Rensmo, H.; Boschloo, G.; Johansson, E. M. Bismuth Based Hybrid Perovskites $A_3Bi_2I_9$ (A: Methylammonium or Cesium) for Solar Cell Application. *Adv. Mater.* **2015**, *27*, 6806−6813.

(56) Saparov, B.; Hong, F.; Sun, J.-P.; Duan, H.-S.; Meng, W.; Cameron, S.; Hill, I. G.; Yan, Y.; Mitzi, D. B. Thin-Film Preparation and Characterization of $Cs_3Sb_2I_9$: A Lead-Free Layered Perovskite Semiconductor. *Chem. Mater.* **2015**, *27*, 5622−5632.

(57) McClure, E. T.; Ball, M. R.; Windl, W.; Woodward, P. M. $Cs_2AgBiX_6$ (X = Br, Cl): New Visible Light Absorbing, Lead-Free Halide Perovskite Semiconductors. *Chem. Mater.* **2016**, *28*, 1348−1354.

(58) Slavney, A. H.; Hu, T.; Lindenberg, A. M.; Karunadasa, H. I. A Bismuth-Halide Double Perovskite with Long Carrier Recombination Lifetime for Photovoltaic Applications. *J. Am. Chem. Soc.* **2016**, *138*, 2138−2141.

(59) Boopathi, K. M.; Karuppuswamy, P.; Singh, A.; Hanmandlu, C.; Lin, L.; Abbas, S. A.; Chang, C. C.; Wang, P. C.; Li, G.; Chu, C. W. Solution-Processable Antimony-Based Light-Absorbing Materials Beyond Lead Halide Perovskites. *J. Mater. Chem. A* **2017**, *5*, 20843−20850.

(60) Hu, W.; He, X.; Fang, Z.; Lian, W.; Shang, Y.; Li, X.; Zhou, W.; Zhang, M.; Chen, T.; Lu, Y.; et al. Bulk Heterojunction Gifts Bismuth-Based Lead-Free Perovskite Solar Cells with Record Efficiency. *Nano Energy* **2020**, *68*, 104362.

(61) Shi, Z.; Guo, J.; Chen, Y.; Li, Q.; Pan, Y.; Zhang, H.; Xia, Y.; Huang, W. Lead-Free Organic-Inorganic Hybrid Perovskites for Photovoltaic Applications: Recent Advances and Perspectives. *Adv. Mater.* **2017**, *29*, 1605005.

(62) Jin, Z.; Zhang, Z.; Xiu, J.; Song, H.; Gatti, T.; He, Z. A Critical Review on Bismuth and Antimony Halide Based Perovskites and Their Derivatives for Photovoltaic Applications: Recent Advances and Challenges. *J. Mater. Chem. A* **2020**, *8*, 16166−16188.

(63) Filip, M. R.; Liu, X.; Miglio, A.; Hautier, G.; Giustino, F. Phase Diagrams and Stability of Lead-Free Halide Double Perovskites Cs2BB′X6: B = Sb and Bi, B′ = Cu, Ag, and Au, and X = Cl, Br, and I. *J. Phy. Chem. C* **2018**, *122*, 158−170.

(64) Fridkin, F. M.; Gerzanich, E. I.; Groshik, I. I.; Lyakhovitskaya, V. A. Absorption Edge in the Semiconducting Ferroelectrics SbSBr, BiSBr, SbSI. *JETP Lett.* **1966**, *4*, 201−205.

(65) Harbeke, G. Absorption Edge on Ferroelectric SbSi under Electric Fields. *J. Phys. Chem. Solids* **1963**, *24*, 957−963.

(66) Starczewska, A.; Nowak, M.; Szperlich, P.; Bednarczyk, I.; Mistewicz, K.; Kepinska, M.; Duka, P. Antimony Sulfoiodide as Novel Material for Photonic Crystals. *Front. Opt.* **2014**, *JW3A*, JW3A.28.

(67) Sanghera, J. S.; Heo, J.; Mackenzie, J. D. Chalcogenide Glasses. *J. Non-Cryst. Solids* **1988**, *103*, 155−178.

(68) Alward, J. F.; Fong, C. Y.; et al. Electronic and Optical Properties of SbSBr, SbSI and SbSeI. *Solid State Commun.* **1978**, *25*, 307−310.

(69) Fridkin, V. M.; Gorelov, I. M.; Grekov, A. A.; Lyakhovitskaya, V. A.; Rodin, A. I. Phase Boundry in Ferroelectric SbSI as the Analog of an Electric Domain in a Semiconductor. *ZhETF Pis'ma 4* **1966**, *11*, 461−468.

(70) Nitsche, R.; Merz, W. J. Photoconduction in Ternary V-VI-VII Compounds. *J. Phys. Chem. Solids* **1960**, *13*, 154−155.

(71) Fatuzzo, E.; Harbeke, G.; Merz, W. J.; Nitsche, R.; Roetschi, H.; Ruppel, W. Ferroelectricity in SbSI. *Phy. Rev.* **1962**, *127*, 2036−2037.

(72) Li, T.; Wang, X.; Yan, Y.; Mitzi, D. B. Phase Stability and Electronic Structure of Prospective Sb-Based Mixed Sulfide and Iodide 3D Perovskite $(CH_3NH_3)SbSI_2$. *J. Phys. Chem. Lett.* **2018**, *9*, 3829−3833.

(73) Sun, Y. Y.; Shi, J.; Lian, J.; Gao, W.; Agiorgousis, M. L.; Zhang, P.; Zhang, S. Discovering Lead-Free Perovskite Solar Materials with A Split-Anion Approach. *Nanoscale* **2016**, *8*, 6284−6289.

(74) Butler, K. T.; Frost, J. M.; Walsh, A. Ferroelectric Materials for Solar Energy Conversion: Photoferroics Revisited. *Energy Environ. Sci.* **2015**, *8*, 838−848.

(75) Ran, Z.; Wang, X.; Li, Y.; Yang, D.; Zhao, X.-G.; Biswas, K.; Singh, D. J.; Zhang, L. Bismuth and Antimony-Based Oxyhalides and Chalcohalides As Potential Optoelectronic Materials. *npj Comput. Mater.* **2018**, *4*, 1−7.

(76) Kunioku, H.; Higashi, M.; Abe, R. Low-Temperature Synthesis of Bismuth Chalcohalides: Candidate Photovoltaic Materials with Easily, Continuously Controllable Band gap. *Sci. Rep.* **2016**, *6*, 32664.

(77) Peng, B.; Xu, K.; Zhang, H.; Ning, Z.; Shao, H.; Ni, G.; Li, J.; Zhu, Y.; Zhu, H.; Soukoulis, C. M. 1D SbSeI, SbSI, and SbSBr With High Stability and Novel Properties for Microelectronic, Optoelectronic, and Thermoelectric Applications. *Adv. Theory Simul.* **2018**, *1*, 1700005.

(78) Fenner, J.; Rabenau, A.; Trageser, G. Solid-State Chemistry of Thio-, Seleno-, and Tellurohalides of Representative and Transition Elements. *Adv. Ing. Chem. Radiochem* **1980**, *23*, 329−425.

(79) Nowak, M.; Jesionek, M.; Mistewicz, K. Industrial Applications of Nanomaterials; *Elsevier* **2019**, 225−282.

(80) Nowak, M.; Jesionek, M.; Mistewicz, K. *Nanomaterials Synthesis*; Elsevier, 2019; pp 337−384.

(81) Wlazlak, E.; Blachecki, A.; Bisztyga-Szklarz, M.; Klejna, S.; Mazur, T.; Mech, K.; Pilarczyk, K.; Przyczyna, D.; Suchecki, M.; Zawal, P.; et al. Heavy Pnictogen Chalcohalides: The Synthesis, Structure And Properties of These Rediscovered Semiconductors. *Chem Commun.* **2018**, *54*, 12133−12161.

(82) Wu, L. M.; Wu, X. T.; Chen, L. Structural Overview and Structure-Property Relationships of Iodoplumbate and Iodobismuthate. *Coord. Chem. Rev.* **2009**, *253*, 2787−2804.

(83) Xiao, J. R.; Yang, S. H.; Feng, F.; Xue, H. G.; Guo, S. P. A Review of The Structural Chemistry and Physical Properties of Metal Chalcogenide Halides. *Coord. Chem. Rev.* **2017**, *347*, 23−74.

(84) Nie, R.; Sumukam, R. R.; Reddy, S. H.; Banavoth, M.; Seok, S. I. Lead-free perovskite solar cells enabled by hetero-valent substitutes. *Energy Environ. Sci.* **2020**, *13*, 2363−2385.

(85) Palazon, F. Metal Chalcohalides: Next Generation Photovoltaic Materials? *Sol. RRL* **2022**, *6*, 2100829.

(86) Choi, Y. C.; Jung, K. W. Recent Progress in Fabrication of Antimony/Bismuth Chalcohalides for Lead-Free Solar Cell Applications. *Nanomater.* **2020**, *10*, 2284.

(87) Behler, J. Atom-Centered Symmetry Functions for Constructing High-Dimensional Neural Network Potentials. *J. Chem. Phys.* **2011**, *134*, 074106−13.

(88) Curtarolo, S.; Setyawan, W.; Wang, S.; Xue, J.; Yang, K.; Taylor, R. H.; Nelson, L. J.; Hart, G. L. W.; Sanvito, S.; Buongiorno-Nardelli, M.; et al. AFLOWLIB.ORG: A Distributed Materials Properties Repository from High-Throughput Ab Initio Calculations. *Comput. Mater. Sci.* **2012**, *58*, 227−235.

(89) Stevanović, V.; Lany, S.; Zhang, X.; Zunger, A. Correcting Density Functional Theory for Accurate Predictions of Compound Enthalpies of Formation: Fitted Elemental-Phase Reference Energies. *Phys. Rev. B* **2012**, *85*, 115104−12.

(90) Lany, S. Band-Structure Calculations For The 3d transition Metal Oxides In-GW. *Phys. Rev. B* **2013**, *87*, 085112−9.

(91) Kirklin, S.; Saal, J. E.; Meredig, B.; Thompson, A.; Doak, J. W.; Aykol, M.; Rühl, S.; Wolverton, C. The Open Quantum Materials Database (OQMD): assessing the accuracy of DFT formation energies. *npj Comput. Mater.* **2015**, *1*, 15010.

(92) Luo, S.; Li, T.; Wang, X.; Faizan, M.; Zhang, L. High-Throughput Computational Materials Screening and Discovery Of Optoelectronic Semiconductors. *WIREs Computat. Mol. Sci.* **2021**, *11*, No. e1489.

(93) Ma, X. Y.; Lewis, J. P.; Yan, Q. B.; Su, G. Accelerated Discovery of Two-Dimensional Optoelectronic Octahedral Oxyhalides via High-Throughput Ab Initio Calculations and Machine Learning. *J. Phys. Chem. Lett.* **2019**, *10*, 6734−6740.

(94) Davies, D. W.; Butler, K. T.; Jackson, A. J.; Morris, A.; Frost, J. M.; Skelton, J. M.; Walsh, A. Computational Screening of All Stoichiometric Inorganic Materials. *Chem* **2016**, *1*, 617−627.

(95) Cai, W. B.; Abudurusuli, A.; Xie, C. W.; Tikhonov, E.; Li, J. J.; Pan, S. L.; Yang, Z. H. Toward the Rational Design of Mid-Infrared Nonlinear Optical Materials with Targeted Properties via a Multi-Level Data-Driven Approach. *Adv. Funct. Mater.* **2022**, *32*, 2200231.

(96) Wang, P.; Chu, Y.; Tudi, A.; Xie, C. W.; Yang, Z. H.; Pan, S. L.; Li, J. J. The Combination of Structure Prediction and Experiment for the Exploration of Alkali-Earth Metal-Contained Chalcopyrite-Like IR Nonlinear Optical Material. *Adv. Sci.* **2022**, *9*, 2106120.

(97) Brandt, R. E.; Stevanović, V.; Ginley, D. S.; Buonassisi, T. Identifying Defect-Tolerant Semiconductors With High Minority-Carrier Lifetimes: Beyond Hybrid Lead Halide Perovskites. *MRS Commun.* **2015**, *5*, 265−275.

(98) Chatterjee, S.; Pal, A. J. Influence of Metal Substitution On Hybrid Halide Perovskites: Towards Lead-Free Perovskite Solar Cells. *J. Mater. Chem. A* **2018**, *6*, 3793−3823.

(99) Huang, Y. T.; Kavanagh, S. R.; Scanlon, D. O.; Walsh, A.; Hoye, R. L. Z. Perovskite-Inspired Materials for Photovoltaics And Beyond-From Design to Devices. *Nanotechnol.* **2021**, *32*, 132004.

(100) Li, T.; Luo, S.; Wang, X.; Zhang, L. Alternative Lone-Pair $ns^2$-Cation-Based Semiconductors beyond Lead Halide Perovskites for Optoelectronic Applications. *Adv. Mater.* **2021**, *33*, No. e2008574.

(101) Zhao, X.-G.; Yang, D.; Ren, J.-C.; Sun, Y.; Xiao, Z.; Zhang, L. Rational Design of Halide Double Perovskites for Optoelectronic Applications. *Joule* **2018**, *2*, 1662−1673.

(102) Horak, J.; Turjanica, I. D.; Nejezchleb, K. Synthesis, Optical and Photoelectric Properties Of Semiconducting BiSeI. *Crystals. Krist. Tech* **1968**, *3*, 231−240.

(103) Turyanitsa, I. D.; Zayachkovskij, M. P.; Zayachkovskaya, N. F.; Kozmanko, I. I. Bisei Crystal Growing By The Stockbarger Method. *Izvestiya Akademii Nauk SSSR, Neorganicheskie Materialy* **1974**, *10* (1884), 1884−1885.

(104) Yoo, B.; Ding, D.; Marin-Beloqui, J. M.; Lanzetta, L.; Bu, X.; Rath, T.; Haque, S. A. Improved Charge Separation and Photovoltaic Performance of $BiI_3$ Absorber Layers by Use of an In Situ Formed BiSI Interlayer. *ACS Appl. Energy Mater.* **2019**, *2*, 7056−7061.

(105) Xiao, B.; Zhu, M.; Ji, L.; Zhang, B.-B.; Dong, J.; Yu, J.; Sun, Q.; Jie, W.; Xu, Y. Centimeter Size BiSeI Crystal Grown by Physical Vapor Transport Method. *J. Cryst. Growth* **2019**, *517*, 7−11.

(106) Hahn, N. T.; Rettie, A. J. E.; Beal, S. K.; Fullon, R. R.; Mullins, C. B. n-BiSI Thin Films: Selenium Doping and Solar Cell Behavior. *J. Phys. Chem. C* **2012**, *116*, 24878−24886.

(107) Groom, R. A.; Jacobs, A.; Cepeda, M.; Drummey, R.; Latturner, S. E. Structural and Optical Properties of Sb-Substituted BiSI Grown from Sulfur/Iodine Flux. *Inorg Chem.* **2017**, *56*, 12362−12368.

(108) Zhou, C.; Wang, R.; Jiang, C.; Chen, J.; Wang, G. Dynamically Optimized Multi-interface Novel BiSI-Promoted Redox Sites Spatially Separated n-p-n Double Heterojunctions $BiSI/MoS_2/CdS$ for Hydrogen Evolution. *Ind. Eng. Chem. Res.* **2019**, *58*, 7844−7856.

(109) Islam, S. M.; Malliakas, C. D.; Sarma, D.; Maloney, D. C.; Stoumpos, C. C.; Kontsevoi, O. Y.; Freeman, A. J.; Kanatzidis, M. G. Direct Gap Semiconductors $Pb_2BiS_2I_3$, $Sn_2BiS_2I_3$, and $Sn_2BiSI_5$. *Chem. Mater.* **2016**, *28*, 7332−7343.

(110) Pai, N.; Lu, J.; Gengenbach, T. R.; Seeber, A.; Chesman, A. S. R.; Jiang, L.; Senevirathna, D. C.; Andrews, P. C.; Bach, U.; Cheng, Y. B.; et al. Silver Bismuth Sulfoiodide Solar Cells: Tuning Optoelectronic Properties by Sulfide Modification for Enhanced Photovoltaic Performance. *Adv. Energy Mater.* **2019**, *9*, 1803396.

(111) Lin, W.; Stoumpos, C. C.; Kontsevoi, O. Y.; Liu, Z.; He, Y.; Das, S.; Xu, Y.; McCall, K. M.; Wessels, B. W.; Kanatzidis, M. G. $Cu_2I_2Se_6$: A Metal-Inorganic Framework Wide-Bandgap Semiconductor for Photon Detection at Room Temperature. *J. Am. Chem. Soc.* **2018**, *140*, 1894−1899.

(112) Toso, S.; Akkerman, Q. A.; Martin-Garcia, B.; Prato, M.; Zito, J.; Infante, I.; Dang, Z.; Moliterni, A.; Giannini, C.; Bladt, E.; et al. Nanocrystals of Lead Chalcohalides: A Series of Kinetically Trapped Metastable Nanostructures. *J. Am. Chem. Soc.* **2020**, *142*, 10198−10211.

(113) Sun, Y. Y.; Agiorgousis, M. L.; Zhang, P.; Zhang, S. Chalcogenide Perovskites For Photovoltaics. *Nano. Lett.* **2015**, *15*, 581−585.

(114) Li, J.; Huang, J.; Li, K.; Zeng, Y.; Zhang, Y.; Sun, K.; Yan, C.; Xue, C.; Chen, C.; Chen, T.; et al. Defect-Resolved Effective Majority Carrier Mobility in Highly Anisotropic Antimony Chalcogenide Thin-Film Solar Cells. *Solar RRL* **2021**, *5*, 2000693.

(115) Yu, L.; Lany, S.; Kykyneshi, R.; Jieratum, V.; Ravichandran, R.; Pelatt, B.; Altschul, E.; Platt, H. A. S.; Wager, J. F.; Keszler, D. A.; et al. Iron Chalcogenide Photovoltaic Absorbers. *Adv. Energy Mater.* **2011**, *1*, 748−753.

(116) Agiorgousis, M. L.; Sun, Y. Y.; Choe, D. H.; West, D.; Zhang, S. Machine Learning Augmented Discovery of Chalcogenide Double Perovskites for Photovoltaics. *Adv. Theor. Simul.* **2019**, *2*, 1800173.

(117) Frost, J. M. Calculating Polaron Mobility in Halide Perovskites. *Phys. Rev. B* **2017**, *96*, 195202−10.

(118) Wilson, J. N.; Frost, J. M.; Wallace, S. K.; Walsh, A. Dielectric and Ferroic Properties of Metal Halide Perovskites. *APL Mater.* **2019**, *7*, 010901−14.

(119) Su, R.; Xu, Z.; Wu, J.; Luo, D.; Hu, Q.; Yang, W.; Yang, X.; Zhang, R.; Yu, H.; Russell, T. P.; et al. Dielectric Screening in Perovskite Photovoltaics. *Nat. Commun.* **2021**, *12*, 2479.

(120) Baranowski, M.; Plochocka, P. Excitons in Metal-Halide Perovskites. *Adv. Energy Mater.* **2020**, *10*, 1903659.

(121) Blancon, J. C.; Even, J.; Stoumpos, C. C.; Kanatzidis, M. G.; Mohite, A. D. Semiconductor Physics of Organic-Inorganic 2D Halide Perovskites. *Nat Nanotechnol.* **2020**, *15*, 969−985.

(122) Yang, Y.; Gu, J.; Young, J. L.; Miller, E. M.; Turner, J. A.; Neale, N. R.; Beard, M. C. Semiconductor Interfacial Carrier Dynamics via Photoinduced Electric Fields,. *Science* **2015**, *350*, 1062−1065.

(123) Eskandari, R.; Zhang, X.; Malkinski, L. M. Polarization-dependent photovoltaic effect in ferroelectric-semiconductor system. *Appl. Phys. Lett.* **2017**, *110*, 121105−5.

(124) Shahrokhi, S.; Gao, W.; Wang, Y.; Anandan, P. R.; Rahaman, M. Z.; Singh, S.; Wang, D.; Cazorla, C.; Yuan, G.; Liu, J. M.; et al. Emergence of Ferroelectricity in Halide Perovskites. *Small Methods* **2020**, *4*, 200149.

(125) Li, X.; Chen, S.; Liu, P. F.; Zhang, Y.; Chen, Y.; Wang, H. L.; Yuan, H.; Feng, S. Evidence for Ferroelectricity of All-Inorganic Perovskite $CsPbBr_3$ Quantum Dots. *J. Am. Chem. Soc.* **2020**, *142*, 3316−3320.

(126) Liao, W. Q.; Zhang, Y.; Hu, C. L.; Mao, J. G.; Ye, H. Y.; Li, P. F.; Huang, S. D.; Xiong, R. G. A Lead-Halide Perovskite Molecular Ferroelectric Semiconductor. *Nat. Commun.* **2015**, *6*, 7338.

(127) Shu, L.; Ke, S.; Fei, L.; Huang, W.; Wang, Z.; Gong, J.; Jiang, X.; Wang, L.; Li, F.; Lei, S.; et al. Photoflexoelectric Effect in Halide Perovskites. *Nat. Mater.* **2020**, *19*, 605−609.

(128) Kooi, B. J.; Noheda, B. Ferroelectric chalcogenides-materials at the edge. *Science* **2016**, *353*, 221−222.

(129) Zhang, Y.; Shimada, T.; Kitamura, T.; Wang, J. Ferroelectricity in Ruddlesden-Popper Chalcogenide Perovskites for Photovoltaic Application: The Role of Tolerance Factor. *J. Phys. Chem. Lett.* **2017**, *8*, 5834−5839.

(130) Moriwake, H.; Konishi, A.; Ogawa, T.; Fujimura, K.; Fisher, C. A. J.; Kuwabara, A.; Shimizu, T.; Yasui, S.; Itoh, M. Ferroelectricity in wurtzite structure simple chalcogenide. *Appl. Phys. Lett.* **2014**, *104*, 242909−3.

(131) Wang, C.; Zhang, M.; Wang, R.; Zhang, C.; Meng, X.; Xi, Y.; Li, S.; Yan, H. First-Principles Investigation into Hybrid Improper Ferroelectricity in Ruddlesden-Popper Perovskite Chalcogenides $Sr_3B_2X_7$ (B = Ti, Zr, Hf; X = S, Se). *J. Phys. Chem. C* **2021**, *125* (25), 13971−1383.

(132) Allan, G.; Delerue, C.; Lannoo, M.; Martin, E. Hydrogenic Impurity Levels, Dielectric Constant, and Coulomb Charging Effects in Silicon Crystallites. *Phys. Rev. B Condens. Matter* **1995**, *52*, 11982−11988.

(133) Ganose, A. M.; Butler, K. T.; Walsh, A.; Scanlon, D. O. Relativistic Electronic Structure and Band Alignment of BiSI and BiSeI: Candidate Photovoltaic Materials. *J. Mater. Chem. A* **2016**, *4*, 2060−2068.

(134) Xiao, Z.; Yan, Y. Progress in Theoretical Study of Metal Halide Perovskite Solar Cell Materials. *Adv. Energy Mater* **2017**, *7*, 1701136.

(135) Wang, K.; Yang, D.; Wu, C.; Sanghadasa, M.; Priya, S. Recent Progress In Fundamental Understanding of Halide Perovskite Semiconductors. *Prog. Mater. Sci.* **2019**, *106*, 100580.

(136) Davies, D. W.; Butler, K. T.; Skelton, J. M.; Xie, C.; Oganov, A. R.; Walsh, A. Computer-Aided Design of Metal Chalcohalide Semiconductors: From Chemical Composition to Crystal Structure. *Chem. Sci.* **2018**, *9*, 1022−1030.

(137) Mao, X.; Han, K.-L.; Deng, W.-Q.; Sun, L. First-Principles Screening of Lead-Free Mixed-Anion Perovskites for Photovoltaics. *J. Phys. Chem. C* **2020**, *124*, 1303−1308.

(138) Farooq, U.; Ishaq, M.; Shah, U. A.; Chen, S.; Zheng, Z.-H.; Azam, M.; Su, Z.-H.; Tang, R.; Fan, P.; Bai, Y.; et al. Bandgap Engineering of Lead-Free Ternary Halide Perovskites for Photovoltaics And Beyond: Recent Progress And Future Prospects. *Nano Energy* **2022**, *92*, 106710.

(139) Baranwal, A. K.; Masutani, H.; Sugita, H.; Kanda, H.; Kanaya, S.; Shibayama, N.; Sanehira, Y.; Ikegami, M.; Numata, Y.; Yamada, K.; et al. Lead-Free Perovskite Solar Cells using Sb And Bi-Based $A_3B_2X_9$ And $A_3BX_6$ Crystals with Normal and Inverse Cell Structures. *Nano Converg.* **2017**, *4*, 26.

(140) Kumar, D.; Kaur, J.; Mohanty, P. P.; Ahuja, R.; Chakraborty, S. Recent Advancements in Nontoxic Halide Perovskites: Beyond Divalent Composition Space. *ACS Omega* **2021**, *6*, 33240−33252.

(141) Li, J.; Duan, J.; Yang, X.; Duan, Y.; Yang, P.; Tang, Q. Review On Recent Progress of Lead-Free Halide Perovskites in Optoelectronic Applications. *Nano Energy* **2021**, *80*, 105526.

(142) Umeyama, D.; Lin, Y.; Karunadasa, H. I. Red-to-Black Piezochromism in a Compressible Pb-I-SCN Layered Perovskite. *Chem. Mater.* **2016**, *28*, 3241−3244.

(143) Shi, H.; Ming, W.; Du, M.-H. Bismuth Chalcohalides and Oxyhalides s Optoelectronic Materials. *Phys. Rev. B* **2016**, *93*, 104108−7.

(144) Ganose, A. M.; Savory, C. N.; Scanlon, D. O. Beyond Methylammonium Lead Iodide: Prospects for The Emergent Field Of $ns^2$ Containing Solar Absorbers. *Chem. Commun.* **2017**, *53*, 20−44.

(145) Ganose, A. M.; Cuff, M.; Butler, K. T.; Walsh, A.; Scanlon, D. O. Interplay of Orbital and Relativistic Effects in Bismuth Oxyhalides: BiOF, BiOCl, BiOBr, and BiOI. *Chem. Mater.* **2016**, *28*, 1980−1984.

(146) Brandt, R. E.; Poindexter, J. R.; Gorai, P.; Kurchin, R. C.; Hoye, R. L. Z.; Nienhaus, L.; Wilson, M. W. B.; Polizzotti, J. A.; Sereika, R.; Žaltauskas, R.; et al. Searching for "Defect-Tolerant" Photovoltaic Materials: Combined Theoretical and Experimental Screening. *Chem. Mater.* **2017**, *29*, 4667−4674.

(147) Nie, R.; Yun, H.-s.; Paik, M.-J.; Mehta, A.; Park, B.-w.; Choi, Y. C.; Seok, S. I. Efficient Solar Cells Based on Light-Harvesting Antimony Sulfoiodide. *Adv. Energy Mater.* **2018**, *8*, 1708901.

(148) Tang, G.; Ghosez, P.; Hong, J. Band-Edge Orbital Engineering of Perovskite Semiconductors for Optoelectronic Applications. *J. Phys. Chem. Lett.* **2021**, *12*, 4227−4239.

(149) Wang, K.; Liang, Z. Q.; Wang, X. Q.; Cui, X. D. Lead Replacement in $CH_3NH_3PbI_3$ Perovskites. *Adv. Electron. Mater.* **2015**, *1*, 1500089.

(150) Walsh, A.; Payne, D. J.; Egdell, R. G.; Watson, G. W. Stereochemistry of Post-Transition Metal Oxides: Revision of the Classical Lone Pair Model. *Chem. Soc. Rev.* **2011**, *40*, 4455−4463.

(151) Jones, L. A. H.; Linhart, W. M.; Fleck, N.; Swallow, J. E. N.; Murgatroyd, P.; Shiel, H.; Featherstone, T.; Smiles, M.; Thakur, P.; Lee, T.; Hardwick, L.; et al. Sn $5s^2$ Lone Pairs and the Electronic Structure of Tin Sulphides: A Photoreflectance, High-Energy Photoemission and Theoretical Investigation. *Phy. Rev. Mater.* **2020**, *4*, 074602.

(152) Walsh, A.; Zunger, A. Instilling Defect Tolerance in New Compounds. *Nat. Mater.* **2017**, *16*, 964−967.

(153) Tennyson, E. M.; Doherty, T. A. S.; Stranks, S. D. Heterogeneity at Multiple Length Scales in Halide Perovskite Semiconductors. *Nat. Rev. Mater.* **2019**, *4*, 573.

(154) Jin, H.; Debroye, E.; Keshavarz, M.; Scheblykin, I. G.; Roeffaers, M. B. J.; Hofkens, J.; Steele, J. A. It's a trap! On the Nature of Localised States and Charge Trapping in Lead Halide Perovskites. *Mater. Horiz.* **2020**, *7*, 397−410.

(155) Zhang, X.; Turiansky, M. E.; Van de Walle, C. G. Correctly Assessing Defect Tolerance in Halide Perovskites. *J. Phy. Chem. C* **2020**, *124*, 6022−6027.

(156) Godel, K. C.; Steiner, U. Thin Film Synthesis of SbSI Micro-Crystals for Self-Powered Photodetectors with Rapid Time Response. *Nanoscale* **2016**, *8*, 15920−15925.

(157) Umari, P.; Mosconi, E.; De Angelis, F. Relativistic GW Calculations on $CH_3NH_3PbI_3$ and $CH_3NH_3SnI_3$ Perovskites for Solar Cell Applications. *Sci. Rep.* **2015**, *4*, 4467.

(158) Zhou, Y.; Wang, L.; Chen, S.; Qin, S.; Liu, X.; Chen, J.; Xue, D.-J.; Luo, M.; Cao, Y.; Cheng, Y.; et al. Thin-film $Sb_2Se_3$ Photovoltaics with Oriented One-Dimensional Ribbons and Benign Grain Boundaries. *Nat. Photonics* **2015**, *9*, 409−415.

(159) Rothmann, M. U.; Kim, J. S.; Borchert, J.; Lohmann, K. B.; O'Leary, C. M.; Sheader, A. A.; Clark, L.; Snaith, H. J.; Johnston, M. B.; Nellist, P. D.; et al. Atomic-Scale Microstructure of Metal Halide Perovskite. *Science* **2020**, *370*, No. eabb5940.

(160) Zhou, Y.; Zhao, Y. Chemical Stability and Instability of Inorganic Halide Perovskites. *Energy Environ. Sci.* **2019**, *12*, 1495−1511.

(161) Stoumpos, C. C.; Kanatzidis, M. G. Halide Perovskites: Poor Man's High-Performance Semiconductors. *Adv. Mater.* **2016**, *28*, 5778−5793.

(162) Xiang, W.; Liu, S.; Tress, W. A Review on the Stability of Inorganic Metal Halide Perovskites: Challenges and Opportunities for Stable Solar Cells. *Energy Environ. Sci.* **2021**, *14*, 2090−2113.

(163) Romani, L.; Speltini, A.; Dibenedetto, C. N.; Listorti, A.; Ambrosio, F.; Mosconi, E.; Simula, A.; Saba, M.; Profumo, A.; Quadrelli, P.; et al. Experimental Strategy and Mechanistic View to Boost the Photocatalytic Activity of $Cs_3Bi_2Br_9$ Lead-Free Perovskite Derivative by $g-C_3N_4$ Composite Engineering. *Adv. Funct. Mater.* **2021**, *31*, 2104428.

(164) Kim, G.; Min, H.; Lee, K. S.; Lee, D. Y.; Yoon, S. M.; Seok, S. I. Impact Of Strain Relaxation On Performance Of A-Formamidinium Lead Iodide Perovskite Solar Cells,. *Science* **2020**, *370*, 108−112.

(165) Jones, T. W.; Osherov, A.; Alsari, M.; Sponseller, M.; Duck, B. C.; Jung, Y.-K.; Settens, C.; Niroui, F.; Brenes, R.; Stan, C. V.; et al. Lattice Strain Causes Non-Radiative Losses In Halide Perovskites. *Energy Environ. Sci.* **2019**, *12*, 596−606.

(166) Liu, D.; Luo, D.; Iqbal, A. N.; Orr, K. W. P.; Doherty, T. A. S.; Lu, Z. H.; Stranks, S. D.; Zhang, W. Strain Analysis And Engineering In Halide Perovskite Photovoltaics. *Nat. Mater.* **2021**, *20*, 1337−1346.

(167) Saidaminov, M. I.; Kim, J.; Jain, A.; Quintero-Bermudez, R.; Tan, H.; Long, G.; Tan, F.; Johnston, A.; Zhao, Y.; Voznyy, O.; et al. Suppression of Atomic Vacancies Via Incorporation Of Isovalent Small Ions To Increase The Stability of Halide Perovskite Solar Cells In Ambient Air. *Nat. Energy* **2018**, *3*, 648−654.

(168) Li, X.; Liang, F.; Liu, T.; Li, H. $Na_2GaS_2Cl$: A New Sodium-Rich Chalcohalide With Two-Dimensional $[GaS_2]$ Infinity Layers And Wide Interlayer Space. *Dalton Trans.* **2021**, *50*, 11167−11172.

(169) Zakutayev, A.; Caskey, C. M.; Fioretti, A. N.; Ginley, D. S.; Vidal, J.; Stevanovic, V.; Tea, E.; Lany, S. Defect Tolerant Semiconductors For Solar Energy Conversion. *J. Phys. Chem. Lett.* **2014**, *5*, 1117−1125.

(170) Sereika, R.; Žaltauskas, R.; Lapeika, V.; Stanionyte, S.; Juškenas, R. Structural Changes in Chlorine-Substituted SbSI. *J. Appl. Phys.* **2019**, *126*, 114101−5.

(171) Molnar, B.; Johannes, H. W. *Bull. Am. Phys. Soc.* **1965**, *10*, 109.

(172) Fong, C. Y.; Perlov, C.; Wooten, F Electronic Properties of BiSeI and BiSeBr.pdf. *J. Phys. C: Solid State Phys.* **1982**, *15*, 2605−2612.

(173) Ganose, A. M.; Matsumoto, S.; Buckeridge, J.; Scanlon, D. O. Defect Engineering of Earth-Abundant Solar Absorbers BiSI and BiSeI. *Chem. Mater.* **2018**, *30*, 3827−3835.

(174) Wu, Y.; Pan, H.; Zhou, X.; Li, M.; Zhou, B.; Yang, C.; Zhang, W. H.; Jie, J.; Li, C. Shape and Composition Control of $Bi_{19}S_{27}(Br_{3-X},I)$ Alloyed Nanowires: The Role of Metal Ions. *Chem. Sci.* **2015**, *6*, 4615−4622.

(175) Yan, Y.; Xu, Y.; Lei, S.; Ou, X.; Chen, L.; Xiong, J.; Xiao, Y.; Cheng, B. Fabrication of $Bi_{19}S_{27}I_3$ Nanorod Cluster Films For Enhanced Photodetection Performance. *Dalton Trans.* **2018**, *47* (10), 3408−3416.

(176) Adams, K.; González, A. F.; Mallows, J.; Li, T.; Thijssen, J. H. J.; Robertson, N. Facile Synthesis And Characterization of $Bi_{13}S_{18}I_2$ Films As A Stable Supercapacitor Electrode Material. *J. Mater. Chem. A* **2019**, *7*, 1638−1646.

(177) Xu, B.; Feng, T.; Agne, M. T.; Tan, Q.; Li, Z.; Imasato, K.; Zhou, L.; Bahk, J. H.; Ruan, X.; Snyder, G. J.; et al. Manipulating Band Structure through Reconstruction of Binary Metal Sulfide for High-Performance Thermoelectrics in Solution-Synthesized Nanostructured $Bi_{13}S_{18}I_2$. *Angew. Chem., Int. Ed.* **2018**, *57*, 2413−2418.

(178) Groom, R.; Jacobs, A.; Cepeda, M.; Drummey, R.; Latturner, S. E. $Bi_{13}S_{18}I_2$: (Re)discovery of a Subvalent Bismuth Compound Featuring $[Bi_2]^{4+}$ Dimers Grown in Sulfur/Iodine Flux Mixtures. *Chem. Mater.* **2017**, *29*, 3314−3323.

(179) Miehe, G.; Kupčík, V. Die Kristallstruktur des $Bi(Bi_2S_3)_9I_3$. *Naturwissenschaften* **1971**, *58*, 219.

(180) Mariolacos, K. The Crystal Structure Of $Bi(Bi_2S_3)_9Br_3$. *Acta Crystallogr.* **1976**, *B32*, 1947−1949.

(181) Li, S.; Xu, L.; Kong, X.; Kusunose, T.; Tsurumachi, N.; Feng, Q. Bismuth Chalcogenide Iodides $Bi_{13}S_{18}I_2$ And BiSI: Solvothermal Synthesis, Photoelectric Behavior, and Photovoltaic Performance. *J. Mater. Chem. C* **2020**, *8*, 3821−3829.

(182) Ni, D.; Guo, S.; Powderly, K. M.; Zhong, R.; Cava, R. J. A High-Pressure Phase With A Non-Centrosymmetric Crystal Structure In The $PbSe-PbBr_2$ System. *J. Solid State Chem.* **2019**, *280*, 120982.

(183) Krebs, V. B. Die Kristallstrukturen von $Pb_4SeBr_6$, $Pb_5S_2I_6$ und $Pb_7S_2Br_{10}$. *Z. Anorg. Allg. Chem.* **1973**, *396*, 137−151.

(184) Ni, D.; Guo, S.; Yang, Z. S.; Powderly, K. M.; Cava, R. J. $Pb_4S_3I_2$-A High-Pressure Phase in The $PbS-PbI_2$ System. *Solid State Sci.* **2019**, *91*, 49−53.

(185) Kavanagh, S. R.; Savory, C. N.; Scanlon, D. O.; Walsh, A. Hidden Spontaneous Polarisation in The Chalcohalide Photovoltaic Absorber $Sn_2SbS_2I_3$. *Mater. Horiz.* **2021**, *8*, 2709−2716.

(186) Nie, R.; Mehta, A.; Park, B. W.; Kwon, H. W.; Im, J.; Seok, S. I. Mixed Sulfur and Iodide-Based Lead-Free Perovskite Solar Cells. *J. Am. Chem. Soc.* **2018**, *140*, 872−875.

(187) Hong, F.; Saparov, B.; Meng, W.; Xiao, Z.; Mitzi, D. B.; Yan, Y. Viability of Lead-Free Perovskites with Mixed Chalcogen and Halogen Anions for Photovoltaic Applications. *J. Phys. Chem. C* **2016**, *120*, 6435−6441.

(188) Shin, D. W.; Hyun, S. C.; Park, S. A.; Kim, Y. G.; Kim, C. D.; Kim, W. T. Optical Properties Of Undoped and Ni-Doped VA-VIA-VIIA Single Crystals. *J. Phys. Chem. Solids* **1994**, *55*, 825−830.

(189) Chepur, D. V.; Beruea, D. M.; Turyanitsa, I. D.; Sum, V. Y. Peculiarities of the Energy Spectrum and Edge Absorption in the Chain Compounds $A^VB^{VI}C^{VII}$. *Phys. Status Solidi* **1968**, *30*, 461−468.

(190) Tiwari, D.; Cardoso-Delgado, F.; Alibhai, D.; Mombrú, M.; Fermín, D. J. Photovoltaic Performance of Phase-Pure Orthorhombic BiSI Thin-Films. *ACS Appl. Energy Mater.* **2019**, *2*, 3878−3885.

(191) Han, D.; Du, M. H.; Dai, C. M.; Sun, D.; Chen, S. Influence Of Defects And Dopants on the Photovoltaic Performance of $Bi_2S_3$: First-Principles Insights. *J. Mater. Chem. A* **2017**, *5*, 6200−6210.

(192) Wu, Y.; Zhou, B.; Yang, C.; Zhou, X.; Zhang, W. H. Bismuth-Based Ternary Nanowires As Efficient Electrocatalysts For Dye Sensitized Solar Cells. *Chem. Commun.* **2017**, *53*, 5445−5448.

(193) Nako, K.; Balkanski, M. Electronic Band Structures of SbSI in the Para- and Ferroelectric. *Phases. Phys. Rev. B* **1973**, *8*, 5759−5780.

(194) Audzijonis, A.; Žaltauskas, R.; Audzijoniene, L.; Vinokurova, I. V.; Farberovich, O. V.; Šadžius, R. Electronic Band Structure of

Ferroelectric Semiconductor SbSI Studied By Empirical Pseudopotential. *Ferroelectr.* **1998**, *211*, 111−126.

(195) Akkus, H.; Mamedov, A. M. Ab Initio Calculations of the Electronic Structure and Linear Optical Properties, Including Self-Energy Effects for Paraelectric SbSI. *J. Phys.: Condens. Matter* **2007**, *19*, 116207.

(196) Khan, W.; Hussain, S.; Minar, J.; Azam, S. Electronic and Thermoelectric Properties of Ternary Chalcohalide Semiconductors: First Principles Study. *J. Electron. Mater.* **2018**, *47*, 1131−1139.

(197) Butler, K. T.; McKechnie, S.; Azarhoosh, P.; Schilfgaarde, M. V.; Scanlon, D. O.; Walsh, A. Quasi-Particle Electronic Band Structure and Alignment of the V-VI-VII Semiconductors SbSI, SbSBr, SbSeI for Solar Cells. *Appl. Phys. Lett.* **2016**, *108*, 112103.

(198) Zhang, W.; Eperon, G. E.; Snaith, H. J. Metal Halide Perovskites for Energy Applications. *Nat. Energy* **2016**, *1*, 16048.

(199) Quan, L. N.; Rand, B. P.; Friend, R. H.; Mhaisalkar, S. G.; Lee, T. W.; Sargent, E. H. Perovskites for Next-Generation Optical Sources. *Chem. Rev.* **2019**, *119*, 7444−7477.

(200) Grinberg, I.; West, D. V.; Torres, M.; Gou, G.; Stein, D. M.; Wu, L.; Chen, G.; Gallo, E. M.; Akbashev, A. R.; Davies, P. K.; et al. Perovskite Oxides for Visible-Light-Absorbing Ferroelectric and Photovoltaic Materials. *Nature* **2013**, *503*, 509−512.

(201) Jodlowski, A.; Rodríguez-Padrón, D.; Luque, R.; de Miguel, G. Alternative Perovskites for Photovoltaics. *Adv. Energy Mater.* **2018**, *8*, 1703120.

(202) Horák, J.; Cermák, K. Preparation and Photoelectric Properties of Bismuth Sulphidiodide. *Cechoslovackij fiziceskij zurnal B* **1965**, *15*, 536−538.

(203) Sasaki, Y. Photoconductivity of a Ferroelectric Photoconductor BiSI. *J. Appl. Phy.* **1965**, *4*, 614−615.

(204) Kumar, R. R.; Raman, G.; Gnanam, F. Growth of Single Crystals of Bismuth Sulpho Iodide in Gel. *J. Mater. Sci.* **1989**, *24*, 4531−4534.

(205) Ganesha, R.; Arivuoli, D.; Ramasamy, P. Growth of Some Group V-VI-VII Compounds from the Vapour. *J. Cryst. Growth* **1993**, *128*, 1081−1085.

(206) Park, S.-A.; Kim, M.-Y.; Lim, J.-Y.; Park, B.-S.; Koh, J.-D.; Kim, W.-T. Optical Properties of Undoped and V-Doped VA-VIA-VIIA Single Crystals. *Phys. Status Solidi* **1995**, *187*, 253−260.

(207) Zhu, L.; Xie, Y.; Zheng, X.; Yin, X.; Tian, X. Growth of Compound BiIII-VIA-VIIA Crystals with Special Morphologies Under Mild Conditions. *Inorg. Chem.* **2002**, *41*, 4560−4566.

(208) Su, X.; Zhang, G.; Liu, T.; Liu, Y.; Qin, J.; Chen, C. A Facile and Clean Synthesis of Pure Bismuth Sulfide Iodide Crystals. *Russ. J. Inorg. Chem.* **2006**, *51*, 1864−1868.

(209) Wang, W.; Wang, S.-Y.; Liu, M. Growth of Rod-Like Crystal BiSI Films by Ultrasonic Spray Pyrolysis. *Mater. Res. Bull.* **2005**, *40*, 1781−1786.

(210) Cao, Z.; He, Y.; Sun, L.; Cao, X. The Competitive Growth of BiOI and BiSI in the Solvothermal Process. *Adv. Mater. Res.* **2011**, *236−238*, 1919−1922.

(211) Zhu, L.; Zheng, X.; Yin, X.; Liu, X.; Jia, Y.; Xie, Y. A Mild Solution Route to Bismuth Selenoiodide Rod-Like Crystals. *Chem. Lett.* **2003**, *32*, 350−351.

(212) Quarta, D.; Toso, S.; Giannuzzi, R.; Caliandro, R.; Moliterni, A.; Saleh, G.; Capodilupo, A. L.; Debellis, D.; Prato, M.; Nobile, C.; et al. Colloidal Bismuth Chalcohalide Nanocrystals. *Angew. Chem., Int. Ed.* **2022**, *134*, No. e202201747.

(213) Donges, V. E. On Chalcogen Halides of Trivalent Antimony and Bismuth. *Zeitschrift Fur Snorganische Und Allgemeine Chemie* **1950**, *263*, 280−291.

(214) Francois, F.; Delwaulle, M. L. Preparation of Bismuth Iodosulphide by the Wet Method. *Bull. Soc. Chim.* **1936**, *3*, 504−508.

(215) Nassau, K.; Shiever, J. W.; Kowalchik, M. The Growth of Large SbSI Crystals. *J. Cryst. Growth* **1970**, *7*, 237−245.

(216) Donges, V. E. About Thiohalides of Trivalent Antimony and Bismuth. *Zeitschrift fur Anorganische hnd Axgemeine Chemie* **1950**, *263*, 112−132.

(217) Nitsche, R.; Merz, W. Photoconduction in Ternary V-VI-VII Compounds. *J. Phys. Chem. Solids* **1960**, *13*, 154−155.

(218) Zhu, L.; Xie, Y.; Zheng, X.; Yin, X.; Tian, X. Growth of Compound Crystals with Special Morphologies Under Mild Conditions. *Inorg. Chem.* **2002**, *41*, 4563−4566.

(219) Xu, Z. C.; Fong, C. Y.; Wooten, F.; Yeh, Y. Reflectance Ellipsometry Studies of the Ternary Chalcohalides SbSI, SbSeI and BiSI near Room Temperature. *Ferroelectrics* **1984**, *56*, 187−202.

(220) Li, Z.; Zhang, Q.; Wu, L.; Gu, W.; Liu, Y. Mechanochemical Synthesis of BiSI and $Bi_{19}S_{27}I_3$ Semiconductor Materials. *Adv. Powder Technol.* **2019**, *30*, 1985−1988.

(221) Kvedaravičius, S.; Audzijonis, A.; Mykolaitiene, N.; Jcancerevičius, A. The Electronic Potential of the V-VI-VII Compounds in the Region of Phase Transition. *Phase Transitions* **1996**, *58*, 235−246.

(222) Audzijonis, A.; Sereika, R.; Žaltauskas, R. Antiferroelectric Phase Transition in SbSI and SbSeI Crystals. *Solid State Commun.* **2008**, *147*, 88−89.

(223) Mistewicz, K.; Nowak, M.; Stroz, D. A Ferroelectric-Photovoltaic Effect in SbSI Nanowires. *Nanomaterials* **2019**, *9*, 580.

(224) Hahn, N. T.; Self, J. L.; Mullins, C. B. BiSI Micro-Rod Thin Films: Efficient Solar Absorber Electrodes? *J. Phys. Chem. Lett* **2012**, *3*, 1571−1576.

(225) Choi, Y. C.; Hwang, E. Controlled Growth of BiSI Nanorod-Based Films Through a Two-Step Solution Process for Solar Cell Applications. *Nanomaterials* **2019**, *9*, 1650.

(226) Deng, C.; Guan, H.; Tian, X. Novel $Bi_{19}S_{27}Br_3$ Superstructures: Facile Microwave-Assisted Aqueous Synthesis and Their Visible Light Photocatalytic Performance. *Mater. Lett.* **2013**, *108*, 17−20.

(227) Chen, Y.; Tian, G.; Feng, T.; Zhou, W.; Ren, Z.; Han, T.; Xiao, Y.; Fu, H. Single-Crystalline $Bi_{19}Br_3S_{27}$ Nanorods with an Efficiently Improved Photocatalytic Activity. *CrystEngComm* **2015**, *17*, 6120−6126.

(228) Wu, Z.; Jiang, Y.; Xiong, X.; Ding, S.; Shi, Y.; Liu, X.; Liu, Y.; Huang, Z.; Hu, J. Synthesis and Characterization of Single-Crystalline $Bi_{19}Cl_3S_{27}$ Nanorods. *Catal. Sci. Technol.* **2017**, *7*, 3464−3468.

(229) Wu, Z.; Liu, Y.; Zhang, S.; Huang, Z.; Jiang, Q.; Zhou, T.; Hu, J. Biomimetic Structure Design and Construction of Cactus-like $MoS_2$/$Bi_{19}Cl_3S_{27}$ Photocatalysts for Efficient Hydrogen Evolution. *J. Mater. Chem. A* **2018**, *6*, 21404−21409.

(230) Chen, Z.; Wu, Z.; Song, Z.; Zhang, X.; Yang, H.; Jiang, Q.; Zhou, T.; Liu, N.; Hu, J. Crucial Effect of Halogen on the Photocatalytic Hydrogen Evolution for $Bi_{19}X_3S_{27}$ (X = Cl, Br) Nanomaterials. *Ind. Eng. Chem. Res.* **2019**, *58*, 22958−22966.

(231) Farooq, S.; Feeney, T.; Mendes, J. O.; Krishnamurthi, V.; Walia, S.; Della Gaspera, E.; van Embden, J. High Gain Solution-Processed Carbon-Free BiSI Chalcohalide Thin Film Photodetectors. *Adv. Funct. Mater.* **2021**, *31*, 2104788.

(232) Choi, Y. C.; Hwang, E.; Kim, D.-H. Controlled Growth of SbSI Thin Films from Amorphous $Sb_2S_3$ for low-Temperature Solution Processed Chalcohalide Solar Cells. *APL Mater.* **2018**, *6*, 121108−8.

(233) Choi, Y. C.; Seok, S. I. Efficient $Sb_2S_3$-Sensitized Solar Cells Via Single-Step Deposition of $Sb_2S_3$ Using S/Sb-Ratio-Controlled $SbCl_3$-Thiourea Complex Solution. *Adv. Funct. Mater.* **2015**, *25*, 2892−2898.

(234) Nie, R.; Im, J.; Seok, S. I. Efficient Solar Cells Employing Light-Harvesting $Sb_{0.67}Bi_{0.33}SI$. *Adv. Mater.* **2019**, *31*, No. e1808344.

(235) Nowak, M.; Kauch, B.; Szperlich, P.; Jesionek, M.; Kepinska, M.; Bober, L.; Szala, J.; Moskal, G.; Rzychon, T.; Stroz, D. Sonochemical Preparation of SbSeI Gel. *Ultrason. Sonochem.* **2009**, *16*, 546−551.

(236) Wibowo, A. C.; Malliakas, C. D.; Liu, Z.; Peters, J. A.; Sebastian, M.; Chung, D. Y.; Wessels, B. W.; Kanatzidis, M. G. Photoconductivity in the Chalcohalide Semiconductor, SbSeI: a New Candidate for Hard Radiation Detection. *Inorg. Chem.* **2013**, *52*, 7045−7050.

(237) Shannon, R. D. Revised Effective Ionic Radii and Systematic Studies of Interatomie Distances in Halides and Chaleogenides. *Acta Crystallogr.* **1976**, *A32*, 751−767.

(238) Nie, R.; Hu, M.; Risqi, A. M.; Li, Z.; Seok, S. I. Efficient and Stable Antimony Selenoiodide Solar Cells. *Adv. Sci.* **2021**, *8*, 2003172.

(239) Xu, C.; Ravi Anusuyadevi, P.; Aymonier, C.; Luque, R.; Marre, S. Nanostructured Materials for Photocatalysis. *Chem. Soc. Rev.* **2019**, *48*, 3868−3902.

(240) Wang, Q.; Domen, K. Particulate Photocatalysts for Light-Driven Water Splitting: Mechanisms, Challenges, and Design Strategies. *Chem. Rev.* **2020**, *120*, 919−985.

(241) Chen, S.; Takata, T.; Domen, K. Particulate Photocatalysts for Overall Water Splitting. *Nat. Rev. Mater.* **2017**, *2*, 1−17.

(242) Chen, X.; Shen, S.; Guo, L.; Mao, S. S. Semiconductor-based Photocatalytic Hydrogen Generation. *Chem. Rev.* **2010**, *110*, 6503−6570.

(243) Chen, P.; Liu, H.; Cui, W.; Lee, S. C.; Wang, L. a.; Dong, F. Bi-based Photocatalysts for Light-Driven Environmental and Energy Applications: Structural Tuning, Reaction Mechanisms, and Challenges. *EcoMat* **2020**, *2*, No. e12047.

(244) Chandrasekaran, S.; Yao, L.; Deng, L.; Bowen, C.; Zhang, Y.; Chen, S.; Lin, Z.; Peng, F.; Zhang, P. Recent Advances in Metal Sulfides: From Controlled Fabrication to Electrocatalytic, Photocatalytic and Photoelectrochemical Water Splitting and Beyond. *Chem. Soc. Rev.* **2019**, *48*, 4178−4280.

(245) Chen, G.; Wang, P.; Wu, Y.; Zhang, Q.; Wu, Q.; Wang, Z.; Zheng, Z.; Liu, Y.; Dai, Y.; Huang, B. Lead-Free Halide Perovskite $Cs_3Bi_{2x}Sb_{2−2x}I_9$ (x approximately 0.3) Possessing the Photocatalytic Activity for Hydrogen Evolution Comparable to that of $(CH_3NH_3)$-$PbI_3$. *Adv. Mater.* **2020**, *32*, No. e2001344.

(246) Kwolek, P.; Pilarczyk, K.; Tokarski, T.; Mech, J.; Irzmanski, J.; Szacilowski, K. Photoelectrochemistry of n-Type Antimony Sulfoiodide Nanowires. *Nanotechnol.* **2015**, *26*, 105710.

(247) Tamilselvan, M.; Bhattacharyya, A. J. Antimony Sulphoiodide (SbSI), a Narrow Band-Gap non-Oxide Ternary Semiconductor with Efficient Photocatalytic Activity. *RSC Adv.* **2016**, *6*, 105980−105987.

(248) Tasviri, M.; Sajadi-Hezave, Z. SbSI Nanowires and CNTs Encapsulated with SbSI as Photocatalysts with High Visible-Light Driven Photoactivity. *Mol. Catal.* **2017**, *436*, 174−181.

(249) Xiao, M.; Wang, Z.; Lyu, M.; Luo, B.; Wang, S.; Liu, G.; Cheng, H. M.; Wang, L. Hollow Nanostructures for Photocatalysis: Advantages and Challenges. *Adv. Mater.* **2019**, *31*, No. e1801369.

(250) Tong, H.; Ouyang, S.; Bi, Y.; Umezawa, N.; Oshikiri, M.; Ye, J. Nano-Photocatalytic Materials: Possibilities and Challenges. *Adv. Mater.* **2012**, *24*, 229−251.

(251) Hoang, S.; Gao, P. X. Nanowire Array Structures for Photocatalytic Energy Conversion and Utilization: A Review of Design Concepts, Assembly and Integration, and Function Enabling. *Adv. Energy Mater.* **2016**, *6*, 1600683.

(252) Wang, H.; Liu, X.; Niu, P.; Wang, S.; Shi, J.; Li, L. Porous Two-Dimensional Materials for Photocatalytic and Electrocatalytic Applications. *Matter* **2020**, *2*, 1377−1413.

(253) Wang, C.; Zhang, M.; Fang, Y.; Chen, G.; Li, Q.; Sheng, X.; Xu, X.; Hui, J.; Lan, Y.; Fang, M.; et al. SbSI Nanocrystals: An Excellent Visible Light Photocatalyst with Efficient Generation of Singlet Oxygen. *ACS Sustainable Chem. Eng.* **2018**, *6*, 12166−12175.

(254) Woods-Robinson, R.; Han, Y.; Zhang, H.; Ablekim, T.; Khan, I.; Persson, K. A.; Zakutayev, A. Wide Band Gap Chalcogenide Semiconductors. *Chem. Rev.* **2020**, *120*, 4007−4055.

(255) Chaves, A.; Azadani, J. G.; Alsalman, H.; da Costa, D. R.; Frisenda, R.; Chaves, A. J.; Song, S. H.; Kim, Y. D.; He, D.; Zhou, J.; et al. Bandgap Engineering of Two-Dimensional Semiconductor Materials. *npj 2D Mater. Appl.* **2020**, *4*, 1−21.

(256) Batzill, M. Fundamental Aspects of Surface Engineering of Transition Metal Oxide Photocatalysts. *Energy Environ. Sci.* **2011**, *4*, 3275−3286.

(257) Zheng, L.; Teng, F.; Ye, X.; Zheng, H.; Fang, X. Photo/Electrochemical Applications of Metal Sulfide/$TiO_2$ Heterostructures. *Adv. Energy Mater.* **2020**, *10*, 1902355.

(258) Tan, G.; Zhao, L. D.; Kanatzidis, M. G. Rationally Designing High-Performance Bulk Thermoelectric Materials. *Chem. Rev.* **2016**, *116*, 12123−12149.

(259) Chen, G.; Li, W.; Yu, Y.; Yang, Q. Fast And Low-Temperature Synthesis of One-Dimensional (1D) Single-Crystalline SbSI Microrod

for High Performance Photodetector. *RSC Adv.* **2015**, *5*, 21859−21864.

(260) Sun, L.; Wang, C.; Xu, L.; Wang, J.; Liu, X.; Chen, X.; Yi, G.-C. Sbsi Whisker/PbI$_2$ Flake Mixed-Dimensional Van Der Waals Heterostructure for Photodetection. *CrystEngComm* **2019**, *21*, 3779−3787.

(261) Shen, J.; Liu, X.; Wang, C.; Wang, J.; Wu, B.; Chen, X.; Yi, G.-c. SbSI Microrod Based Flexible Photodetectors. *J. Phys. D: Appl. Phys.* **2020**, *53*, 345106.

(262) Purusothaman, Y.; Alluri, N. R.; Chandrasekhar, A.; Kim, S.-J. Photoactive Piezoelectric Energy Harvester Driven By Antimony Sulfoiodide (SbSI): A$^{AV}$B$^{VI}$C$^{VII}$ Class Ferroelectric-Semiconductor Compound. *Nano Energy* **2018**, *50*, 256−265.

(263) Mistewicz, K.; Jesionek, M.; Nowak, M.; Kozioł, M. SbSeI Pyroelectric Nanogenerator for A Low Temperature Waste Heat Recovery. *Nano Energy* **2019**, *64*, 103906.

(264) Wang, X.; Song, W.; Liu, B.; Chen, G.; Chen, D.; Zhou, C.; Shen, G. High-Performance Organic-Inorganic Hybrid Photodetectors Based on P3HT:CdSe Nanowire Heterojunctions on Rigid and Flexible Substrates. *Adv. Funct. Mater.* **2013**, *23*, 1202−1209.

(265) Wang, H. P.; Li, S.; Liu, X.; Shi, Z.; Fang, X.; He, J. H. Low-Dimensional Metal Halide Perovskite Photodetectors. *Adv. Mater.* **2021**, *33*, No. e2003309.

(266) Chen, H.; Liu, K.; Hu, L.; Al-Ghamdi, A. A.; Fang, X. New Concept Ultraviolet Photodetectors. *Mater. Today* **2015**, *18*, 493−502.

(267) Saran, R.; Curry, R. J. Lead Sulphide Nanocrystal Photodetector Technologies. *Nat. Photonics* **2016**, *10*, 81−92.

(268) Konstantatos, G.; Sargent, E. H. Nanostructured Materials for Photon Detection. *Nat. Nanotechnol.* **2010**, *5*, 391−400.

(269) Talapin, D. V.; Lee, J.-S.; Kovalenko, M. V.; Shevchenko, E. V. Prospects of Colloidal Nanocrystals for Electronic and Optoelectronic Applications. *Chem. Rev* **2010**, *110*, 389−458.

(270) García de Arquer, F. P.; Armin, A.; Meredith, P.; Sargent, E. H. Solution-Processed Semiconductors For Next-Generation Photodetectors. *Nat. Rev. Mater.* **2017**, *2*, 16100.

(271) Baugher, B. W.; Churchill, H. O.; Yang, Y.; Jarillo-Herrero, P. Optoelectronic Devices Based On Electrically Tunable P-N Diodes in A Monolayer Dichalcogenide. *Nat. Nanotechnol.* **2014**, *9*, 262−267.

(272) Tian, W.; Zhou, H.; Li, L. Hybrid Organic-Inorganic Perovskite Photodetectors. *Small* **2017**, *13*, 1702107.

(273) Eng, P. C.; Song, S.; Ping, B. State-of-The-Art Photodetectors for Optoelectronic Integration at Telecommunication Wavelength. *Nanophotonics* **2015**, *4*, 277−302.

(274) Winter, M.; Brodd, R. J. What Are Batteries, Fuel Cells, and Supercapacitors? *Chem. Rev* **2004**, *104*, 4245−4269.

(275) Blanc, L. E.; Kundu, D.; Nazar, L. F. Scientific Challenges for the Implementation of Zn-Ion Batteries. *Joule* **2020**, *4*, 771−799.

(276) Ryu, H.; Yoon, H. J.; Kim, S. W. Hybrid Energy Harvesters: Toward Sustainable Energy Harvesting. *Adv. Mater.* **2019**, *31*, No. e1802898.

(277) Shao, Y.; El-Kady, M. F.; Sun, J.; Li, Y.; Zhang, Q.; Zhu, M.; Wang, H.; Dunn, B.; Kaner, R. B. Design and Mechanisms of Asymmetric Supercapacitors. *Chem. Rev.* **2018**, *118*, 9233−9280.

(278) Wang, F.; Wu, X.; Yuan, X.; Liu, Z.; Zhang, Y.; Fu, L.; Zhu, Y.; Zhou, Q.; Wu, Y.; Huang, W. Latest Advances In Supercapacitors: From New Electrode Materials to Novel Device Designs. *Chem. Soc. Rev.* **2017**, *46*, 6816−6854.

(279) Wang, G.; Zhang, L.; Zhang, J. A Review Of Electrode Materials For Electrochemical Supercapacitors. *Chem. Soc. Rev.* **2012**, *41*, 797−828.

(280) Wang, Y.; Xia, Y. Recent Progress In Supercapacitors: From Materials Design To System Construction. *Adv. Mater.* **2013**, *25*, 5336−5342.

(281) Winter, M.; Barnett, B.; Xu, K. Before Li Ion Batteries. *Chem. Rev.* **2018**, *118*, 11433−11456.

(282) Yabuuchi, N.; Kubota, K.; Dahbi, M.; Komaba, S. Research Development On Sodium-Ion Batteries. *Chem. Rev.* **2014**, *114*, 11636−11682.

(283) Zhong, C.; Deng, Y.; Hu, W.; Qiao, J.; Zhang, L.; Zhang, J. A Review of Electrolyte Materials And Compositions For Electrochemical Supercapacitors. *Chem. Soc. Rev.* **2015**, *44*, 7484−7539.

(284) Kumar, P.; Wahyudi, W.; Sharma, A.; Yuan, Y.; Harrison, G. T.; Gedda, M.; Wei, X.; El-Labban, A.; Ahmad, S.; Kumar, V.; et al. Bismuth-Based Mixed-Anion Compounds For Anode Materials In Rechargeable Batteries. *Chem. Commun.* **2022**, *58*, 3354−3357.

(285) Wang, A.; Hong, W.; Yang, L.; Tian, Y.; Qiu, X.; Zou, G.; Hou, H.; Ji, X. Bi-Based Electrode Materials for Alkali Metal-Ion Batteries. *Small* **2020**, *16*, 2004022.

(286) Goodenough, J. B.; Park, K. S. The Li-Ion Rechargeable Battery: A Perspective. *J. Am. Chem. Soc.* **2013**, *135*, 1167−1176.

(287) Janek, J.; Zeier, W. G. A Solid Future For Battery Development. *Nat. Energy* **2016**, *1*, 16141.

(288) Zhou, L.; Assoud, A.; Zhang, Q.; Wu, X.; Nazar, L. F. New Family of Argyrodite Thioantimonate Lithium Superionic Conductors. *J. Am. Chem. Soc.* **2019**, *141*, 19002−19013.

(289) Lee, Y.; Jeong, J.; Lim, H.-D.; Kim, S.-O.; Jung, H.-G.; Chung, K. Y.; Yu, S. Superionic Si-Substituted Lithium Argyrodite Sulfide Electrolyte Li$_{6+x}$Sb$_{1-x}$Si$_x$S$_5$I for All-Solid-State Batteries. *ACS Sustainable Chem. Eng* **2021**, *9*, 120−128.

(290) Lee, Y.; Jeong, J.; Lee, H. J.; Kim, M.; Han, D.; Kim, H.; Yuk, J. M.; Nam, K.-W.; Chung, K. Y.; Jung, H.-G.; et al. Lithium Argyrodite Sulfide Electrolytes with High Ionic Conductivity and Air Stability for All-Solid-State Li-Ion Batteries. *ACS Energy Lett.* **2022**, *7*, 171−179.

(291) Shi, X. L.; Zou, J.; Chen, Z. G. Advanced Thermoelectric Design: From Materials and Structures to Devices. *Chem. Rev.* **2020**, *120*, 7399−7515.

(292) Bell, L. E. Cooling, Heating, Generating Power, and Recovering Waste Heat with Thermoelectric Systems. *Science* **2008**, *321*, 1457−1461.

(293) Zeng, M.; Zavanelli, D.; Chen, J.; Saeidi-Javash, M.; Du, Y.; LeBlanc, S.; Snyder, G. J.; Zhang, Y. Printing Thermoelectric Inks Toward Next-Generation Energy And Thermal Devices. *Chem. Soc. Rev.* **2022**, *51*, 485−512.

(294) Massetti, M.; Jiao, F.; Ferguson, A. J.; Zhao, D.; Wijeratne, K.; Wurger, A.; Blackburn, J. L.; Crispin, X.; Fabiano, S. Unconventional Thermoelectric Materials for Energy Harvesting and Sensing Applications. *Chem. Rev.* **2021**, *121*, 12465−12547.

(295) He, J.; Tritt, T. M. Advances in Thermoelectric Materials Research: Looking Back And Moving Forward. *Science* **2017**, *357*, No. eaak9997.

(296) Zhu, T.; Liu, Y.; Fu, C.; Heremans, J. P.; Snyder, J. G.; Zhao, X. Compromise and Synergy in High-Efficiency Thermoelectric Materials. *Adv. Mater.* **2017**, *29*, 1605884.

(297) Gaultois, M. W.; Sparks, T. D.; Borg, C. K. H.; Seshadri, R.; Bonificio, W. D.; Clarke, D. R. Data-Driven Review of Thermoelectric Materials: Performance and Resource Considerations. *Chem. Mater.* **2013**, *25*, 2911−2920.

(298) Zeier, W. G.; Zevalkink, A.; Gibbs, Z. M.; Hautier, G.; Kanatzidis, M. G.; Snyder, G. J. Thinking Like a Chemist: Intuition in Thermoelectric Materials. *Angew. Chem., Int. Ed.* **2016**, *55*, 6826−6841.

(299) Fan, F. R.; Tang, W.; Wang, Z. L. Flexible Nanogenerators for Energy Harvesting and Self-Powered Electronics. *Adv. Mater.* **2016**, *28*, 4283−4305.

(300) Hu, F.; Cai, Q.; Liao, F.; Shao, M.; Lee, S. T. Recent Advancements in Nanogenerators for Energy Harvesting. *Small* **2015**, *11*, 5611−5628.

(301) Mahapatra, S. D.; Mohapatra, P. C.; Aria, A. I.; Christie, G.; Mishra, Y. K.; Hofmann, S.; Thakur, V. K. Piezoelectric Materials for Energy Harvesting and Sensing Applications: Roadmap for Future Smart Materials. *Adv. Sci.* **2021**, *8*, No. e2100864.

(302) Korkmaz, S.; Kariper, I. A. Pyroelectric Nanogenerators (Pyngs) In Converting Thermal Energy Into Electrical Energy: Fundamentals and Current Status. *Nano Energy* **2021**, *84*, 105888.

(303) Hu, Y.; Wang, Z. L. Recent Progress In Piezoelectric Nanogenerators As A Sustainable Power Source In Self-Powered Systems and Active Sensors. *Nano Energy* **2015**, *14*, 3−14.

(304) Rabenau, V. A.; Rau, H. Uber Sulfidhalogenide Des Bleis Und Das $Pb_4SeBr_6$. *Zeitschrift fur anorganische und allgemeine Chemie. Band* **1969**, *369*, 295−305.

(305) Nie, R.; Kim, B.; Hong, S. T.; Seok, S. I. Nanostructured Heterojunction Solar Cells Based on $Pb_2SbS_2I_3$: Linking Lead Halide Perovskites and Metal Chalcogenides. *ACS Energy Lett.* **2018**, *3*, 2376−2382.

(306) Nie, R.; Lee, K. S.; Hu, M.; Paik, M. J.; Seok, S. I. Heteroleptic Tin-Antimony Sulfoiodide for Stable and Lead-free Solar Cells. *Matter* **2020**, *3*, 1701−1713.

(307) Dolgikh, V. A. New Chalkogen-Halogenides of The Type MSbSI. *Izv. Akad. Nauk SSSR, Neorg. Mater* **1985**, *21*, 1211.

(308) Starosta, V. I.; Kroutil, J.; Benes, L. Preparation and Fundamental Physical Properties of $Sn_2SbS_2I_3$, and $Pb_2SbS_2I_3$ Compounds. *Cryst. Res. Technol.* **1990**, *25*, 1439−1442.

(309) Oliver-Fourcade, J.; Jumas, J. C.; Maurin, M.; Philippot, E. A New Sulfoiodide Of Tin And Antimony: Structure Investigation. *Z. Anorg. Allg. Chem.* **1980**, *468*, 91.

(310) Dolgikhv, A. New chalcogen-halogenides of the type $M_2SbS_2I_3$. *Izv Akad Nauk SSSR. Neorg. Mater.* **1985**, *25*, 1439.

(311) Reuter, B.; Hardel, K. Silver Sulfide Bromide and Silver Sulfide Iodide. *Angew. Chem., Int. Ed.* **1960**, *72*, 138.

(312) Takahashi, T.; Yamamoto, O. The $Ag/Ag_3SI/I_2$, Solid-Electrolyte Cell. *Electrochim. Acta* **1966**, *11*, 779−789.

(313) Tver'yanovich, Y. S.; Bal'makov, M. D.; Tomaev, V. V.; Borisov, E. N.; Volobueva, O. Ion-conducting multilayer films based on alternating nanolayers $Ag_3SI$, AgI and $Ag_2S$, AgI. *Glass Phys. Chem.* **2008**, *34*, 150−154.

(314) Beeken, R. B.; Beeken, E. M. Ionic conductivity in Cu-substituted $Ag_3SBr$. *Solid State Ionics* **2000**, *136−137*, 463−467.

(315) Kurita, M.; Nakagawa, K.; Akao, F. Photoacoustic Spectrum in Superionic Conductors $Ag_3SI$ and AgI. *J. App. Phys* **1988**, *27*, L1920−L1922.

(316) Shimosaka, W.; Kashida, S.; Kobayashi, M. Electronic Structure of AgSI. *Solid State Ionics* **2005**, *176*, 349−355.

(317) Li, J.; Liu, X.; Xu, J.; Chen, J.; Zhao, C.; Salma Maneno, M.; Zhang, B.; Yao, J. Fabrication of Sulfur-Incorporated Bismuth-Based Perovskite Solar Cells via a Vapor-Assisted Solution Process. *Solar RRL* **2019**, *3*, 1900218.

(318) Zhang, C.; Teo, S.; Guo, Z.; Gao, L.; Kamata, Y.; Xu, Z.; Ma, T. Development of a Mixed Halide-chalcogenide Bismuth-based Perovskite $MABiI_2S$ with Small Bandgap and Wide Absorption Range. *Chem. Lett.* **2019**, *48*, 249−252.

(319) Kageyama, H.; Hayashi, K.; Maeda, K.; Attfield, J. P.; Hiroi, Z.; Rondinelli, J. M.; Poeppelmeier, K. R. Expanding Frontiers In Materials Chemistry And Physics With Multiple Anions. *Nat. Commun.* **2018**, *9*, 772.

(320) Meredig, B.; Wolverton, C. A Hybrid Computational-Experimental Approach For Automated Crystal Structure Solution. *Nat. Mater.* **2013**, *12*, 123−127.

(321) Seko, A.; Koyama, Y.; Tanaka, I. Cluster Expansion Method For Multicomponent Systems Based On Optimal Selection Of Structures for Density-Functional Theory Calculations. *Phys. Rev. B* **2009**, *80*, 165122−7.

(322) Zunger, A.; Wei, S.; Ferreira, L. G.; Bernard, J. E. Special Quasirandom Structures. *Phys. Rev. Lett.* **1990**, *65*, 353−356.

(323) Zhang, X.; Shen, J.-X.; Wang, W.; Van de Walle, C. G. First-Principles Analysis of Radiative Recombination in Lead-Halide Perovskites. *ACS Energy Lett.* **2018**, *3*, 2329−2334.

(324) Califano, M.; Lu, R.; Zhou, Y. Indirect to Direct Band Gap Transformation by Surface Engineering in Semiconductor Nanostructures. *ACS Nano* **2021**, *15*, 20181−20191.

(325) Malyi, O. I.; Acosta, C. M. Amorphization of Indirect Band Gap Semiconductors To Tune Their Optoelectronic Properties. *J. Phys. Chem. C* **2020**, *124*, 14432−14438.

(326) Lee, I.-H.; Lee, J.; Oh, Y. J.; Kim, S.; Chang, K. J. Computational Search For Direct Band Gap Silicon Crystals. *Phys. Rev. B* **2014**, *90*, 115209.

(327) Wang, Q.; Xu, B.; Sun, J.; Liu, H.; Zhao, Z.; Yu, D.; Fan, C.; He, J. Direct Band Gap Silicon Allotropes. *J. Am. Chem. Soc.* **2014**, *136*, 9826−9829.

(328) Jing, Y.; Ma, Y.; Li, Y.; Heine, T. $GeP_3$: A Small Indirect Band Gap 2D Crystal with High Carrier Mobility and Strong Interlayer Quantum Confinement. *Nano Lett* **2017**, *17*, 1833−1838.

(329) d'Avezac, M.; Luo, J. W.; Chanier, T.; Zunger, A. Genetic-Algorithm Discovery of A Direct-Gap and Optically Allowed Superstructure From Indirect-Gap Si and Ge Semiconductors. *Phys. Rev. Lett.* **2012**, *108*, 027401.

(330) Hadi, M. A.; Islam, M. N.; Podder, J. Indirect To Direct Band Gap Transition Through Order To Disorder Transformation Of $Cs_2AgBiBr_6$ Via Creating Antisite Defects For Optoelectronic and Photovoltaic Applications. *RSC Adv.* **2022**, *12*, 15461−15469.

(331) Mutailipu, M.; Poeppelmeier, K. R.; Pan, S. Borates: A Rich Source for Optical Materials. *Chem. Rev.* **2021**, *121*, 1130−1202.

(332) Mutailipu, M.; Li, F. M.; Jin, C. C.; Yang, Z. H.; Poeppelmeier, K. R.; Pan, S. L. Strong Nonlinearity Induced by Coaxial Alignment of Polar Chain and Dense $[BO_3]$ Units in $CaZn_2(BO_3)_2$. *Angew. Chem.* **2022**, *61*, No. e202202096.